Etude numérique et analyse physique du morphing de profils d'aile de type Airbus A3XX en régime transsonique par l'approche de modélisation de la turbulence "Organised Eddy Simulation" à nombre de Reynolds élevé.

Jean-Baptiste Tô

THÈSE

En vue de l'obtention du

DOCTORAT DE L'UNIVERSITÉ DE TOULOUSE

Délivré par :

Institut National Polytechnique de Toulouse (Toulouse INP)

Discipline ou spécialité :

Dynamique des fluides

Présentée et soutenue par :

M. JEAN-BAPTISTE TO

le mercredi 27 octobre 2021

Titre :

Etude numérique et analyse physique du morphing de profils d'aile de type Airbus A3XX en régime transsonique par l'approche de modélisation de la turbulence "Organised Eddy Simulation" à nombre de Reynolds

---

Ecole doctorale :

Mécanique, Energétique, Génie civil, Procédés (MEGeP)

Unité de recherche :

Institut de Mécanique des Fluides de Toulouse (IMFT)

Directeurs de Thèse :

MME MARIANNA BRAZA

M. GILLES HARRAN

Rapporteurs :

M. BRUNO KOOBUS, UNIVERSITE DE MONTPELLIER

M. PAWEL FLASZINSKI, POLISH ACADEMY OF SCIENCES GDANSK

Membres du jury :

M. YANNICK HOARAU, UNIVERSITE DE STRASBOURG, Président

M. FLAVIEN BILLARD, DASSAULT AVIATION, Membre

M. GEORGE TZABIRAS, NATIONAL TECHNICAL UNIVERSITY ATHENES, Membre

M. GILLES HARRAN, TOULOUSE INP, Invité

MI. JEAN-FRANÇOIS ROUCHON, TOULOUSE INP, Membre

MME MARIANNA BRAZA, TOULOUSE INP, Membre

Organisation du manuscrit

Le morphing électroactif en tant que concept est tout d'abord défini et son implémentation sera détaillée dans la première partie de ce manuscrit. Un aperçu de l'état de l'art sera ensuite donné afin de décrire les récentes avancées de la recherche sur le morphing dans les phases de vol subsonique, tant sur un plan expérimental que numérique. Il s'agira également de mentionner les diverses contributions sur le thème du contrôle d'écoulements en régime transsonique et des interactions entre choc et couche limite.

Une partie est dédiée à la description des schémas numériques, de la configuration du domaine de simulation. Le choix du modèle de turbulence sera également motivé.

Un bref chapitre sur la phénoménologie des Interactions entre Choc et Couche Limite dans le régime considéré fait écho à la première partie en montrant l'émergence de l'instabilité du tremblement transsonique au travers des simulations numériques bi-dimensionnelles ainsi que tri-dimensionnelles, en motivant l'usage du morphing en tant que technologie permettant la manipulation des instationnarités de l'écoulement lors d'un vol de croisière.

Les résultats de la thèse sont ensuite présentés, mettant en exergue l'effet du morphing de bord de fuite à haute fréquence sur la modification des performances aérodynamique en vol ainsi que les interactions entre le mode du tremblement et les fréquences de vibration du bord de fuite.

Acknowledgements

This thesis lasted 4 long years, and yet they felt so short. Throughout the duration of my doctoral studies, I have encountered many hardships but just as many hands - if not more! - reaching out to help me and provide me with endless support, whether technical or emotional in nature.

First, I would like to extend my many thanks to Dr. Marianna Braza, my supervisor, with whom I have spent many evenings discussing and working on the subtleties of my research topic. Your expertise, patience and words of wisdom have guided me in moments of doubt and your rigorousness constantly reminded me that I had to strive for thoroughness and diligence in my research tasks. I also would like to thank Gilles Harran who was my former teacher in ENSEEIHT and who was always supportive of my work as my co-supervisor.

Among the many people who greatly contributed to the success of this thesis, I would like to kindly express my gratitude to Profs. Jean-François Rouchon, Yannick Hoarau for their help, Pr. Tzabiras and Dr. Billard for being part of the committee and showing interest in my work as well as Profs. Koobus and Flaszynski who very kindly accepted to review my manuscript and help me improve it.

I am indebted to the *University of Toulouse*, *Toulouse INP*, the *Institut de Mécanique des Fluides de Toulouse* and the *Smart Morphing and Sensing* project for granting me the opportunity to fulfill this doctoral work and providing me with the financial means to do so.

To my colleagues and former teachers, I would also like to send words of acknowledgement and appreciation for the formal and informal conversations we had together as well as the knowledge you passed on to me. Many thanks to the technical IT support of IMFT for their friendliness and unwavering assistance even when the World seemed to collapse around me. Yes, this is sometimes the feeling of helplessness I had in front of a BSOD...

Last, but not least, I would like to warmly thank my family and my friends in IMFT and outside the laboratory who helped me cope with the stern day-to-day life of a young researcher during the onset of a global pandemic. The

pleasant moments around a meal, a beer, a coffee or a competitive game of table tennis will be forever kept in my heart. I deeply thank my parents who have both always tried their best to provide me with a lot of comfort and encouragement. You have always been my home and my primary source of solace.

Contents

List of Figures

List of Tables

To my friends, to my parents.

Chapter 1

Introduction

Dans un monde en constante expansion tant sur le plan économique que démographique, l'industrie aéronautique fait face à un besoin pressant de répondre à des problématiques financières et environnementales. En 2016, 3,6 milliards d'êtres humains avaient utilisé l'avion pour se déplacer. L'International Air Transport Association (IATA) considère que ce nombre pourrait doubler en 2035 en raison d'une estimation du taux de croissance moyen de l'ordre de 3.7% sur une durée de 20 ans. Ce constat amène de nombreux acteurs du monde aéronautique à constamment innover dans le but de réduire l'impact environnemental du vol commercial et dans l'optique de concilier croissance et développement durable.

L'évolution de l'avion de ligne au cours du dernier siècle a progressivement amené l'implémentation de composants électroniques en plus d'actionneurs hydrauliques afin de faciliter et automatiser les commandes de vol, faisant de l'avion le moyen de transport le plus sûr, le plus rapide et le moins coûteux sur de longues distances. Mais le besoin d'associer de nombreux systèmes hétérogènes a fait de l'avion un appareil complexe et lourd. Les principaux défis auxquels doivent faire face les avionneurs sont ainsi de dimensionner un engin robuste mais léger, aux commandes redondantes mais ergonomiques, rapide mais sûr.

Ces besoins parfois complémentaires, parfois antagonistes, entraînent souvent la recherche d'un compromis. Mais cette recherche amène également au développement incrémental de nouvelles méthodes, technologies et procédés qui permettent à l'avion de devenir plus efficace, plus propre et plus sûr au

cours du temps.

Dans un contexte économique changeant et face aux défis environnementaux auxquels les constructeurs d'avions sont confrontés, il devient primordial de faire appel à des concepts innovants et des idées empruntées à la Nature. C'est dans ce cadre que le projet Smart Morphing and Sensing for aeronautical configurations (SMS - http://smartwing.org/SMS/EU) intervient. Ce projet de recherche, piloté par l'Institut National Polytechnique de Toulouse, s'inscrit dans le cadre du programme H2020 de la Commission Européenne, et réunit 10 partenaires venant de 5 pays européens dans le but de développer un nouveau concept d'aile déformable — le Morphing Hybride Electroactif — qui s'inspire des ailes d'oiseau. Cette déformation continue et modulable en fonction des conditions de vol permet d'améliorer le comportement des aéronefs, les performances aérodynamiques ainsi que de réduire les sources de bruit liées à l'écoulement autour des surfaces portantes. Il serait ainsi possible de réduire la consommation de carburant et les émanations de gaz à effet de serre. En effet, les rejets de gaz carbonique et d'oxydes d'azote sont principalement dûs à la température de flamme au sein de la chambre à combustion des moteurs d'avion. En réduisant la poussée à fournir lors d'un trajet, notamment lors du décollage qui est la phase nécessitant une poussée maximale et la phase de croisière qui est la phase la plus longue, le but du morphing est de permettre à l'avion de devenir plus économe, se basant sur des prédictions allant jusqu'à au moins 1% de gain sur la consommation de carburant.

Cette thèse s'intéresse au morphing électroactif en tant que technique permettant la déformation des surfaces portantes et l'amélioration des performances aérodynamiques dans toutes les phases du vol, ici en particulier dans la phase de croisière, une étape du vol lors de laquelle l'écoulement autour de l'avion est transsonique et donne lieu à des phénomènes de compressibilité. L'étude portera notamment sur la compréhension et la manipulation d'une instabilité provenant de l'Interaction entre Choc et Couche Limite (en anglais "Shock Wave Boundary Layer Interactions", ou SWBLI) en écoulement transsonique par le biais du morphing. L'utilisation d'outils de modélisation de la turbulence et de résolution numérique des équations de Navier-Stokes permettent d'établir le comportement de cette instabilité sous l'action d'une déformation dynamique de l'aile.

Les simulations ont été produites avec le code Navier Stokes MultiBlock (NSMB), par le biais d'une approche statistique de modélisation de la turbulence qui rend compte de la formation de structures cohérentes et de leur interaction avec le fond désordonné et chaotique de la turbulence.

Les résultats de simulation permettent de mettre en exergue l'influence de certains artefacts vorticaux dans la dynamique des interactions entre choc et couche limite, et exhibent des phénomènes dont la compréhension rend possible la manipulation des instabilités résultantes à l'aide du morphing électroactif. Ainsi, plusieurs modes de déformation et fréquences de vibration sur des plages allant de 100 Hz à plus de 800 Hz ont été étudiés et couplés à des études expérimentales en soufflerie dans le cadre du projet SMS. Cette étude paramétrique et l'exploitation physique qui en résulte montre que l'emploi de certaines fréquences permet de considérablement réduire la traînée de forme des surfaces portantes à l'aide d'une rétro-action sur la SWBLI. La finesse aérodynamique se retrouve également augmentée pour ces mêmes fréquences de déformation. Cela laisse présager la possibilité d'exploiter le morphing de haute fréquence en phase de croisière afin d'améliorer les performances aérodynamiques d'un avion commercial.

In a world in constant expansion and growth, both economically and demographically, the aeronautics industry faces a pressing need to respond to financial and environmental issues. In 2016, 3.6 billion people used the plane to get around. The International Air Transport Association (IATA) considers that this number could double in 2035 due to an estimated average growth rate of around 3.7% over a period of 20 years. This observation has led many players in the aeronautical world to constantly innovate in order to reduce the environmental impact of commercial flight with a view to reconciling growth and sustainable development.

The evolution of the commercial airliner over the last century has gradually brought about the implementation of electronic components in addition to hydraulic actuators in order to facilitate and automate flight controls, making the aircraft the safest means of transport, the fastest and cheapest over long distances. But the need to combine many heterogeneous systems

has made the airplane a complex and cumbersome machine. Therefore, aircraft manufacturers face many challenges. They notably have to answer the demand for a robust but light vehicle, with redundant but ergonomic controls and the ability to travel quickly but safely.

These conflicting needs often lead designers to seek compromises. But this search for the middle ground also leads to the incremental development of new methods, technologies and processes that allow the aircraft to become more efficient and safer over time.

In an ever-changing economy and facing environmental pressure, aircraft manufacturers need to adapt to new requirements for a cleaner aircraft. It thus becomes essential to explore innovative concepts and ideas borrowed from Nature. It is in this context that the Smart Morphing and Sensing for aeronautical configurations project (SMS — http://smartwing.org/SMS/EU) intervenes. This research project, led by the National Polytechnic Institute of Toulouse, is part of the European Commission's Horizon 2020 program, and brings together 10 partners from 5 European countries with the goal of developing a new compliant wing concept called bio-inspired and electro-active hybrid morphing.

This technology was inspired by bird wings to achieve the same optimal flight. To do so, a continuous deformation is imparted to the wing, said deformation being modified over time depending on the flight conditions in order to improve aircraft stability, aerodynamic performance and reduce airflow-generated noise sources at all times. It would thus be possible to reduce fuel consumption and greenhouse gas emissions. Indeed, the release of carbon dioxide and nitrogen oxides are mainly due to the flame temperature within the combustion chamber of aircraft turbo engines. By reducing the required thrust throughout a plane trip, especially during take-off and cruise, morphing aims to make commercial aircraft a more economical transportation method, based on predictions that such a technology would allow to save up to at least 1% in terms of fuel consumption.

This thesis studies electroactive morphing as a technique allowing the deformation of airfoils and the improvement of aerodynamic performance in all flight phases and — of most interest here — in during cruise, a phase when the flow around the aircraft is transonic which gives rise to compressibility

phenomena. This analysis will focus on the understanding and manipulation through morphing of an instability resulting from so-called Shock Wave-Boundary Layer Interactions (or SWBLI) in the transonic regime. The use of turbulence modeling tools and the numerical resolution of the Navier-Stokes equations help establish the behavior of this instability under the action of a dynamic deformation of the wing.

The simulations were produced using the Navier-Stokes MultiBlock (NSMB) code, as well as a statistical turbulence modeling approach that accounts for the formation and development of coherent structures and their interaction with the messy and random background of turbulence. The simulation results allow to highlight the importance of certain coherent vortical structures in the dynamics of SWBLIs. They also exhibit feedback mechanisms that enable the manipulation of the resulting flow instability using electroactive morphing. Consequently, several deformation modes and vibration frequencies from 100 Hz to more than 800 Hz have been investigated and coupled with wind tunnel studies as part of the SMS project. This parametric study and the resulting discussion show that the use of specific frequencies can reduce shape drag by means of the aforementioned feedback effect that acts on decreasing the strength of the SWBLI. The lift to drag ratio is also found to be considerably increased for these same deformation frequencies. This suggests the possibility of using high-frequency morphing during cruise to improve the aerodynamic performance of a commercial aircraft.

Chapter 2

State of the art

2.1 Phenomenology

2.1.1 The transonic regime

The transonic regime is characterized by compressibility effects as opposed to the low subsonic regime where the flow is generally incompressible ($Ma < 0.3$) and the high subsonic regime ($0.3 < Ma < Ma_c$) where compressibility effects are weaker. The boundaries between the subsonic, transonic and supersonic regime are not clear-cut, and their definition may vary depending on the author, but it has been widely accepted that transonic flows happen whenever the critical Mach number is exceeded, that is the lowest Mach number that causes curvature-induced acceleration the flow to become supersonic. Under certain conditions dictated primarily by the Mach number, the angle of attack and the shape of the airfoil, a normal shock wave may form along the suction side or the pressure side of the wing

2.1.2 Transonic flows

Fluid flows are generally deemed transonic in a Mach number interval that encompasses both Mach numbers lower than unity and Mach numbers higher than unity. Transonic flows are typical of situations where the flow is not quite supersonic everywhere around the object it is flowing past, yet contains regions where it becomes locally supersonic. This usually occurs after a certain Mach number is reached for a given object with a given orientation in relation to the velocity vector of the flow, which is named the critical

Mach number Ma_c. For an increasing Mach number, the then subsonic flow thus becomes transonic, i.e. $Ma_\infty \geq Ma_c$, from the moment a supersonic pocket first appears in the vicinity of the object, the reason being that the object causes the flow to accelerate in its proximity until it reaches supersonic speeds.

2.2 Shock Wave-Boundary Layer Interactions

This section serves as an introduction to the topic of Shock Wave-Boundary Layer Interactions. First, this particular type of flow is defined qualitatively using the empirical observations and numerical calculations performed over the past 70 years of research. Then different kinds of SWBLI are classified into separate categories. Finally, an assessment of the interaction characteristics is carried out to identify the type of SWBLI that corresponds to the case studied in this thesis, for this particular geometry and flow regime.

2.2.1 What are Shock Wave-Boundary Layer Interactions?

In the transonic regime, there exists an freestream Mach number that will cause the flow to reach supersonic speeds over the surface of the body. For high enough Mach numbers, the solutions of Navier-Stokes equations result in the appearance of discontinuities. These can be either contact discontinuities or shocks. Contact discontinuities are surfaces that separate two zones with discontinuous thermodynamic properties - namely density and temperature - but leave pressure and tangential velocity continuous across the interface. On the other hand, shocks are a type of flow discontinuities associated with a sharp increase of pressure across the interface. These discontinuities happen due to the competition between non-linear effects, arising from the advection term in the Navier-Stokes equations, and dissipative effects that are caused by molecular viscosity as well as a result of turbulence. They physically manifest as the accumulation of a large number of acoustic waves or weak shocks (see figure). These waves represent the weak solution of the Rankine-Hugoniot equations that govern the behavior of the flow across such discontinuities.

Shock Wave-Boundary Layer Interactions take place whenever a shock

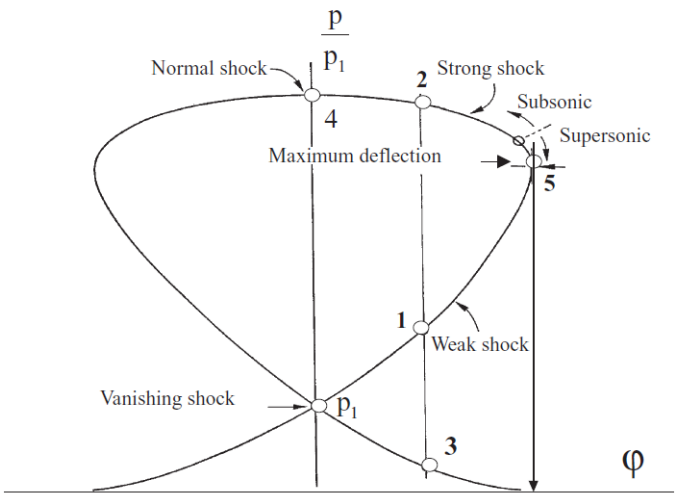

Figure 2.1: A shock-polar curve which represents the intensity of the pressure differential across the Rankine-Hugoniot solution as a function of the flow deflection caused by the corresponding discontinuity

encounters a boundary layer. Such cases have traditionally been studied in flat plate configurations where an oblique shock wave is generated by a wedge located upstream and impinges the opposite wall at an angle that is dictated by the Mach number. The boundary layer bound to the opposite wall is thus disturbed by the intense adverse pressure gradient caused by the incident shock, giving rise to a weak interaction due to the generally weak shock intensity in transonic flows and the absence of separation in the case of a flat plate. Others have also studied different configurations such as ramp-induced shocks (see Shang, W. L., and Law, 1976 for instance), normal shock waves (cf. Gadd, 1958) and adaptation shocks at the exit of an overexpanded nozzle (Frey, 1998).

The shock induces a sudden compression of the flow along with several transformations which are:

- Brutal flow deceleration across the shock.
- An abrupt density increase.
- Pressure increase.
- A sudden static temperature increase.

In any case, strong SWBLI are characterized by the presence of a strong shock - which is typically the case in the event of a normal shock - that interacts with a separating boundary layer. This usually happens on lifting bodies for sufficiently high angles of attack and Mach numbers (see Paladini et al., 2019 or Giannelis, Levinski, and Vio, 2018 for instance), on which surface curvature creates substantial flow accelerations and adverse pressure gradients leading to separation.

2.2.2 Typology of Shock Wave-Boundary Layer Interactions

2.2.2.1 Weak shock wave-boundary layer interactions

When an oblique shock impinges on a flat plate, it reflects away at the same angle. Within the boundary layer, a structure can be observed wherein the incident shock fans out across the thickness of the boundary layer (see figure).

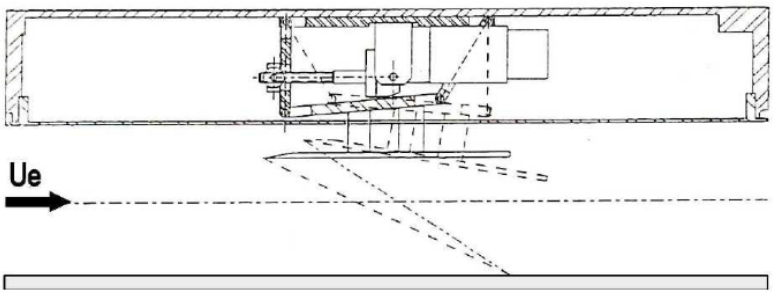

Figure 2.2: A schematic view showing the operation of a shock generator. A flat plate terminated by a bevelled edge on one side causes an oblique shock to form. Modifying the incidence of this shock generator will result in different shock incidences. Piponniau, 2009

Since the boundary layer is a region where flow velocity is allowed to decrease until it reaches zero, there exists a point where the shock meets a subsonic region. This coincidentally corresponds to a locus where the shock dissipates due to a low enough Mach number.

For inviscid flows, the presence of the shock normally creates a sudden compression immediately after the shock front, which takes place over very short but finite distances of typically 5 to 20 mean free paths according to

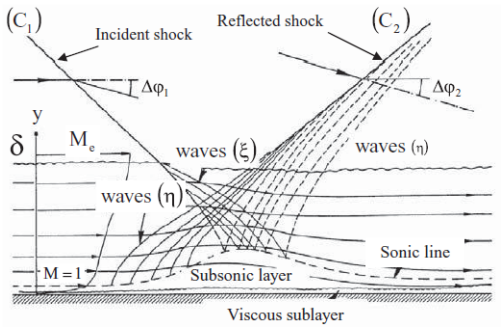

Figure 2.3: A schematic cross-sectional view of the turbulent shock-reflection on a flat plate without boundary-layer separation

Babinsky and Harvey, 2011, Sundén and Fu, 2017 and Kundu, Cohen, and Dowling, 2012. However, in the case of a real, viscous flow, the shock compresses the subsonic part of the BL which results in the compression zone being spread out due to the parabolic nature of the Navier-Stokes equations within the subsonic layer, instead of being solely localized at the shock impingement point. This streamwise dilation of the subsonic layer induces a slight upward deflection of streamlines within the boundary layer. This deflection results in the formation of an array of compression waves, or Mach waves, that coalesce to form the reflected shock.

Since the presence of the subsonic layer causes a slight modification of the flow topology leading to a correction of the shock-induced compression front by spreading this compression near the wall, the interaction between the shock and the boundary layer is deemed "weak". This means that the viscous effects do not cause any drastic change in terms of flow behavior: The pressure differential between the front and the rear of the shock does not change compared the equivalent inviscid situation (see figure). It is only smoothed out due to the diffusive character of the subsonic region within the boundary layer.

The interaction between a normal shock and a non-separated boundary layer in the transonic regime also results in an increase of BL displacement thickness (see figure). Notably, the shock causes the subsonic layer to compress progressively, leading to a break-up of the shock into a Mach stem in the supersonic region of the boundary layer. Because this compression is smoothed out across the Mach stem, the entropy increases almost isentropically along each streamline that travels along the supersonic viscous region.

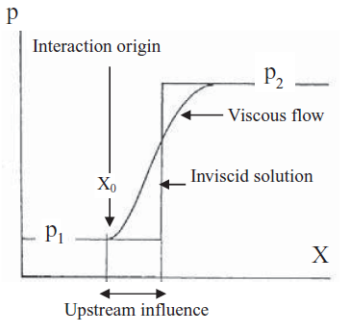

Figure 2.4

This causes the sonic line to slightly overshoot the position of the shock.

It is of interest to note that since transonic SWBLIs feature a substantial subsonic region after the shock, the nature of the interaction is strongly dependent on downstream conditions.

2.2.2.2 Strong shock wave-boundary layer interactions

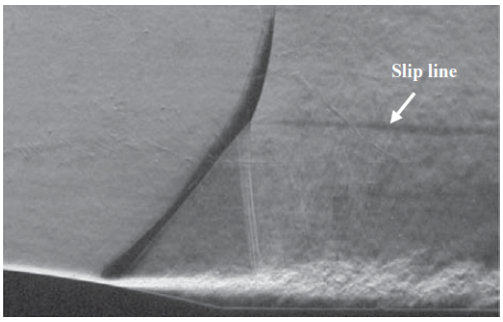

Figure 2.5: A strong SWBLI resulting from the interaction between a normal shock and the boundary layer it contributes to separate on the suction side of an airfoil. A slip line can be seen emanating from the junction between (S1), (S2) and (S3) due to a discontinuity in flow conditions between the zone directly aft the normal shock (S3) and aft (S2).

In the transonic regime, the flow over a curved bump or an airfoil tends to accelerate over the object due to its curvature. This leads to the creation of a pocket of air where the flow becomes supersonic. Such a supersonic flow will generally end with a shock, where the Mach number is equal to unity.

Coincidentally, the curvature of the geometry also causes an adverse pressure gradient in the streamwise direction. This progressive and continuous compression increases shear strain within the boundary layer and eventually leads to flow reversal when the compounded effect of this compression balances out and negates the boundary layer momentum. This effect combines with the terminating shock – the effect of which is to suddenly and violently pressurize the flow – to induce boundary layer separation in the vicinity of the shock foot.

In such cases, the separation of the BL acts as a viscous wedge for the external inviscid flow. This causes a first compression leading to an oblique shock (S1). Since an oblique shock is weaker than a strong shock, the flow remains supersonic upon crossing this first shock, before reaching a near-normal shock (S2) which forms a shock-leg. These two shocks meet at a junction and combine into a normal shock (S3) which causes a stronger compression of the flow. Since the flow undergoes a more progressive compression through (C1) and (C2) rather than by flowing through (C3), the compression along the lower part of the SWBLI happens in a nearly isentropic fashion while compression through (C3) is dominated by irreversible transformations. This results in a slip line at the junction between (C1), (C2) and (C3) – see figure 2.5 – where the flow on the upper side of the slip line and on the lower side have a different Mach number, density and temperature.

The SWBLI is hence described by Babinsky and Harvey, 2011 as a phenomenon that emanates from the competition between the viscous effects that largely dictate flow behavior in the boundary layer on one hand, and the intense pressure gradients caused by the shock wave on the other hand. As Délery, 2001 mentions, the boundary layer is subjected to a retardation effect that is accentuated by the presence of the shock, meaning that the flow is considerably slowed down due to the adverse pressure gradient which forces the flow backwards until the forward momentum of the near-wall layers cancels out. That is caused by the fact that the stagnation pressure decreases within a boundary layer as we approach the wall. From Bernoulli's equation, the stagnation pressure is given as the sum of the static pressure P and the dynamic pressure $\rho V^2/2$ where V is the flow velocity. Since the stagnation pressure remains nearly constant along streamlines and considerably decreases near the wall, a sudden compression results in a much reduced flow velocity.

This ultimately contributes to the formation of a recirculation bubble at the shock foot (flow reversal) in between shocks (S1) and (S2).

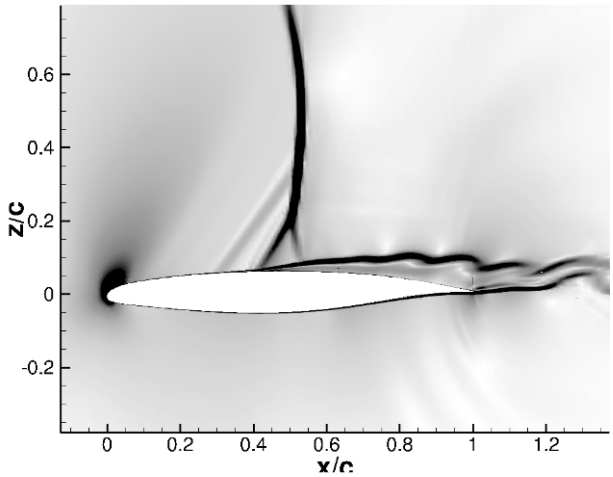

Figure 2.6: Numerical Schlieren from Tô et al., 2019 showing density gradient iso-contours around a supercritical wing. The normal shock and lambda shock system can be easily identified along with a first weaker and more inclined oblique shock that forms before the lambda shock foot.

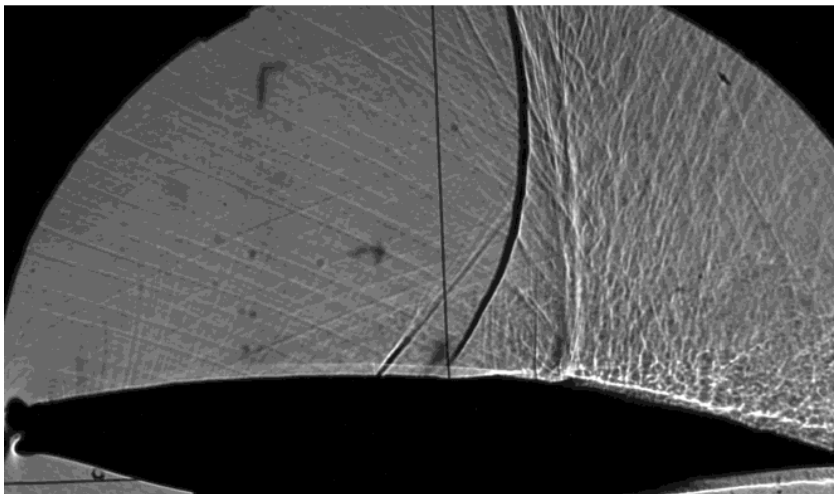

Figure 2.7: Schlieren picture from an experiment by Brutyan, Petrov, and Potapchik, 2016 displaying the presence of a weaker oblique shock before the SWBLI.

The flow is then pushed upstream and upwards, forming a viscous wedge within the subsonic part of the boundary layer which contributes to more

progressive compressions in some cases as was observed in Tô et al., 2019 (see for example fig. 2.6) or Brutyan, Petrov, and Potapchik, 2016 in fig. 2.7. In such circumstances, a laminar-turbulent transition can cause the boundary layer to thicken up, creating a first weaker – and more inclined – oblique shock before adverse pressure gradient effects compress the flow more significantly, inducing the more radical phenomenons described above. A high curvature radius can also be the root of such a phenomenon, where the gentle adverse pressure gradient leads to a gradual thickening of the boundary layer and the emergence of an array of oblique shocks until a more sudden compression occurs.

2.2.3 Shock motion unsteadiness as the result of strong SWBLI

Unsteadiness in SWBLI has been observed for a long time, such as by Seegmiller, Marvin, and Levy, 1978, McDevitt, Levy Jr., and Deiwert, 1976, Levy Jr., 1978, Marvin, Levy Jr., and Seegmiller, 1979, Davis and Malcolmf, 1980 in both experimental and numerical analyses and have more recently been investigated by Jacquin et al., 2005, Jacquin et al., 2009 in experimental studies. Such unsteadiness is characterized by a concerted oscillatory motion of the shock wave and boundary layer system, and such phenomena usually happen around frequencies of typically 100 Hz. They can be triggered by varying causes, such as through disturbances in the incoming flow or due to perturbations happening within the incoming boundary layer. Sometimes, they are triggered by the unsteady behavior of the separation bubble that lies beneath the shock.

In the event of a strong shock wave-boundary layer interaction, where the flow is subsonic behind the shock, pressure fluctuations that happen aft the shock – whether they are forced by an external system or a consequence of the unsteady flow physics that happen due to the presence of the body – can travel back upstream and affect both its strength and its position, as well as its unsteady behavior. One of the first attempts to model and predict this behavior was produced by Lee, Murty, and Jiang, 1994 who studied the propagation of waves emanating from the trailing edge in transonic flows by solving the nonlinear transonic small disturbance equation in two dimensions:

$$\begin{aligned} M_\infty^2 \kappa^2 \partial_{tt}\phi + 2M_\infty \kappa \partial_{xt}\phi \\ = \left(1 - M_\infty^2 - (\gamma+1)M_\infty^2 \partial_x \phi\right) \partial_{xx}\phi + \partial_{yy}\phi \end{aligned} \tag{2.1}$$

where M_∞ here is the freestream Mach number, ϕ is the velocity potential such that $\mathbf{U}_\infty = \nabla\phi$, and κ is the reduced frequency of the oscillating wave source.

This observation was preceded by Tijdeman, 1977. Upon studying the flow behaviors around oscillating airfoils in the transonic regime, the latter coined the term "Kutta waves" when designating the wave disturbances travelling from the trailing edge due to the interaction between shear layer vorticity and the trailing edge of the airfoil. This denomination comes from the observation that the Kutta condition does not hold true at all times, especially on an airfoil with a truncated trailing edge. Instead, the boundary condition that is applied in these cases is the unsteady Kutta condition, which stipulates that there should be no pressure jump or velocity discontinuity across the trailing edge Ayton, Gill, and Peake, 2016. Any vortex travelling towards the trailing edge will create a fluctuation of circulation about the airfoil, generating dipole acoustic sources at the origin of the so-called "Kutta waves" being generated at the trailing edge. These waves are now broadly studied in the aeroacoustic field, such as by Roger, Moreau, and Kucukcoskun, 2015 or Wolf and Lele, 2012, and have been identified as acoustic waves being generated by the interaction of coherent vortices travelling past the trailing edge of an airfoil, representing one of the main mechanisms that cause tonal noise behind streamlined and bluff bodies.

Both Tijdeman, 1977 and Lee, Murty, and Jiang, 1994 presumed that these acoustic waves were responsible for the shock unsteadiness they observed, and more particularly for the lag between airfoil oscillation and the shock response. It was thus suspected that a feedback mechanism based on the transport of information towards the shock through these acoustic waves and in the opposite direction was underlying the oscillatory shock motion. In conjunction with the nonlinear transonic small disturbance equation used to model the propagation of the waves, Tijdeman produced an empirical formula to compute the time T it takes for a pressure signal to travel from the trailing edge to the shock position x_S:

$$T = -\int_{x=c}^{x=x_S} \frac{\mathrm{d}x}{(1 - M_{\mathrm{loc}})a_{\mathrm{loc}}} \tag{2.2}$$

where c is the chord of the airfoil (hence $x = c$ is the position of the trailing edge), M_{loc} is the local Mach number and a_{loc} is the local speed of sound.

This formula produced good agreements with experimental results obtained for an NLR 7301 airfoil at a Mach number of 0.7, an angle of attack of 3 degrees and an unsteady pitch motion of ± 1 degrees and Lee, Murty, and Jiang, 1994 verified that the empirical formula approximates the numerically computed delay quite well. This result allows to correlate the shock motion to the time it takes for a wave-like disturbance to travel upstream.

2.2.4 The buffet instability

In any case, this feedback mechanism is only one of the many possible reasons explaining shock unsteadiness. In the case of airfoils, where shock-induced separation is important, the unsteadiness of the SWBLI can produce modifications of the global flowfield. In fact, the pressure increase aft the shock can lead to the reinforcement of the shock – whether it be through a constructive wave interference due to Kutta waves travelling upstream, or due to the thickening and pressurization of the boundary layer – causing the shock to travel upstream while the strengthened shock contributes to thicken up the boundary layer even more and displace the separation point further upstream. This is because the relative velocity between the shock and the incident flow increases, leading to a larger incident Mach number hence a stronger compression of the boundary layer, driving it upwards and causing more shear. However, as the shock moves towards the leading edge of the airfoil, the downstream pressure decreases and the shock is weakened since the airflow has a relatively small leeway to accelerate to supersonic speeds. This contributes to a diminished separation and the boundary layer appears to thin down, deflating towards the airfoil, causing the shock to travel downstream again since the pressure after the shock tends to decrease. The dynamics of both the shock wave and boundary layer become extremely intricate, such that it is difficult to identify which phenomenon comes first. They most realistically influence each other, resulting in a feedback loop wherein the behavior of the shock influences the behavior of the boundary layer, which then accentuates the motion of the former and so forth while their common dance is influenced by downstream flow conditions. Such a phenomenon is called **transonic buffet** and it can be particularly damaging to wing structure since it comes with intense and unsteady pressure fluctuations on the

surface of the wing. These quasi-periodic disturbances can even interact with the structural modes of the airframe since the natural vibrational modes of a wing happen at neighboring frequencies. This induces a resonant motion of the wing, sometimes resulting in aeroelastic flutter during flight and possibly leading to a destructive instability.

Navier-Stokes simulations by Bouhadji and Braza, 2003 had analysed shock-vortex interactions and their impact on the upstream supersonic flow region, through the effect of compressibility waves in the transonic regime around a NACA0012 airfoil at zero incidence and a Reynolds number of 10^4. These studies analyzed the influence of the downstream unsteadiness on the upstream supersonic regions in the Mach number range $0.7 - 0.9$ that leads to transonic buffet in the Mach range $0.7 - 0.8$. Furthermore, DNS by Bourdet et al., 2003 made evidence of the critical conditions for the appearance of the transonic buffet by means of the Landau oscillator model applied on the DNS results.

It becomes essential to predict the onset of transonic buffet and mitigate its effects, or find a means to eliminate it altogether.

2.3 SWBLI mitigation and drag - reduction techniques in the transonic regime

SWBLI causes shock-induced boundary layer separation in many instances, which forces the BL to become turbulent resulting in more friction drag on the surface of the body. Additionally, the interaction between the separated boundary layer strengthens the shock in return as it acts as a viscous wedge to the external flow. This mutual reinforcement means that wave drag is also increased since the entropy produced by strong shocks is superior to the entropy increase due to weak shocks.

In order to reduce the intensity of these phenomena, some authors resort to flow control using diverse methods to modify the SWBLI, either by decreasing the shock strength or by delaying boundary layer transition. This can be done using different techniques that involve artificially pumping energy into the boundary layer or converting part of its kinetic energy into rotational modes to increase its momentum and alleviate its tendency to separate. These techniques are hereby summarized:

2.4 SWBLI mitigation and drag reduction techniques in the transonic regime

SWBLI causes shock-induced boundary layer separation in many instances, which forces the BL to become turbulent resulting in more friction drag on the surface of the body. Additionally, the interaction between the separated boundary layer strengthens the shock in return as it acts as a viscous wedge to the external flow. This mutual reinforcement means that wave drag is also increased since the entropy produced by strong shocks is superior to the entropy increase due to weak shocks.

In order to reduce the intensity of these phenomena, some authors resort to flow control using diverse methods to modify the SWBLI, either by decreasing the shock strength or by retardating boundary layer transition. This can be done using different techniques that involve artificially pumping energy into the boundary layer or converting part of its kinetic energy into rotational modes to increase its momentum and alleviate its tendency to separate. These techniques are hereby summarized:

2.4.1 Drag reduction using bumps

In order to reduce wave drag, which is caused by the presence of a shock wave around the wing inducing a brutal flow compression, some researchers devised Shock Control Bumps (hereby denoted SCB) the shape of which allows to delay the onset of buffet for transonic wings. Finite-span SCBs act by creating streamwise vorticity. Such vortices contribute to re-energize the boundary layer which is retardated due to the adverse pressure gradient. This passive device uses vortices to suck down the boundary layer and limit its separation aft the bump.

As such, experimental studies were performed by Bruce and Colliss, 2015 on the shape and spanwise distribution of SCBs that would allow to reduce wave drag on laminar-flow airfoils. Others, such as Wong et al., 2008 and König et al., 2009 employed both experimental and numerical analysis – or only numerics such as Qin et al., 2000 to investigate the aerodynamic performance of SCBs. These studies found a benefit in using bumps to control

the position and strength of the shock that forms in the transonic regime. However this also comes with limitations such as a strong dependence of SCBs to flow conditions including shock strength and position as well as the adverse pressure gradient aft the shock. The installation of SCBs also represents an issue when the aircraft is flying in other regimes. The impossibility to move SCBs along the surface of the lifting surface or remove them whenever they are not needed anymore represents a technological hurdle.

2.4.2 Drag reduction using vortex generators

In the same vein as Shock Control Bumps, Vortex Generators (VGs) have been vastly employed in the transonic regime but also for other flight phases and industrial applications such as the automotive or naval industries.

They act by creating strong streamwise vortices that produce an intense downwash to keep the boundary layer attached to the surface of the body. Such VGs can be mechanical and passive (cf. Gageik et al., 2018), taking the shape of small wedges protruding on the lifting body placed at an angle with respect to the flow direction, but some authors such as Ramaswamy and Schreyer, 2021 have employed vortex generator jets, sometimes called air-jet vortex generators, to control shock wave boundary layer interactions.

And despite their positive influence on wave drag in specific conditions, they also contribute to the generation of shape drag since their action on the flow creates flow separation and intense vortices which carry away part of the useful kinetic energy of the flow (Méndez and Gutiérrez, 2018).

References

Ayton, Lorna J, J R Gill, and N Peake (2016). "The Importance of the Unsteady Kutta Condition when Modelling Gust-Aerofoil Interaction". In.

Babinsky, H. and J. K. Harvey (2011). *Shock Wave-Boundary Layer Interactions*. ISBN: 9780521848527.

Bouhadji, A and M Braza (2003). "Organised modes and shock–vortex interaction in unsteady viscous transonic flows around an aerofoil: Part II: Reynolds number effect". In: *Computers & Fluids* 32.9, pp. 1261–1281. ISSN: 0045-7930. DOI: 10.1016/S0045-7930(02)00101-9.

Bourdet, S. et al. (2003). "Direct Numerical Simulation of the Three-Dimensional Transition to Turbulence in the Transonic Flow around a Wing". In: *Flow, Turbulence and Combustion (formerly Applied Scientific Research)* 71.1-4, pp. 203–220. ISSN: 1386-6184. DOI: 10.1023/B:APPL.0000014932.28421.9e.

Bruce, P. J.K. and S. P. Colliss (2015). "Review of research into shock control bumps". In: *Shock Waves* 25.5, pp. 451–471. ISSN: 09381287. DOI: 10.1007/s00193-014-0533-4.

Brutyan, M., A. Petrov, and A. V. Potapchik (2016). "New Method of Transonic Buffet Decreasing on Supercritical Airfoil". In.

Davis, Sanford S and Gerald N Malcolmf (1980). "Transonic Shock-Wave / Boundary-Layer Interactions on an Oscillating Airfoil". In: *AIAA Journal* 18.11, pp. 1306–1312.

Délery, J. M. (2001). "Shock Wave/Boundary Layer Interactions". In: *Handbook of Shock Waves*, pp. 205–I. DOI: 10.1016/B978-012086430-0/50024-5.

Frey, Manuel (1998). "Shock Patterns in the Plume of Overexpanded Rocket Nozzles". In: ed. by ESA SP R. A. Harris. Paris: European Space Agency (ESA), 1999, pp. 395–402. ISBN: 9290927046.

Gadd, G. E. (1958). "Interactions between shock waves and boundary layers". In: *Grenzschichtforschung / Boundary Layer Research*, pp. 239–255. DOI: 10.1007/978-3-642-45885-9_20.

Gageik, M. et al. (2018). "Pressure wave damping in transonic airfoil flow by means of micro vortex generators". In: *Aerospace Science and Technology* 81.M, pp. 65–77. ISSN: 12709638. DOI: 10.1016/j.ast.2018.05.011.

Giannelis, Nicholas F., Oleg Levinski, and Gareth A. Vio (July 2018). "Influence of Mach number and angle of attack on the two-dimensional

transonic buffet phenomenon". In: *Aerospace Science and Technology* 78, pp. 89–101. ISSN: 12709638. DOI: 10.1016/J.AST.2018.03.045.

Jacquin, L. et al. (2009). "Experimental Study of Shock Oscillation over a Transonic Supercritical Profile". In: *AIAA Journal* 47.9, pp. 1985–1994. ISSN: 0001-1452. DOI: 10.2514/1.30190.

Jacquin, Laurent et al. (2005). "An Experimental Study of Shock Oscillation over a Transonic Supercritical Profile". In: *35th AIAA Fluid Dynamics Conference and Exhibit*. Reston, Virigina: American Institute of Aeronautics and Astronautics. ISBN: 978-1-62410-059-8. DOI: 10.2514/6.2005-4902.

König, Benedikt et al. (2009). "Numerical and Experimental Validation of Three-Dimensional Shock Control Bumps". In: *Journal of Aircraft* 46.2, pp. 675–682. ISSN: 0021-8669. DOI: 10.2514/1.41441.

Kundu, P. K., I. M. Cohen, and D. R. Dowling (2012). "Compressible Flow". In: *Fluid Mechanics*, pp. 729–778. DOI: 10.1016/B978-0-12-382100-3.10015-0.

Lee, B. H. K., H. Murty, and H. Jiang (1994). "Role of Kutta waves on oscillatory shock motion on an airfoil". In: *AIAA Journal* 32.4, pp. 789–796. ISSN: 0001-1452. DOI: 10.2514/3.12054.

Levy Jr., Lionel L. (1978). "Experimental and Computational Steady and Unsteady Transonic Flows about a Thick Airfoil". In: *AIAA Journal* 16.6, pp. 564–572. ISSN: 0001-1452. DOI: 10.2514/3.60935.

Marvin, J. G., L L Levy Jr., and H. L. Seegmiller (1979). "Aerospace Sciences Meeting". In: *Physics*. DOI: Doi10.1109/Icsssm.2006.320779.

McDevitt, John B., Lionel L. Levy Jr., and George S. Deiwert (1976). "Transonic Flow about a Thick Circular-Arc Airfoil". In: *AIAA Journal* 14.5, pp. 606–613. ISSN: 0001-1452. DOI: 10.2514/3.61402.

Méndez, B and R Gutiérrez (2018). "Non-conventional vortex generators calculated with CFD". In: p. 22029. DOI: 10.1088/1742-6596/1037/2/022029.

Paladini, Edorado et al. (2019). "Transonic buffet instability: From two-dimensional airfoils to three-dimensional swept wings". In: *Physical Review Fluids* 4.10, p. 103906. ISSN: 2469990X.

Piponniau, Sébastien (2009). "Instationnarités dans les décollements compressibles : cas des couches limites soumises à ondes de choc". In.

Qin, N. et al. (2000). "Active control of transonic aerodynamics using suction, blowing, bumps and synthetic jets". In: *18th Applied Aerodynamics Conference*. DOI: 10.2514/6.2000-4329.

Ramaswamy, Deepak Prem and Anne Marie Schreyer (2021). "Control of shock-induced separation of a turbulent boundary layer using air-jet vortex generators". In: *AIAA Journal* 59.3, pp. 927–939. DOI: 10.2514/1.J059674.

Roger, Michel, Stéphane Moreau, and Korcan Kucukcoskun (2015). "On sound scattering by rigid edges and wedges in a flow, with applications to high-lift device aeroacoustics". In: DOI: 10.1016/j.jsv.2015.10.004.

Seegmiller, H. L., J. G. Marvin, and L. L. Levy (1978). "Steady and unsteady transonic flow". In: *AIAA Journal* 16.12, pp. 1262–1270. ISSN: 00011452. DOI: doi:10.2514/6.1978-160.

Shang, J. S., Jr. Hankey W. L., and C. H. Law (1976). "Numerical simulation of shock wave-turbulent boundary layer interaction". In: *aiaa*.

Sundén, Bengt and Juan Fu (2017). "Introduction". In: *Heat Transfer in Aerospace Applications*, pp. 1–17. DOI: 10.1016/B978-0-12-809760-1.00001-6.

Tijdeman, H (1977). "Investigation of the transonic flow around oscillating airfoils". In: *National Aerospace Lab. Amsterdam, Netherlands* TR-77-090U. DOI: b07421b9-136d-494c-a161-b188e5ba1d0d.

Tô, J.-B. et al. (2019). "Effects of vibrating and deformed trailing edge of a morphing supercritical airfoil in transonic regime by numerical simulation at high Reynolds number". In: *Journal of Fluids and Structures*. ISSN: 0889-9746. DOI: 10.1016/J.JFLUIDSTRUCTS.2019.02.011.

Wolf, William R. and Sanjiva K. Lele (Nov. 2012). "Trailing-edge noise predictions using compressible large-eddy simulation and acoustic analogy". In: *AIAA Journal* 50 (11), pp. 2423–2434. DOI: 10.2514/1.J051638.

Wong, W. S. et al. (Sept. 2008). "A combined experimental and numerical study of flow structures over three-dimensional shock control bumps". In: *Aerospace Science and Technology* 12 (6), pp. 436–447. DOI: 10.1016/J.AST.2007.10.011.

Chapter 3

Hybrid and bio-inspired morphing

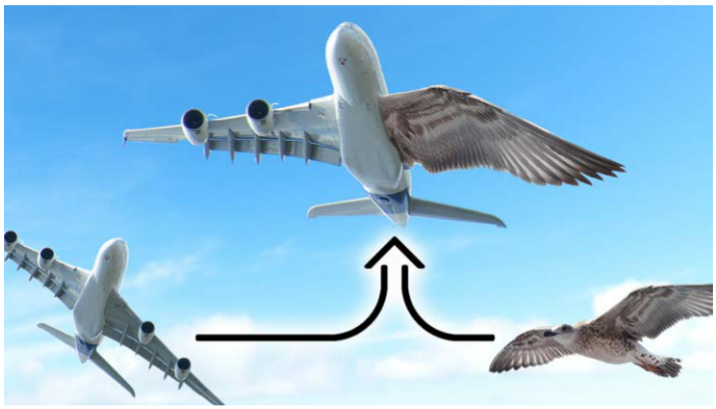

Figure 3.1: In the Smart Morphing and Sensing (SMS) research project, bio-inspired morphing draws inspiration from the wings of birds of prey to produce deformable wings that can reach better aerodynamic performance than conventional lifting surfaces in all phases of flight. Reproduced with permission from G. Jodin's PhD thesis

3.1 What is morphing?

A morphing structure is one that can be deformed easily and continuously in order to achieve varying degrees of performance. A compliant design, as

part of a dynamic system can thus be warped to achieve optimal behaviour at all times, no matter which operational conditions it is subjected to.

In 2002, McGowan et al., 2002 in their report on morphing activities defined morphing as a technology that achieves:

1. efficiency
2. multi-point adaptability
3. large structural shape changes
4. small structural shape changes (so-called "Micro-Aero Adaptive Control")

Morphing thus addresses the problematic of ever more complex designs with a more efficient structure or manages to reach better efficiency in terms of energy expenditure.

Similarly, morphing is characterized by structures that can adapt to changing flight conditions, hence the requirement for multi-point adaptability, where "multi-point" stands for multiple flight scenarios that can arise.

Morphing technology must also allow high-amplitude deformations as well as small-scale deformations to act on the various length and time scales that pertain to real flows in flight conditions.

3.2 Morphing as a bio-inspired technology

Morphing takes its many sources of inspiration from nature in order to achieve optimality since natural selection has allowed many animals in the animal kingdom to adapt to their environment, selective pressure enabling only the favorable genes to be transmitted across the generations. As such, birds, fishes, mammals, insects and many other living – as well as non-living – beings that possess DNA have evolved in such a way that they can best foster the resources available to them.

Birds are believed to have evolved from early theropods. Recent discoveries (Bock, 2000) show that many of these small dinosaurs were covered in feathers but many of them did not possess the ability to fly although some paleonthologists such as Godefroit et al., 2013 are convinced that by using feathered wings, some animals could have already achieved flight in the

mid-Jurassic period. Ever since, wings have evolved to include additional features such as the alula, a thumb-like extension supporting feathers that can be extended forward and upwards to avoid stall in low-speed and high AoA conditions. Most notably, there exists a broad diversity of wing shapes in Nature, each of which are adapted to different types of flight: The design of a wing is tailored to a particular use at distinct Reynolds and Mach regimes. Its general shape and size also satisfy other requirements such as wing loading and structural integrity. But compliance and controllability adds efficiency and flexibility to an already optimized wing shape. This proves to be crucial in the avian world, since these characteristics allow birds to quickly change direction and adapt to fluctuating circumstances, which would not be possible if wings were rigid.

Some studies such as Ponitz et al., 2014, Ponitz, Triep, and Brücker, 2014 have thus investigated the three-dimensional behavior of the flow around falcon-shaped bodies in a bid to understand how birds of prey – in particular falcons – can so effectively reach high velocities during their dive. Others, such as Lee et al., 2015, Heerenbrink and Hedenström, 2017 or Heerenbrink, Johansson, and Hedenström, 2017 analyzed the influence of protrusions on the wings having a direct effect on the generation or alleviation of marginal vortices, hence improving flight performance during gliding flight.

In other domains of fluid mechanics, the study of bird flight has also brought to light several ways feathers can influence flight for the better. For example, it is worth noticing that owls generate very little noise when they glide towards their prey. Some authors such as Geyer, Sarradj, and Fritzsche, 2014 or Jaworski and Peake, 2020 strive to understand how serration length and shape of an owl's plumage acts to diminish tonal noise through destructive interference. Another article by Liu, Jawahar, and Azarpeyvand, 2016 points to the action of flow three-dimensionality near serrated trailing edges as a main contributor in the reduction of acoustic sources. Since feathers allow the flow to permeate from the pressure side of the wing towards the suction side, serration creates vorticity that contributes to quickly decay turbulent energy in the wake, leading to a reduction of "self-noise" which comes from the interaction between boundary layer eddies propagating downstream and the trailing edge.

3.2.1 A few examples of research works that employ morphing technologies for aeronautical applications

Bio-inspired morphing applied to lifting surfaces aims to improve upon existing designs or create novel technological approaches on the basis of existing systems and designs in Nature. Drawing inspiration on birds is already a thematic broadly stridden in research.

Indeed, research on morphing technologies attempt to provide an answer to the several problems that arise during take-off, landing and cruise flight. For instance, take-off requires considerable runway lengths to allow the aircraft to reach sufficiently high speeds without which it would struggle to depart from the ground or immediately stall upon lift-off due to the significant angles of attack that would be required.

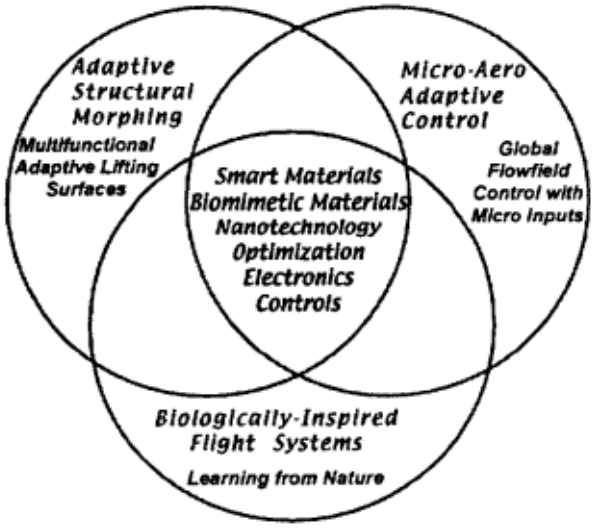

Figure 3.2: Bio-inspired morphing comes from the conjunction of different fields according to McGowan et al., 2002

This is evidenced by several research programs and the morphing prototypes that were developed across the world for the past two decades, such as NASA's **Variable Camber Continuous Trailing Edge Flap** (VCCTEF) Kaul and Nguyen, 2014 and Nguyen et al., 2015 which endeavored to tackle the issue of wings deforming past their optimal operational design due to their

structural flexibility. In order to reach optimality in these ever-changing conditions, the wing trailing edge is replaced by a compliant trailing edge that is segmented along the chordwise direction.

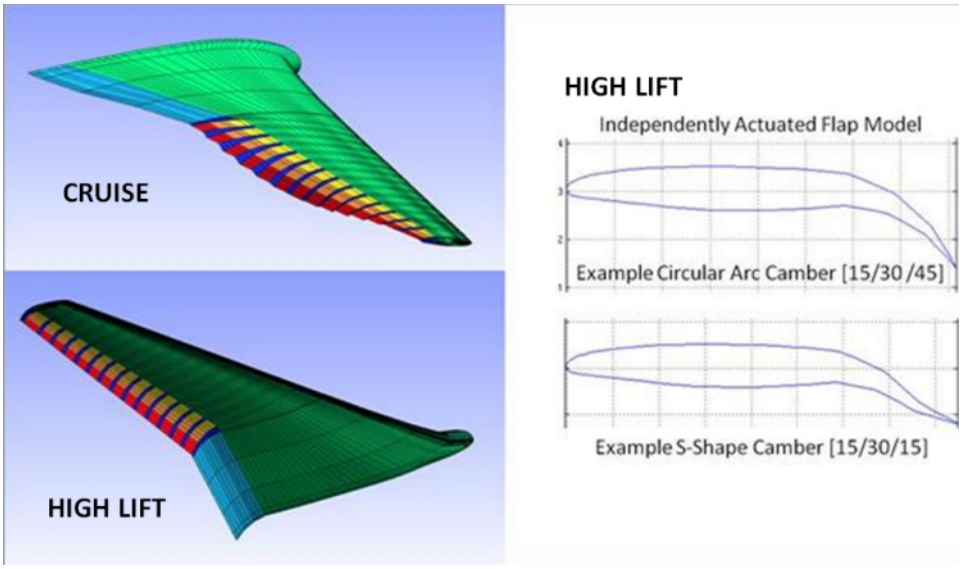

Figure 3.3: On the left, the figures show the Cruise and High-Lift configurations that are studied by Nguyen et al., 2015

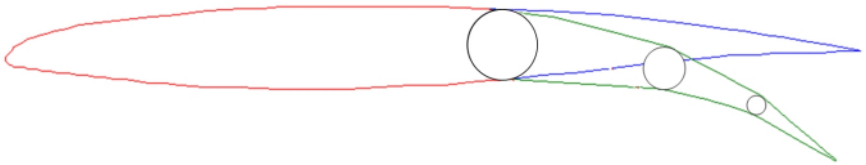

Figure 3.4: On the left, the figures show the Cruise and High-Lift configurations that are studied by Nguyen et al., 2015

Several designs were developed during this program, one of them consisting of an articulated trailing edge with several hinges linking the different parts. Another design, named Mission Adaptive Compliant Wing (MACW) Hetrick et al., 2007, is based on a deformable skin that is elastically strained.

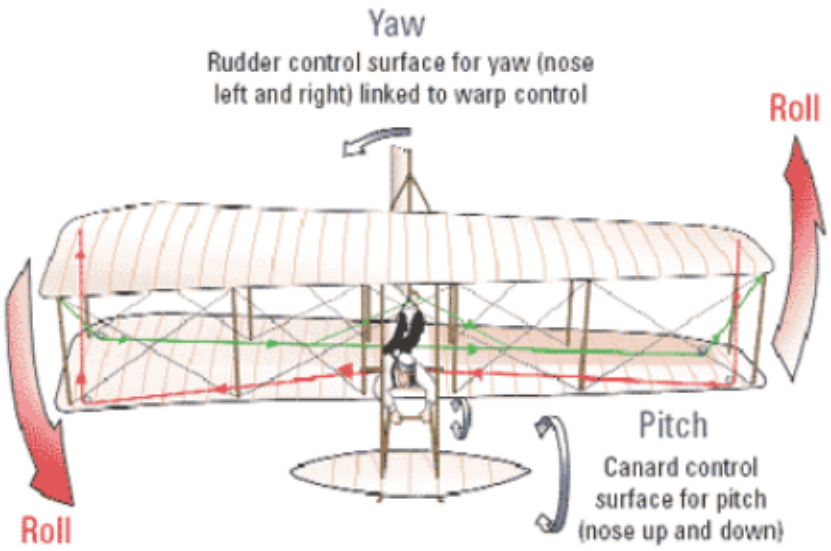

Figure 3.5: Figure showing wing warping on an early Wright-brothers aircraft. This actuation was a precursor of modern morphing techniques.

3.3 The SMS project

The Smart Morphing and Sensing (SMS[1]) european research program was a three-year multi-disciplinary project coordinated by IMFT aiming at developing, studying and testing novel compliant technologies based on electroactive and bio-inspired morphing applied to aeronautical systems in order to improve flight performance whether it be in take-off, landing or cruise phases.

This is achieved through the use of smart-materials that can be deformed at will to imprint an optimal shape to the wing under any flight condition, thanks to commands that are tuned beforehand to attain such behavior. These commands are dictated by flight data, hence a reliance on high-performance sensors and real-time data acquisition to accurately and rapidly detect the transport of aerodynamic stresses along the surface of the wing. This way, it is possible to recognize patterns that indicate the nature of the flow and anticipate any fast modifications that may occurr. Real-time data acquisition was made possible via the use of sensors employing fiber Bragg

[1] http://smartwing.org/SMS/EU/

gratings coordinated by a dedicated controller that interfaces both actuators and sensors.

The prototypes that were developed during the SMS project relied on the combined use of low-speed actuators responsible for large-scale deformations and high-speed actuators performing small deformations. The former are made up of Shape Memory Alloys positioned underneath the skin of the wings and acting like muscles, alternatively contracting or extending depending on the direction of the deformation. The latter are comprised of piezo-actuators arranged in a spanwise manner along the trailing edge of the wing, and are made to vibrate at frequencies of the order of a few hundred Hertz. This hybrid combination of low time-scale and high time-scale actuators allows morphing to tackle different flow phenomenons depending on the flight regime. As such, low-speed flight involves slow-developing yet energetic coherent structures that may be more efficiently dealt with thanks to low-speed actuation. Conversely, high-speed flight taking place at very high Reynolds numbers sees the emergence of a broader turbulence spectrum requiring the ability to manipulate high-frequency vortices.

To perform this extensive study, both experiments in wind tunnels and numerical analysis using high-fidelity Computational Fluid Dynamics (CFD) simulations were performed among the different partners of this European consortium. The airfoil used for this analysis is based on an A320 mid-section airfoil. Numerical simulations were used to find the optimum actuation modes and sensor position while experiments have studied the improvement of performance in cruise flight, take-off and landing.

3.3.1 Inception of the Smart Morphing and Sensing research program and first prototypes

The multidisciplinary research team composed of the two research Institutes IMFT and LAPLACE created and lead the Morphing platform www.smartwing.org since 2010 thanks to three federative national research programmes EMMAV, DYNAMORPH and SMARTWING, all of which were sponsored by the STAE-RTRA Foundation : *Sciences et Techniques pour l'Aéronautique et l'Espace - Réseau Thématique de Recherche Avancée.* In this context, the study of suitable electroactive actuators was developed, able

to operate at different time and length scales, as required by the structure of the Turbulence spectrum that is able to be optimally manipulated thanks to these actuations. Concerning a low frequency scale (order of 1Hz) but offering large deformation capabilities in the order of 15-20% of the wing's chord, Shape Memory Alloys have been embedded under the skin of the lifting structure.

The choice to employ Shape Memory Alloys quickly prevailed on the basis of the conclusions drawn from another research program called EMMAV (Electroactive Morphing for Micro Air Vehicles). Chinaud et al., 2012 studied SMA actuators composed of an alloy of Nickel and Titanium. SMAs are materials that are characterized by a thermomechanical behavior dictated by the existence of two phases depending on the temperature of the material: an austenitic phase that is stable at high temperature and a martensitic phase stable at low temperatures. Going from one phase to the other by increasing or decreasing the temperature of the material causes a phase transformation which rearranges the crystalline nanostructure of the material, causing strain.

As part of the EMMAV program, the LAPLACE laboratory devised a deformable plate using an SMA to perform a thorough characterization of the material, validate it and calibrate control laws. As part of their theses, G. Jodin and J. Scheller have also developed a vibrating trailing edge that uses piezo-electric materials, employing mathematical models and Finite Elements Analysis (FEA) to find the vibrational modes of the actuated trailing edge. These studies helped evolve the first morphing wing prototypes – the first one based on a NACA0012 wing and investigated as part of the DYNAMORPH research project Chinaud et al., 2014, Scheller et al., 2015 and Jodin et al., 2017 – that would serve to investigate flow physics in wind tunnel experiments during the SMS project.

The streaklines here denote the motion of particles that are being advected by the flow, clearly displaying a distinctive flow pattern characterized by the presence of intense recirculation in the vicinity of the trailing edge as well as both small and bigger coherent vortices that accompany and develop turbulence growth.

Camber control in the rear part of the airfoil can be achieved with the use of a Shape Memory Alloy (SMA) made of a lattice of

By heating these SMA wires (temperature range: 20°C -> 80°C), a contraction is obtained, which pulls on each individual wire, allowing the wing to be cambered downwards or upwards depending on which wire is being actuated.

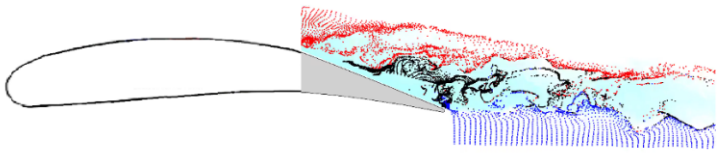

Figure 1.3: *Development of interfaces and vortices in the wake; an illustration of the morphing effects.*

Figure 3.6: PIV results from the thesis of G. Jodin showing the motion of streaklines near the trailing edge of a deformable A320 airfoil. Image reproduced from the thesis of N. Simiriotis.

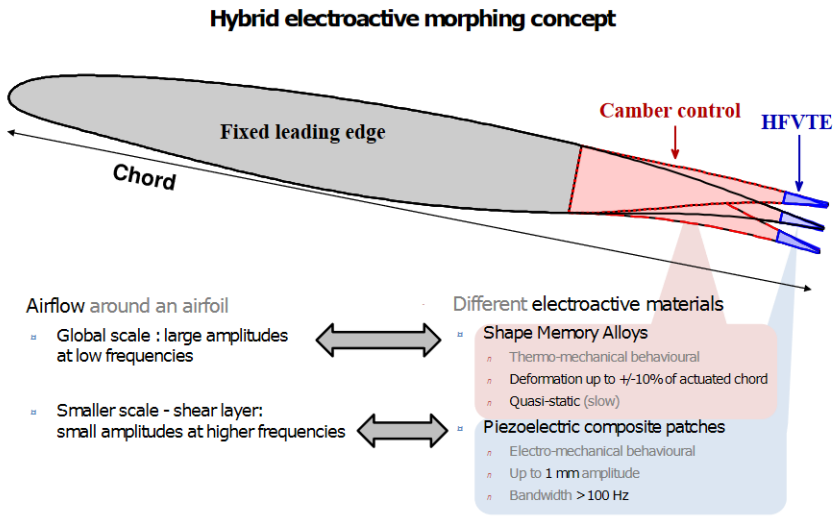

Figure 2.2: Concept of the hybrid morphing, using electroactive materials.

Figure 3.7: Image taken from Jodin's thesis showing the different actuators employed in order to govern the deformation of a morphing wing.

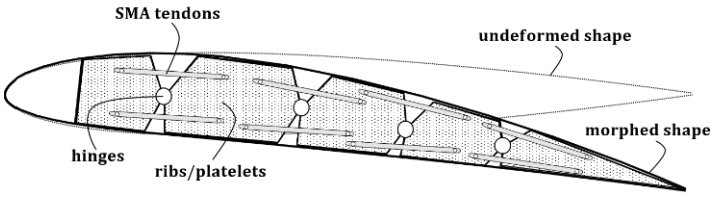

Figure 5.1: *An airfoil architecture with SMAs: placement of the hinges and of pairs of SMA tendons to adjust the aerodynamic shape.*

Figure 3.8: Image taken from Simiriotis's thesis showing the way a wing section can have its shape manipulated as a result of tying articulated ribs with the use of agonist and antagonist Shape Memory Alloys (SMA) playing a similar role to muscles and tendons in a bird wing

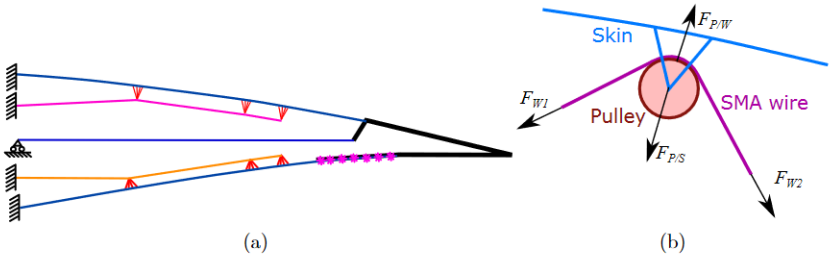

Figure 2.6: (a) Geometry of the finite element model. (b) Illustration of the pulley/wire link.

Figure 3.9: Image taken from Jodin's thesis that focuses on the way the Finite Element Model is set-up in order to compute the efforts produced by SMA wires to achieve any given airfoil deformation. A similar FEM model is used in Simiriotis's thesis, wherein the last 30% of the wing chord is actuated.

References

Bock, Walter J. (Aug. 2000). "Explanatory History of the Origin of Feathers". In: *Integrative and Comparative Biology* 40 (4), pp. 478–485. ISSN: 1540-7063. DOI: 10.1093/ICB/40.4.478.

Chinaud, M. et al. (2012). "Thermo-mechanical coupling in Nitinol. Application to an electro-morphing plate". In: *Proceedings - 2012 20th International Conference on Electrical Machines, ICEM 2012*, pp. 2580–2584. DOI: 10.1109/ICELMACH.2012.6350249.

Chinaud, M. et al. (2014). "Trailing-edge dynamics and morphing of a deformable flat plate at high Reynolds number by time-resolved PIV". In: *Journal of Fluids and Structures* 47, pp. 41–54. ISSN: 0889-9746. DOI: 10.1016/J.JFLUIDSTRUCTS.2014.02.007.

Geyer, T., E. Sarradj, and C. Fritzsche (2014). "Measuring owl flight noise". In: *undefined*.

Godefroit, Pascal et al. (Jan. 2013). "Reduced plumage and flight ability of a new Jurassic paravian theropod from China". In: *Nature Communications 2013 4:1* 4 (1), pp. 1–6. ISSN: 2041-1723. DOI: 10.1038/ncomms2389.

Heerenbrink, Marco Klein and Anders Hedenström (Feb. 2017). "Wake analysis of drag components in gliding flight of a jackdaw (Corvus monedula) during moult". In: *Interface Focus* 7 (1). DOI: 10.1098/RSFS.2016.0081.

Heerenbrink, Marco Klein, L. Christoffer Johansson, and Anders Hedenström (May 2017). "Multi-cored vortices support function of slotted wing tips of birds in gliding and flapping flight". In: *Journal of the Royal Society Interface* 14 (130). DOI: 10.1098/RSIF.2017.0099.

Hetrick, Joel A. et al. (2007). "Flight testing of Mission Adaptive Compliant Wing". In: *Structural Dynamics and Materials Conference* 1, pp. 92–109. DOI: 10.2514/6.2007-1709.

Jaworski, Justin W. and N. Peake (Jan. 2020). "Aeroacoustics of Silent Owl Flight". In: *Annual Review of Fluid Mechanics* 52, pp. 395–420. DOI: 10.1146/ANNUREV-FLUID-010518-040436.

Jodin, G. et al. (2017). "Dynamics of a hybrid morphing wing with active open loop vibrating trailing edge by time-resolved PIV and force measures". In: *Journal of Fluids and Structures* 74, pp. 263–290. ISSN: 10958622. DOI: 10.1016/j.jfluidstructs.2017.06.015.

Kaul, Upender K and Nhan T Nguyen (2014). "Drag Optimization Study of Variable Camber Continuous Trailing Edge Flap (VCCTEF) Using OVERFLOW". In: ISSN: 2014-2444. DOI: 10.2514/6.2014-2444.

Lee, Sang Im et al. (May 2015). "The function of the alula in avian flight". In: *Scientific Reports* 5. DOI: 10.1038/SREP09914.

Liu, Xiao, Hasan Kamliya Jawahar, and Mahdi Azarpeyvand (2016). "Wake development of airfoils with serrated trailing edges". In: *22nd AIAA-CEAS Aeroacoustics Conference*. DOI: 10.2514/6.2016-2817.

McGowan, Anna-Maria Rivas et al. (July 2002). "Recent results from NASA's morphing project". In: *https://doi.org/10.1117/12.475056* 4698, pp. 97–111. DOI: 10.1117/12.475056.

Nguyen, Nhan T. et al. (2015). "Wind tunnel investigation of a flexible wing high-lift configuration with a variable camber continuous trailing edge flap design". In: *33rd AIAA Applied Aerodynamics Conference*. DOI: 10.2514/6.2015-2417.

Ponitz, Benjamin, Michael Triep, and Christoph Brücker (2014). "Aerodynamics of the Cupped Wings during Peregrine Falcon's Diving Flight". In: *Open Journal of Fluid Dynamics* 04 (04), pp. 363–372. DOI: 10.4236/OJFD.2014.44027.

Ponitz, Benjamin et al. (Feb. 2014). "Diving-flight aerodynamics of a peregrine falcon (Falco peregrinus)". In: *PLoS ONE* 9 (2). DOI: 10.1371/JOURNAL.PONE.0086506.

Scheller, J. et al. (2015). "Trailing-edge dynamics of a morphing NACA0012 aileron at high Reynolds number by high-speed PIV". In: *Journal of Fluids and Structures* 55, pp. 42–51. ISSN: 10958622. DOI: 10.1016/j.jfluidstructs.2014.12.012.

Chapter 4

Numerical methods for solving the turbulent and compressible Navier-Stokes equations

4.1 Introduction

The numerical methods employed for solving the Navier-Stokes equations are summarized below.

The present thesis benefited from the use of a parallel code, Navier-Stokes Multi Block (NSMB - cf. Hoarau et al., 2016 and Vos et al., 1998) jointly developed by several research laboratories forming a European Consortium. This Fortran-based code solves both the compressible and incompressible Navier-Stokes equations. In order to capture turbulent features, it encompasses a wide range of turbulence closure models that can not only be applied to a URANS (Reynolds-Averaged Navier-Stokes) formulation but also to Large-Eddy Simulations (LES) or even to more recent hybrid RANS-LES approaches. The latter combine the advantages of both RANS methods and LES methodology, for it solves for large eddies in outer flow regions, where the mesh resolution requirements are less stringent, while the treatment of near-wall turbulence is left to a URANS model. Such methods were initially devised by Speziale, 1998 and Spalart et al., 1997 who proposed the Detached Eddy Simulation (DES) as a means to tackle the problems that were (and are still) met in solving for fine turbulent structures. As such, LES requires several mesh quality criteria to be respected such as a cell aspect ratio as

close as possible to 1 in all directions (the grid is said to be *isotropic*) so as to not generate high skewness of the vertical velocity as was demonstrated by Nishizawa et al., 2015.

Among the various two-equations models that were implemented in NSMB can be found the $k-\varepsilon$ and $k-\omega$ models and the $k-\tau$ model. Many versions of the $k-\omega$ model are implemented. More sophisticated non-linear models (EARSM and NLEVM) are also implemented based on both $k-\varepsilon$ and $k-\omega$ models.

The $k-\varepsilon$ model requires the solution of transport equations for the turbulent kinetic energy k and the turbulent dissipation ε, the same for $k-\omega$ models. This basis model is typically a "high Reynolds number" model. To take into account for the interaction between turbulence and fluid viscosity, many different low-Reynolds number versions have been implemented. These versions differ in the form of the source terms, in the surface boundary conditions imposed, in the values of closure coefficients and also in the form of the damping functions. They both solve an equation for the isotropic component of the turbulent dissipation. The proposal to use this modified dissipation variable is due to Jones and Launder Jones and Launder, 1972 who cited decisive computational advantages. Moreover Kunz et al. Kunz and Lakshminarayana, 1992 have observed that transporting the exact dissipation may be responsible for near wall instabilities in low-Reynolds number models!

4.2 Governing equations

The conservative form of the Navier-Stokes equations for turbulent flow of a viscous, perfect gas, is expressed as follows:

$$\frac{\partial W}{\partial t}+\frac{\partial f}{\partial x}+\frac{\partial f_v}{\partial x}+\frac{\partial g}{\partial y}+\frac{\partial g_v}{\partial y}+\frac{\partial h}{\partial z}+\frac{\partial h_v}{\partial z}=S$$

where:

$$W = \begin{vmatrix} \overline{\rho} \\ \overline{\rho}\widetilde{u} \\ \overline{\rho}\widetilde{v} \\ \overline{\rho}\widetilde{w} \\ \overline{\rho}\widetilde{E} \\ \overline{\rho}\widetilde{k} \\ \overline{\rho}\widetilde{\varepsilon} \text{ or } \overline{\rho}\widetilde{\tau} \text{ or } \overline{\rho}\widetilde{\omega} \end{vmatrix}$$

$$f = \begin{vmatrix} \overline{\rho}\widetilde{u} \\ \overline{\rho}\widetilde{u}^2 + p^* \\ \overline{\rho}\widetilde{u}\widetilde{v} \\ \overline{\rho}\widetilde{u}\widetilde{w} \\ \overline{\rho}\widetilde{u}\widetilde{E} + \widetilde{u}p^* \\ \overline{\rho}\widetilde{u}\widetilde{k} \\ \overline{\rho}\widetilde{u}\widetilde{\varepsilon} \text{ or } \overline{\rho}\widetilde{u}\widetilde{\tau} \text{ or } \overline{\rho}\widetilde{u}\widetilde{\omega} \end{vmatrix} \qquad g = \begin{vmatrix} \overline{\rho}\widetilde{v} \\ \overline{\rho}\widetilde{v}\widetilde{u} \\ \overline{\rho}\widetilde{v}^2 + p^* \\ \overline{\rho}\widetilde{v}\widetilde{w} \\ \overline{\rho}\widetilde{v}\widetilde{E} + \widetilde{v}p^* \\ \overline{\rho}\widetilde{v}\widetilde{k} \\ \overline{\rho}\widetilde{v}\widetilde{\varepsilon} \text{ or } \overline{\rho}\widetilde{v}\widetilde{\tau} \text{ or } \overline{\rho}\widetilde{v}\widetilde{\omega} \end{vmatrix} \qquad h = \begin{vmatrix} \overline{\rho}\widetilde{w} \\ \overline{\rho}\widetilde{w}\widetilde{u} \\ \overline{\rho}\widetilde{w}\widetilde{v} \\ \overline{\rho}\widetilde{w}^2 + p^* \\ \overline{\rho}\widetilde{w}\widetilde{E} + \widetilde{w}p^* \\ \overline{\rho}\widetilde{w}\widetilde{k} \\ \overline{\rho}\widetilde{w}\widetilde{\varepsilon} \text{ or } \overline{\rho}\widetilde{w}\widetilde{\tau} \text{ or } \overline{\rho}\widetilde{w}\widetilde{\omega} \end{vmatrix}$$

$$f_v = \begin{vmatrix} 0 \\ -{\tau_{xx}}^T \\ -{\tau_{xy}}^T \\ -{\tau_{xz}}^T \\ -\widetilde{u}{\tau_{xx}}^T - \widetilde{v}{\tau_{xy}}^T - \widetilde{w}{\tau_{xz}}^T + {q_x}^T - \sigma_{kx} \\ \sigma_{kx} \\ \sigma_{\varepsilon x} \text{ or } \sigma_{\tau x} \text{ or } \sigma_{\omega x} \end{vmatrix}$$

$$g_v = \begin{vmatrix} 0 \\ -{\tau_{yx}}^T \\ -{\tau_{yy}}^T \\ -{\tau_{yz}}^T \\ -\widetilde{u}{\tau_{yx}}^T - \widetilde{v}{\tau_{yy}}^T - \widetilde{w}{\tau_{yz}}^T + {q_y}^T - \sigma_{ky} \\ \sigma_{ky} \\ \sigma_{\varepsilon y} \text{ or } \sigma_{\tau y} \text{ or } \sigma_{\omega y} \end{vmatrix}$$

$$h_v = \left| \begin{array}{l} 0 \\ -{\tau_{zx}}^T \\ -{\tau_{zy}}^T \\ -{\tau_{zz}}^T \\ -\widetilde{u}{\tau_{zx}}^T - \widetilde{v}{\tau_{zy}}^T - \widetilde{w}{\tau_{zz}}^T + {q_z}^T - \sigma_{kz} \\ \sigma_{kz} \\ \sigma_{\varepsilon z} \ or \ \sigma_{\tau z} \ or \ \sigma_{\omega z} \end{array} \right.$$

$$S = \left| \begin{array}{l} 0 \\ 0 \\ 0 \\ 0 \\ 0 \\ S_k \\ S_\varepsilon \ or \ S_\tau \ or \ S_\omega \end{array} \right.$$

where the Favre average — under the ergodic assumption — is denoted by a tilde symbol on top of the state variable it contributes to average:

$$\widetilde{\Phi}(x) \equiv \frac{\sum_{realizations} \rho_i(x,t)\Phi_i(x,t)}{\sum_{realizations} \rho_i(x,t)} = \frac{\overline{\rho\Phi}}{\overline{\rho}}$$

This density-weighted average is used in highly compressible formulations (typically transonic, supersonic and hypersonic cases) where turbulent fluctuations lead to significant density variations.

- For linear two equations models, the Reynolds tensor can be expressed as such (Boussinesq assumption): $-\overline{\rho u_i'' u_j''} + \frac{2}{3}\bar{\rho}\widetilde{k} = \mu_t \left[\frac{\partial \widetilde{u_i}}{\partial x_j} + \frac{\partial \widetilde{u_j}}{\partial x_i} - \frac{2}{3}\frac{\partial \widetilde{u_k}}{\partial x_k}\delta_{ij} \right]$
- $p^* = p + \frac{2}{3}\rho k$
- ${\tau_{ij}}^T = \overline{\tau}_{ij} + {\tau_{ij}}^t = \overline{\mu}[\frac{\partial \widetilde{u_i}}{\partial x_j} + \frac{\partial \widetilde{u_j}}{\partial x_j} - \frac{2}{3}\frac{\partial \widetilde{u_l}}{\partial x_l}\delta_{ij}] - \overline{\rho u_i'' u_j''} + \frac{1}{3}\overline{\rho u_l'' u_l''}\delta_{ij} = (\overline{\mu} + \mu_t)[\frac{\partial \widetilde{u_i}}{\partial x_j} + \frac{\partial \widetilde{u_j}}{\partial x_j} - \frac{2}{3}\frac{\partial \widetilde{u_l}}{\partial \widetilde{u_l}}\delta_{ij}]$
  The term $(-\frac{1}{3}\overline{\rho u_l'' u_l''}\delta_{ij} = -\frac{2}{3}\bar{\rho}\widetilde{k})$ is substracted here because it has already been added to the pressure term
- ${q_i}^T = \overline{q_i} + {q_i}^t = -(\overline{\lambda} + \lambda_t)\frac{\partial \widetilde{T}}{\partial x_i} = -(\frac{\gamma\overline{\mu}}{\mathrm{Pr}} + \frac{\gamma\mu_t}{pr_t})\frac{\partial \widetilde{T}}{\partial x_i}$
- $\sigma_{ki} = -(\overline{\mu} + \frac{\mu_t}{\sigma_k})\frac{\partial \widetilde{k}}{\partial x_i}$

- $\sigma_{\varepsilon i} = -(\overline{\mu} + \frac{\mu_t}{\sigma_\varepsilon})\frac{\partial \widetilde{\varepsilon}}{\partial x_i}$ and $\sigma_{\tau i} = -(\overline{\mu} + \frac{\mu_t}{\sigma_\tau})\frac{\partial \widetilde{\tau}}{\partial x_i}$ and $\sigma_{\omega i} = -(\overline{\mu} + \frac{\mu_t}{\sigma_\omega})\frac{\partial \widetilde{\omega}}{\partial x_i}$

- $S_k = P_k - \bar{\rho}\widetilde{\varepsilon} + W_k$ and $S_\varepsilon = C_{\varepsilon 1} f_1 \frac{\widetilde{\varepsilon}}{\widetilde{k}} P_k - C_{\varepsilon 2} f_2 \bar{\rho} \frac{\widetilde{\varepsilon}^2}{\widetilde{k}} + W_\varepsilon$ and $S_\tau = (1 - C_{\varepsilon_1} f_1)\frac{\widetilde{\tau}}{\widetilde{k}} P_k + (C_{\varepsilon_2} f_2 - 1)\bar{\rho} + W_\tau$ and $S_\omega = \alpha \frac{\widetilde{\omega}}{\widetilde{k}} P_k - \beta \bar{\rho} \widetilde{\omega}^2 + W_\omega$

- $P_k = -\overline{\rho u_i'' u_j''}\frac{\partial \widetilde{u}_i}{\partial x_j} = \left[\mu_t \left(\frac{\partial \widetilde{u}_i}{\partial x_j} + \frac{\partial \widetilde{u}_j}{\partial x_i} - \frac{2}{3}\frac{\partial \widetilde{u}_k}{\partial x_k}\delta_{ij}\right) - \frac{2}{3}\bar{\rho}\widetilde{k}\right]\frac{\partial \widetilde{u}_i}{\partial x_j}$

4.3 Chien's $k - \varepsilon$ model

The two dimensionless parameters are introduced :

$$Re_t = \frac{k^2}{\varepsilon \nu} \qquad y^+ = \frac{u_\tau y}{\nu}$$

$$S_k = P_k - \overline{\rho}\widetilde{\varepsilon} - \frac{2\overline{\mu}\widetilde{k}}{{y_w}^2}$$
$$S_\varepsilon = C_{\varepsilon_1} f_1 \frac{\widetilde{\varepsilon}}{\widetilde{k}} P_k - C_{\varepsilon_2} f_2 \overline{\rho} \frac{\widetilde{\varepsilon}^2}{\widetilde{k}} - \frac{2\overline{\mu}\widetilde{\varepsilon}}{{y_w}^2} exp(-0.5\ y^+)$$

4.3.1 The model of Chien

Chien, 1982 introduced a $k - \varepsilon$ implementation to predict the correct shape and development of a boundary-layer flow at low Reynolds number. To do so, he chose to adopt the same general approach as the one proposed by Jones and Launder, 1972, but modified it profoundly to adapt this formulation to a more suitable one for the relevant usecase. This work led to altered values for the model constants which are listed here.

The damping functions, closure coefficients and surface boundary condition on ε for the two models are written as follows :

- **damping functions:**
  $f_\mu = 1 - exp(-0.0115\ y^+)$
  $f_1 = 1$
  $f_2 = [1 - 0.22\ exp(-\frac{Re_t^2}{36})]$

- **constants**
  $C_\mu = 0.09$
  $C_{\varepsilon_1} = 1.35$
  $C_{\varepsilon_2} = 1.8$
  $\sigma_k = 1.0$
  $\sigma_\varepsilon = 1.3$

- **boundary conditions at the wall:**
  $k = 0 \quad$ and $\quad \varepsilon = 0$

4.3.2 Implementation of the OES methods

For unsteady separated flows where the statistical models employed in standard RANS are no-longer valid, the OES (Organised Eddy Simulation) approach was implemented in NSMB as an alternative to help accurately depict the formation of coherent eddies in the inertial range as well as their influence on the modified energy transfers that result from the nonlinear interaction between coherent and chaotic structures. This results in a modification of the constants and the damping functions as shown in Jin and Braza, 1994, Hoarau, 2002 and used by Rodes, 1999. These modifications account for a lower gradient in the damping law, modifying f_μ. This modification plays an important role in the alteration of the flow physics near the wall because it affects the turbulent viscosity ν_t. By decreasing the gradient of the damping function, the dissipation of the turbulent viscosity is lessened close to the wall in conditions of high shear stress and intense adverse pressure gradients which are encountered in non-equilibrium turbulence. The damping functions are summarized in Hoarau, 2016 and in Hoarau et al., 2016.

- **Damping functions:**
  $f_\mu = 1 - exp(-0.0002\ y^+ - 0.000065\ {y^+}^2)$
  $f_1 = 1$
  $f_2 = [1 - 0.22\ exp(-\frac{Re_t^2}{36})]$

- **Constants of the model**
  $C_\mu = 0.02$

$C_{\varepsilon_1} = 1.44$
$C_{\varepsilon_2} = 1.92$
$\sigma_k = 1.0$
$\sigma_\varepsilon = 1.3$

- **Boundary conditions at the wall:**
  $k = 0 \quad$ and $\quad \varepsilon = 0$

References

Chien, Kuei-Yuan (May 1982). "Predictions of Channel and Boundary-Layer Flows with a Low-Reynolds-Number Turbulence Model". In: *https://doi.org/10.2514/3.51043* 20 (1), pp. 33–38. DOI: 10.2514/3.51043.

Hoarau, Y. (2016). *Turbulence Models Description*.

Hoarau, Yannick (Jan. 2002). "Analyse physique par simulation numérique et modélisation des écoulements décollés instationnaires autour de surfaces portantes". In: *http://www.theses.fr*.

Hoarau, Yannick et al. (2016). "Recent Developments of the Navier Stokes Multi Block (NSMB) CFD solver". In: *54th AIAA Aerospace Sciences Meeting*. AIAA SciTech Forum. American Institute of Aeronautics and Astronautics. DOI: doi:10.2514/6.2016-2056.

Jin, G and M Braza (1994). "Two-equation turbulence model for unsteady separated flows around airfoils". In: *AIAA Journal* 32.11, pp. 2316–2320. ISSN: 0001-1452. DOI: 10.2514/3.12292.

Jones, W.P. and B.E. Launder (1972). "The Prediction of Laminarization with a Two-Equation Model of Turbulence." In: *Int. J. of Heat and Mass Transfer* vol. 15, p. 301.

Kunz, R.F. and B. Lakshminarayana (1992). "Stability of explicit Navier-Stokes Procedures using k-epsilon algebraic Reynolds Stress Turbulence Models". In: *J. of Computational Physics* 103, pp. 141–159.

Nishizawa, S et al. (2015). "Influence of grid aspect ratio on planetary boundary layer turbulence in large-eddy simulations". In: *Geosci. Model Dev* 8, pp. 3393–3419. DOI: 10.5194/gmd-8-3393-2015.

Rodes, Pascal (Jan. 1999). "Contribution à l'étude d'écoulements instationnaires transtionnels et turbulents autour d'une aile par simulation numérique et modélisation". In: *http://www.theses.fr*.

Spalart, P. R. et al. (1997). "Comments on the feasibility of LES for wings and on a hybrid RANS/LES approach". In: *Advances in DNS/LES* 1.JANUARY, pp. 4–8.

Speziale, Charles G. (Sept. 1998). "A Combined Large-Eddy Simulation and Time-Dependent RANS Capability for High-Speed Compressible Flows". In: *Journal of Scientific Computing 1998 13:3* 13 (3), pp. 253–274. ISSN: 1573-7691. DOI: 10.1023/A:1023266932231.

Vos, J. B. et al. (1998). "Recent advances in aerodynamics inside the nsmb (navier stokes multi block) consortium". In: *36th AIAA Aerospace Sci-*

ences Meeting and Exhibit. DOI: 10.2514/6.1998-225. URL: https://arc.aiaa.org/doi/abs/10.2514/6.1998-225.

Chapter 5

The Organized Eddy Simulation (OES) turbulence modelling approach

5.1 Foundations of the Organized Eddy Simulation method

In high Reynolds flows, both chaotic turbulence – characterized by random and short-lived vortex-like structures – and coherent eddies coexist. The latter are caused by the creation and growth of flow instabilities in regions of non-equilibrium where the creation of turbulent energy exceeds dissipative effects that tend to convert the energy of these eddies into internal energy via mesoscopic processes (molecular viscosity).

In a region of non-equilibrium, it would hence be possible to notice a stark difference between the slope of the spectrum compared to the one for homogeneous turbulence where a balance is assumed between creation processes and dissipative phenomenons, and the turbulence spectrum for a situation of non-equilibrium, as shown by Braza et al., 2006 via Particle Image Velocimetry (PIV) measurements.

Studies lead by Cantwell and Coles, 1983 and Brown and Roshko, 1974 were early attempts to to experimentally identify the development of these coherent structures forming in the wake and around bluff bodies in high

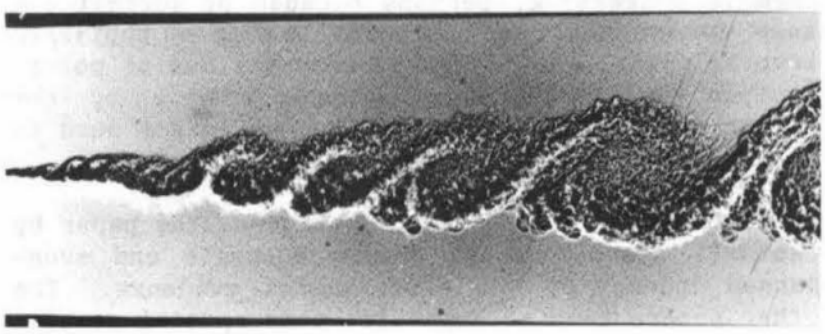

Figure 5.1: A picture from Brown and Roshko, 1974 showing the destabilisation of a shear layer which forms the Kelvin-Helmholtz coherent vortices. As the coherent eddies grow more and more, the intensification of the shear stress contributes to the production of turbulence, giving rise to the formation of a multitude of smaller eddies of varying degrees of spatio-temporal coherence.

Reynolds number, and most importantly to attempt to define the notion of coherent eddies.

However, Corrsin, 1943 was the first to argue that the idea of turbulence as exclusively composed of chaotic structures needed to be overhauled due to his observation of boundary intermittency at the turbulent-non turbulent interface of a free jet. This demonstrated the existence of a large-scale disturbance amidst the turmoil of turbulence. Following this examination, Townsend, 1956 produced a new model that presents turbulence as a phenomenon that involves the co-existence of two types of structures: chaotic eddies and coherent structures. The first constitute the fuzzy background of turbulence and correspond to the diffusive dynamics described in Kolmogorov, 1991 or Frisch and Kolmogorov, 1995, which define isotropic and homogeneous turbulence. The bigger, coherent eddies thus play an advective role, contributing to the large-scale transport of turbulence and the formation of immediately smaller scales that feed even smaller eddies through non-linear phenomena, transferring their kinetic energy in a cascade-like fashion.

In order to accurately and effectively represent this transfer of energy in numerical simulations, the Reynolds stress tensor that arises from the Reynolds-averaged (or ensemble-averaged) Navier-Stokes (RANS-like) equa-

tions needs to be modelled properly. In the most commonly used turbulence models applied to RANS calculations, it is generally assumed that the Reynolds tensor takes the shape of mean-field gradient tensor according to the Boussinesq approximation that finds its rationale in the dissipative nature of turbulence. It is thus suggested that turbulence acts as a second viscosity term, playing a role similar to molecular viscosity in that it allows to transfer momentum and eventually smooth out gradients that may appear in the flow, albeit this time through non-linear advection.

However, this hypothesis does not necessarily hold true in regions of the flow where turbulence is developing and where equilibrium between turbulent production and dissipation is not respected. It has been showed by Bourguet et al., 2008 and Braza et al., 2006 that non-linear dynamics govern the behavior of eddies in the inertial zone, highlighting an interaction between coherent structures that develop in the flow and the chaotic background of turbulence that they feed.

It was shown by Djeridi et al., 2003 and Braza et al., 2006 through Laser Doppler Velocimetry (LDV) in the first study and by using a Time-Resolved PIV (TRPIV) visualization technique in the second that the existence and development of coherent eddies profoundly impacts the nature of the chaotic content of turbulence: In the intertial range, the slope of the turbulence energy spectrum differs from that of isotropic turbulence which is shown to be equal to $-5/3$ by Kolmogorov, 1991. This is best illustrated when the coherent content of the spectrum has been filtered out through the use of a phase average properly tuned to extract the quasi-periodic signature of the coherent eddies.

Hence, it was observed that the phase-average could be applied to the Navier-Stokes equations to reach a new formulation. While an ensemble-averaged formulation yielded the RANS equations where the content of turbulence is either calculated or modelled on the basis of a limiting length scale, phase-averaged Navier-Stokes equations distinguish the phase-averaged content – which is comprised of coherent eddies – from purely random eddies which are modelled. Consequently, any state variable $u(x,t)$ can be decomposed like such:

$$u(x,t) = \langle u(x,t) \rangle + u'(x,t) = \bar{u}(x) + u_c(x,t) + u'(x,t) \tag{5.1}$$

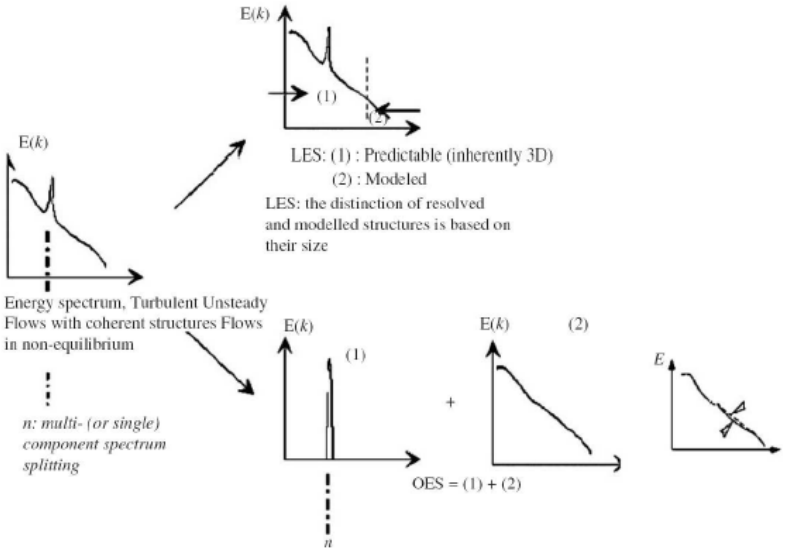

Figure 5.2: Schematic representation of the spectral decomposition chosen in the Organized Eddy Simulation method. The organized – or coherent – content is characterized by the presence of peaks in the spectrum due to their statistically coherent nature

where $\langle u(x,t)\rangle = \bar{u}(x) + u_c(x,t)$ is the phase-averaged variable, $\bar{u}(x)$ is the ensemble average (which is also the time average of the field in the ergodic hypothesis) and $u_c(x,t)$ is made of all resolved coherent flow fluctuations.

It can be concluded that the development and growth of coherent structures causes a deep modification in the properties of turbulence, which were modelled by Hoarau, 2002 in his thesis in the context of strongly separated flows around airfoils.

In the same study, it has been found that the term $-\overline{u'v'}/\kappa$ is non-constant and its value increases near the walls where a conjunction of both intense adverse pressure gradients and shear stress contribute to its augmentation. While its value has been found to be nearly constant and equal to 0.3 in most of a fully-turbulent boundary layer by Bradshaw, 1967, this does not hold true in highly separated shear flows that develop around curved bodies. This value needs to be corrected so as to not over-predict the turbulent eddy viscosity and allow coherent eddies to develop in the flow.

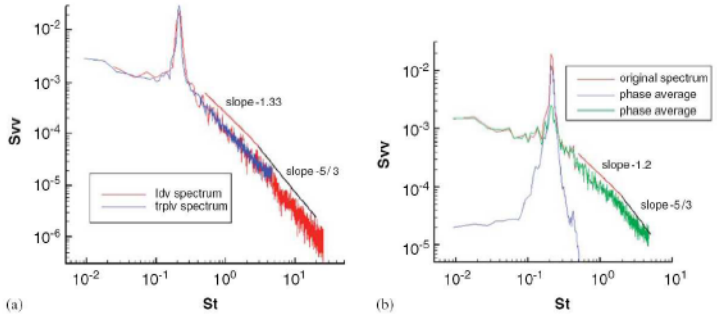

Figure 5.3: These measures were obtained in the wake of a circular cylinder at a Reynolds number of 1.4×10^5 (a) A comparison of the turbulent kinetic energy spectra obtained from LDV (red) and PIV (blue) data. Both show that the slope of the inertial range is less steep in the vicinity of the coherent peak, denoting the imbalance between turbulence production and dissipation (skewed towards production). (b) A sililar graph is produced from PIV data before and after a phase average is applied to the data. In the phase average, here drawn in green, one can notice that the value of the slope is also less pronounced compared to Kolmogorov's $-5/3$ constant.

References

Bourguet, R. et al. (2008). "Anisotropic Organised Eddy Simulation for the prediction of non-equilibrium turbulent flows around bodies". In: *Journal of Fluids and Structures* 24.8, pp. 1240–1251. ISSN: 08899746. DOI: 10.1016/j.jfluidstructs.2008.07.004.

Bradshaw, P. (Sept. 1967). "The turbulence structure of equilibrium boundary layers". In: *Journal of Fluid Mechanics* 29 (4), pp. 625–645. ISSN: 1469-7645. DOI: 10.1017/S0022112067001089.

Braza, M et al. (2006). "Turbulence modelling improvement for highly detached unsteady aerodynamic flows by statistical and hybrid approaches". In: *ECCOMAS CFD 2006 : European Conference on Computational Fluid Dynamics, September 5-8, 2006* September.

Brown, Garry L. and Anatol Roshko (1974). "On density effects and large structure in turbulent mixing layers". In: *Journal of Fluid Mechanics* 64 (4), pp. 775–816. ISSN: 1469-7645. DOI: 10.1017/S002211207400190X.

Cantwell, Brian and Donald Coles (1983). "An experimental study of entrainment and transport in the turbulent near wake of a circular cylinder".

In: *Journal of Fluid Mechanics* 136, pp. 321–374. ISSN: 14697645. DOI: 10.1017/S0022112083002189.

Corrsin, S. (1943). "Investigation of Flow in an Axially Symmetrical Heated Jet of Air". In: *undefined*.

Djeridi, H. et al. (2003). "Near-Wake Turbulence Properties around a Circular Cylinder at High Reynolds Number". In: *Flow, Turbulence and Combustion* 71 (1-4), pp. 19–34. DOI: 10.1023/B:APPL.0000014930.49408.53.

Frisch, U. (Uriel) and A. N. (Andrei Nikolaevich) Kolmogorov (1995). "Turbulence : the legacy of A.N. Kolmogorov". In: p. 296.

Hoarau, Yannick (Jan. 2002). "Analyse physique par simulation numérique et modélisation des écoulements décollés instationnaires autour de surfaces portantes". In: *http://www.theses.fr*.

Kolmogorov, A. N. (July 1991). "The local structure of turbulence in incompressible viscous fluid for very large Reynolds numbers". In: *Proceedings of the Royal Society of London. Series A: Mathematical and Physical Sciences* 434 (1890), pp. 9–13. DOI: 10.1098/RSPA.1991.0075.

Townsend, A. A. (Dec. 1956). "The properties of equilibrium boundary layers". In: *Journal of Fluid Mechanics* 1 (06), p. 561. DOI: 10.1017/S0022112056000378.

Chapter 6

Description of the numerical methodology and phenomenology

6.1 Description of the computations

6.1.1 Geometry and mesh used

For this study, two-dimensional computations were performed around an A320 profile of chord $c = 0.15$ cm in accordance with the chord of the transonic Reduced Scale prototype (tRS) of the SMS project. A C-H topology computational domain was set-up around the profile to ensure that the underlying mesh would have strong orthogonality features and an overall good quality.

In order to ensure that the boundary layer is well computed, the mesh is refined near the geometry walls so as to place the first cell within a distance of $y^+ = 1$ above the wall in order to ensure proper convergence requirements concerning turbulence damping laws near solid walls.

The first cell is located in the approximate range $y^+ = 0.1$ to $y^+ = 0.5$. The number of refinement layers around the geometry was suitably chosen to address the need for a proper computation of transverse gradients. Additionally, the geometry is adequately refined in the streamwise direction over the suction side and in the wake to capture both the shock as well as the formation and transport of coherent eddies.

Morphing is performed numerically thanks to the Arbitrary Lagrangian-

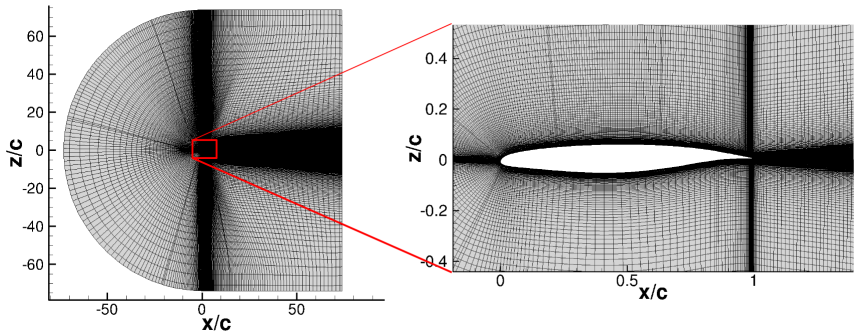

Figure 6.1: Computational domain and structured mesh used for 2D computations.

Eulerian methodology used for the deformed grid. A second-order polynomial deformation of the trailing edge is imposed so that it moves up and down about its initial position by plus or minus 1°.

6.1.2 Physical parameters

Numerical simulations were performed at the same inlet conditions as the experiments with the tRS prototype of the SMS project constructed by the INPT/LAPLACE Laboratory and made available in IMP-PAN, together with its specific piezoactuation power supply for the experiments to be carried out in the transonic wind tunnel of Gdańsk. An inlet Mach number of 0.78 and an angle of incidence of $\alpha = 1.8$ř were chosen to make sure that freestream conditions are representative of real flight freestream conditions for an A320 airliner. Free stream total pressure is set to 101 kPa while total temperature is 293 K, and turbulence level is chosen at 0.5%. A viscosity ratio of 10 is set. With all these parameters, the chord Reynolds number for this case is 2.06×10^6.

6.1.3 Numerical parameters and computational setup

Computations are carried out with the Navier-Stokes Multi Block (NSMB) code that is the result of a collaboration between CFS Engineering, IMFT and other institutes within the NSMB European Consortium. The computational mesh described earlier is a structured mesh that is divided into multiple blocks that contain approximately the same number of cells each, in order to

exploit the parallelization capability of the multi-block solver. This allows the workload to be evenly distributed along the cores of a computational node and considerably speed up simulation time. Following a speed-up analysis, the two-dimensional mesh is cut in 64 blocks that are optimally spread across the 36 cores of a single computation node on the Olympe supercomputer of the CALMIP ("Calcul en Midi-Pyrénées" Supercomputing Center) by means of a load balancing algorithm.

The computational domain is extended by about 60 to 70 chords around the geometry which prevents boundary effects and numerical instabilities from impacting wake development. Likewise, slip boundary conditions are applied at the upper and lower boundaries of the computational domain after numerical computations have indicated that choosing a slip boundary condition (non-zero velocity tangent to the surface) provides a better agreement with experimental results.

The temporal and spatial discretization schemes are chosen to be similar to the previous studies conducted by Grossi, Braza, and Hoarau, 2014 as well as Szubert et al., 2015 or Szubert et al., 2016: A third-order upwind Roe scheme with Van Leer's MUSCL limiter (Leer, 1979) is employed for the discretization of the advection terms thanks to its accuracy in capturing discontinuities and convergence properties while time integration is performed via a dual-time stepping, second-order backward difference scheme with a sufficient number of inner iterations to ensure proper convergence. With this particular mesh, time step convergence was achieved for a constant time step of less than 5×10^{-6} seconds while about 150 inner iterations are carried out for every time step.

The Organised Eddy Simulation method (OES) has been employed by our group in multiple studies of our group involving the capture of coherent eddies. Therefore, the present computations solve the k-epsilon turbulent transport equations under a k-epsilon-OES formulation with a modification of closure coefficients, boundary conditions and damping functions in accordance to this statistical modelling.

6.2 Results

6.2.1 Phenomenology of the 3D flow

Delayed Detached Eddy Simulations with an OES implementation for the near-wall region (DDES-OES) were produced around the A320 wing at a high Reynolds number of 2.2×10^6 and at a Mach number of 0.78.

In order to reach proper convergence of the L_2-norm of the net flux residual, the time step needs to be reduced to $\Delta t = 2.5 \times 10^{-6}$ s.

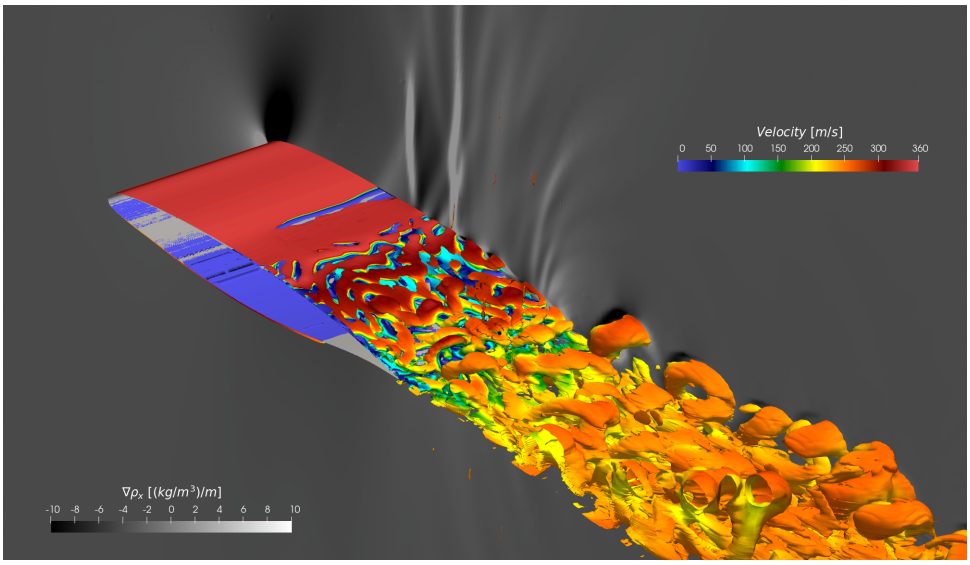

Figure 6.2: Numerical Schlieren consisting of iso-contours of the longitudinal component of the density gradient field (in shades of grey) with a Q-criterion iso-surface colored with the velocity magnitude.

Coherent eddies, which form as a consequence of intense shearing and adverse pressure gradients, are highlighted by the bulging Q-criterion iso-surfaces in the wake and in the shear layer that forms on top of the wing.

The gradient of density iso-contours (in grey) shows the presence of shocklets, the lambda-shock structure and acoustic waves arising from so-called vortical modes. A buffet period can be evidenced in the time history of the forces and occurs at a frequency that lies in the vicinity of 100 Hz. It is shown in 2D OES simulations that the natural frequency of buffet in the same flow regime is equal to 110 Hz.

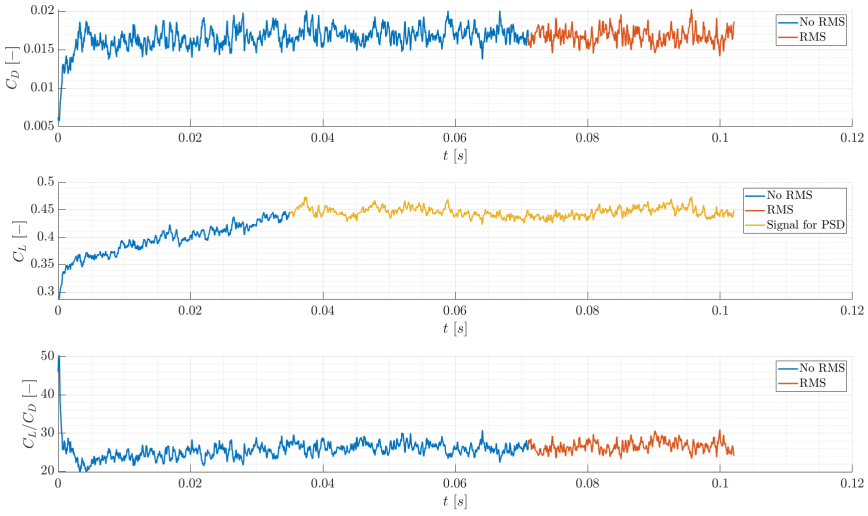

Figure 6.3: The drag, lift and lift-to-drag time series over the duration of a DDES-OES run lasting approximately 0.1 s. The force oscillations take place at a frequency neighboring 90 to approximately 100 Hz.

References

Grossi, Fernando, Marianna Braza, and Yannick Hoarau (2014). "Prediction of Transonic Buffet by Delayed Detached-Eddy Simulation". In: *AIAA Journal* 52.10, pp. 2300–2312. ISSN: 0001-1452. DOI: 10.2514/1.J052873.

Leer, Bram van (1979). "Towards the ultimate conservative difference scheme. V. A second-order sequel to Godunov's method". In: *Journal of Computational Physics* 32 (1), pp. 101–136. ISSN: 10902716. DOI: 10.1016/0021-9991(79)90145-1. URL: https://www.researchgate.net/publication/285599602_Towards_the_Ultimate_Conservative_Difference_Scheme_V_A_Second-order_Sequel_to_Godunov's_Method.

Szubert, Damien et al. (2015). "Shock-vortex shear-layer interaction in the transonic flow around a supercritical airfoil at high Reynolds number in buffet conditions". In: *Journal of Fluids and Structures* 55, pp. 276–302. ISSN: 10958622. DOI: 10.1016/j.jfluidstructs.2015.03.005.

Szubert, Damien et al. (2016). "Numerical study of the turbulent transonic interaction and transition location effect involving optimisation around a

supercritical aerofoil". In: *European Journal of Mechanics, B/Fluids* 55, pp. 380–393. ISSN: 09977546. DOI: 10.1016/j.euromechflu.2015.09.007.

Effects of vibrating and deformed trailing edge of a morphing supercritical airfoil in transonic regime by numerical simulation at high Reynolds number

In the following, a first article published in the Journal of Fluids and Structures gathers the first conclusions of the thesis. It highlights the phenomena that motivate trailing edge morphing while establishing the existence of a feedback effect which draws information from the wake towards the shock and even brings it slightly upstream of the lambda shock system as evidenced by numerical Schlieren visualization associated to streaklines.

A synchronization between the actuation frequency of the trailing edge and the buffet frequency is also evidenced for actuation frequencies neighboring the natural buffet frequency in this flow regime. Different morphing deformation modes are also studied and their effect on aerodynamic performance is quantified.

ARTICLE IN PRESS

Journal of Fluids and Structures xxx (xxxx) xxx

Contents lists available at ScienceDirect

Journal of Fluids and Structures

journal homepage: www.elsevier.com/locate/jfs

Effects of vibrating and deformed trailing edge of a morphing supercritical airfoil in transonic regime by numerical simulation at high Reynolds number

J.-B. Tô [a,*,1], N. Simiriotis [a,1], A. Marouf [a,b,1], D. Szubert [a,2], I. Asproulias [a,2], D.M. Zilli [a,3], Y. Hoarau [b,4], J.C.R. Hunt [c,a,5], M. Braza [a,*,6]

[a] *Institut de Mécanique des Fluides de Toulouse (IMFT), UMR 5502 CNRS-INPT-UT3, Allée du prof. Camille Soula, 31400 Toulouse, France*

[b] *ICUBE, Unité Mixte C.N.R.S.-Université de Strasbourg 7357, France*

[c] *University College London, United Kingdom*

ARTICLE INFO

Article history:
Received 11 January 2019
Received in revised form 6 February 2019
Accepted 11 February 2019
Available online xxxx

Keywords:
Morphing
Transonic buffet
Turbulence
Organised eddy simulation OES
Von Kármán vortices
Shear layer

ABSTRACT

This article examines the aerodynamic performance increase of an Airbus A320 aerofoil thanks to morphing of the near-trailing-edge region in transonic regime corresponding to cruise conditions. The study has been carried out by numerical simulation at Reynolds number $Re = 2.06 \times 10^6$ and Mach number of 0.78, by using the NSMB code (Navier–Stokes MultiBlock) including adapted turbulence modelling approaches sensitised in capturing coherent structures development. It has been shown that transonic buffet occurs at angle of incidence 1.8° and in a more pronounced way at angle of 5°. The interactions among the shock-boundary layer area, the shear layers vortices and those of the near wake have been analysed by spectral analysis and streakline dynamics. Strong feedback effects have been shown from the near trailing-edge region towards the SWBLI (Shock Wave Boundary Layer Interaction) up to the upstream of the shock area. By taking benefit from these feedback effects, it has been obtained that morphing applied as a slight upwards deflection of the near-trailing-edge region by 2° is able to practically attenuate the buffet instability and to increase lift-to-drag ratio by 10.4 percent. The trailing-edge's area vibration at low amplitudes simulating the motion of piezo-patches of MFC type (Macro-Fibre Composites) applied experimentally in the context of the H2020 European research project www.smartwing.org/SMS/EU) has shown a lock-in effect of the buffet's frequency. Therefore, a conditioning of the shock's motion by means of these actuations can be reached, although a relative increase of the *rms* of the aerodynamic forces is produced in this case. The study of a combined upwards slight

* Corresponding authors.
E-mail addresses: jean-baptiste.to@imft.fr (J.-B. Tô), nikolaos.simiriotis@imft.fr (N. Simiriotis), abderahmane.marouf@imft.fr (A. Marouf), damien.szubert@imft.fr (D. Szubert), ioannis.asproulias@imft.fr (I. Asproulias), dmzilli@epsilon-alcen.com (D.M. Zilli), hoarau@unistra.fr (Y. Hoarau), julian.hunt@ucl.ac.uk (J.C.R. Hunt), marianna.braza@imft.fr (M. Braza).

1 Ph.D. fellow.
2 Postdoctoral research fellow.
3 Graduate student.
4 Professor.
5 Professor Em.
6 Director of Research CNRS.

https://doi.org/10.1016/j.jfluidstructs.2019.02.011

Please cite this article as: J.-B. Tô, N. Simiriotis, A. Marouf et al., Effects of vibrating and deformed trailing edge of a morphing supercritical airfoil in transonic regime by numerical simulation at high Reynolds number. Journal of Fluids and Structures (2019), https://doi.org/10.1016/j.jfluidstructs.2019.02.011.

deflection and of trailing-edge area vibrations allowed obtaining decrease of drag and increase of lift-to-drag ratio with simultaneous decrease of *rms*. These effects have been studied for a wide frequency range from 200 to 500 Hz.

1. Introduction

A considerable number of experimental and numerical studies have been devoted to the investigation of the transonic interaction around a wing and particularly on buffet appearance, i.e the unsteady quasi-periodic shock's motion over a wing, occurring in a specific Mach number range of (0.7–0.8) (McDevitt et al., 1976). This range corresponds to cruise conditions for which it is crucial to analyse the buffet dynamics in order to attenuate or suppress it, because it could create critical conditions for dip-flutter instability amplification with negative damping. The transonic buffet is a result of a fluid's instability, due to a strong interaction among the shock, the boundary layer and the separated shear layers as well as the coherent vortices formed downstream of the trailing edge, whose dynamics influence each other in a closed loop. Pioneering experimental studies driven by Seegmiller et al. (1978), McDevitt et al. (1976), Levy (1978), Marvin et al. (1980) and more recently by Jacquin et al. (2005, 2009) who investigated the SWBLI associated with the buffet dynamics and its effects on the wall pressure and the aerodynamic forces including PIV measurements. Collected experimental studies of the transonic buffet can be also found (Doerffer et al., 2011) in the context of the European research programme UFAST (Unsteady Effects in Shock Wave Induced Separation) and of the European research programme TFAST (Transition Location Effect on Shock Wave Boundary Layer Interaction) http://tfast.eu (Doerffer et al., 2019).

In the last twenty five years, in parallel with experimental investigations, numerical studies examined the transonic interaction and the buffet phenomenon. Starting from the low Reynolds number range, the successive stages of instabilities amplification as Mach number increases had been studied through DNS and 2D numerical simulation by Bouhadji and Braza (1998). It was shown that first, a von Kármán instability mode is amplified in the wake and makes undulation of the two separated shear layers over a NACA0012 airfoil at Reynolds number of 10,000. As Mach number increases from 0.5 to 0.6, a progressive formation of a slightly supersonic region upstream of the shock is formed and remains steady, while the von Kármán amplitude progressively increases. At Mach number of 0.7, a much lower-frequency mode appears in the forces fluctuations, that envelopes a considerable number of periods of the von Kármán mode, while the upstream of the shock supersonic area starts oscillating according to this low frequency and gives birth to the buffet mode. These lower Reynolds number studies allowed precisely the follow-up of the above successive stages and made evidence of the history in the appearance of the different instability modes, a fact that is difficult to observe experimentally, because the amplification of these modes in the high Reynolds number range occurs quite fast.

As Mach number increases in the range (0.7–0.8), the buffet amplitudes increase and continue enveloping the von Kármán mode periods, while the averaged shock position progressively moves downstream. As Mach number increases up to 0.85, only the von Kármán mode persists up to Mach numbers 0.9 in the forces fluctuations, while the wall pressure is practically steady. This is due to the shock wave occurrence in most downstream positions because of the progressive increase of the hyperbolic character of the flow with the Mach number increase. At Mach numbers in the range (0.9–0.95) the shock wave has moved in the wake and the forces are steady.

Considering 3D studies, Bourdet et al. (2003) studied the buffet instability amplification by DNS and by means of the Landau global oscillator model around a NACA0012 airfoil. The DNS study illustrated the secondary instability amplification and the formation of spanwise undulated vortex structures in the near wake, governed by predominant large-scale wave lengths. This pattern persists in the high Reynolds number range concerning the three-dimensional character of the coherent structures past the trailing edge, as shown by Delayed Detached Eddy Simulation in Grossi et al. (2014) around a supercritical wing, the OAT15A a Mach numbers corresponding to the buffet occurrence and Reynolds numbers of order 3 Million, studied in the context of the European research programme ATAAC.[7] In these studies, the shock wave structure and the buffet dynamics were found not considerably affected by the three-dimensionality. For these reasons, as mentioned below, a two-dimensional approach can be used in order to ensure a rich parametric study concerning the morphing effects. Moreover, the Zonal Detached Eddy Simulations, ZDES by Deck (2005) presents a quite complete analysis of the transonic interaction around the OAT15A and a promising turbulence modelling approach.

Moreover, 2D URANS studies at high Reynolds numbers (Brunet, 2003) have also provided a detailed physical analysis of the buffet around the same configuration. More recently, Szubert et al. (2015b) studied the transonic interaction among the buffet, the shear layer vortices and the von Kármán vortices by 2D numerical simulation using the Organised Eddy Simulation, OES (Braza et al., 2006 and Bourguet et al., 2008). Through this method, able to capture the instabilities amplification and the coherent structure dynamics in 2D and 3D, the transonic interaction was studied as well as its impact on the pressure and forces fluctuations, by means of wavelets and Proper Orthogonal Decomposition (POD). The

[7] http://cfd.mace.manchester.ac.uk/twiki/bin/view/ATAAC/WebHome.

Please cite this article as: J.-B. Tô, N. Simiriotis, A. Marouf et al., Effects of vibrating and deformed trailing edge of a morphing supercritical airfoil in transonic regime by numerical simulation at high Reynolds number. Journal of Fluids and Structures (2019), https://doi.org/10.1016/j.jfluidstructs.2019.02.011.

role of the higher-order modes in producing a shear sheltering effect in the separated shear layers past the SWBLI was analysed and used to create a stochastic forcing by re-injection of turbulence in these layers and in the shock's shearing region, as source terms in the turbulence transport equations, in the so-called IOES (Improved OES) approach. This forcing acts as an eddy-blocking effect as described in Hunt et al. (2008) resulting in a considerable thinning of the shear layers and of the wake's width. This effect, besides a significant improvement of the pressure coefficient and the forces evaluation, is used in the present study in order to enhance the benefits from the morphing as described in the results discussion.

Moreover, the transition location effects on the buffet have been studied and optimised in the same high Reynolds number range for the supercritical wing V2C design by Dassault Aviation in the context of the TFAST European project. Szubert et al. (2015a) studied by DDES/OES the transonic buffet and carried out an optimisation of the transition location. The study by Bonne (2018) proposed quite successful physical models of the laminar SWBLI that allowed analysis of the multi-modal coupling in the high Reynolds number range, offering physical mechanisms comprehension of high interest for the industrial applications, including buffet study in swept wings by numerical simulation.

The objective of the present article is to study the effects of morphing on the flow dynamics regarding an unconfined 2D configuration to help the design the A320 morphing prototype in the context of the H2020 European research project SMS.[8] This study will serve to implement the best type of actuations near the trailing edge of the experimental prototype, in order to obtain optimal increase of the aerodynamic performance. To this end, the actuations studied in the present paper by means of numerical simulation are in accordance with the hardware actuations studied in a number of experimental works of the present research group in the context of the SMS research platform, supported by the French Foundation "Sciences et Technologies pour l'Aéronautique et l'Espace" - (STAE), http://www.fondation-stae.net/ and in other recent studies as follows.

It has been shown (Scheller, 2015 and Scheller et al., 2015) that vortex breakdown occurs by trailing edge vibrations using PUSH–PUSH piezoactuators in the trailing-edge region of a NACA0012 wing, with a significant lift improvement, drag and noise sources decrease, in the context of the STAE Research projects research project EMMAV — Electroactive Morphing for Micro-Airvehicles using Shape Memory Alloys (SMA) (Chinaud et al., 2014) and DYNAMORPH: "Dynamic Regime Electroactive Morphing", by means of a combined action of SMA and piezoactuators (Scheller, 2015). Furthermore, the European research programme SARISTU[9] had considered morphing trailing edge devices through SMA and MEMS. The European programme SADE[10] developed morphing devices for the leading edge and the wings by using flexible matrix composites (FMC). In particular, the MFC piezoactuators provided good performances in subsonic flow conditions (Scheller, 2015 and Jodin et al., 2017). The actuation concept associating different degrees of deformation and vibration at multiple time scales is called hybrid electro-active morphing in these studies by the multidisciplinary research group IMFT-LAPLACE. It was demonstrated that the flow dynamics are significantly affected by the trailing edge actuation. An important reduction of the wake's width and spectral energy associated to drag and aerodynamic noise respectively was quantified by means of Particle Image Velocimetry (PIV) measurements. In the context of these studies, the aim of the hybrid morphing concept is to use the turbulence itself, in order to manipulate part of the "harmful" eddies and to enhance the beneficial ones thanks to the "eddy blocking effect" (Hunt et al., 2008) previously mentioned. The objective is to increase the aerodynamic performances and simultaneously decrease the noise sources generated from predominant instability modes. Hence at a given controlled camber, the vibrating trailing edge adds kinetic energy in the wake that fosters the suppression of coherent turbulent structures. This kind of actuation is precisely studied numerically in the present article, together with a slight upwards deflection. It is worthwhile mentioning that in transonic speeds, only slight deformations of the rear region are recommended, whereas in low subsonic speeds, large deformations are needed. Therefore the present article will examine the effects of slightly deformed and vibrating trailing-edge region in a wide frequency range, first as a stand-alone actuation and secondly combined with a slight static deflection of the rear part, which was proven beneficial in recent studies of us (Zilli, 2015).

There do not exist, to our knowledge, studies concerning morphing in transonic regimes where the target is to increase lift-to-drag ratio and to decrease drag and acoustic generation. The numerical study by Barbut et al. (2010) by means of DDES (Delayed Detached Eddy Simulation) investigated the dynamics around a NACA0012 wing with an oscillating trailing edge in the transonic regime. An experimental and numerical study around this wing can be found in a work by Braza et al. (2011).

Therefore, the objectives of this paper are to examine the effects of morphing of the rear part of the wing by suitable deformations and vibrations able to manipulate the surrounding turbulence and vortex dynamics and able to be realised in experimental environment and in real flight. This paper is thus articulated as follows: In the first section, the numerical parameters and turbulence modelling are introduced. Secondly, the results are presented investigating the effects of morphing on the aerodynamic performance of the wing by different trailing-edge vibrations, by a slight deformation upwards and by combining both actuations. The results are discussed regarding optimal behaviours in respect of aerodynamic performance and finally the conclusions are drawn in the last part of the article.

8 www.smartwing.org/SMS/EU.

9 http://www.saristu.eu.

10 https://cordis.europa.eu/project/rcn/89908/reporting/en.

Please cite this article as: J.-B. Tô, N. Simiriotis, A. Marouf et al., Effects of vibrating and deformed trailing edge of a morphing supercritical airfoil in transonic regime by numerical simulation at high Reynolds number. Journal of Fluids and Structures (2019), https://doi.org/10.1016/j.jfluidstructs.2019.02.011.

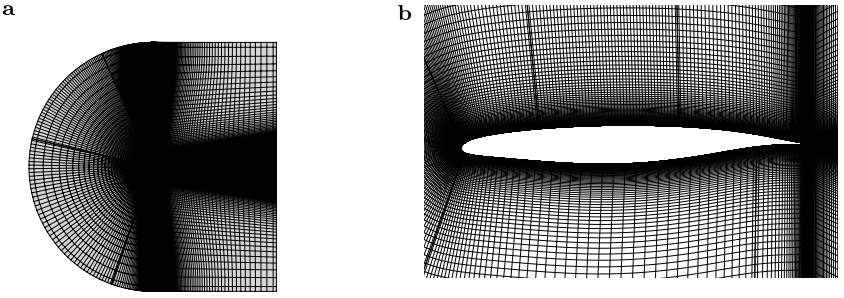

Fig. 1. (a) Computational grid over the A320 airfoil and (b) zoom around the wall area.

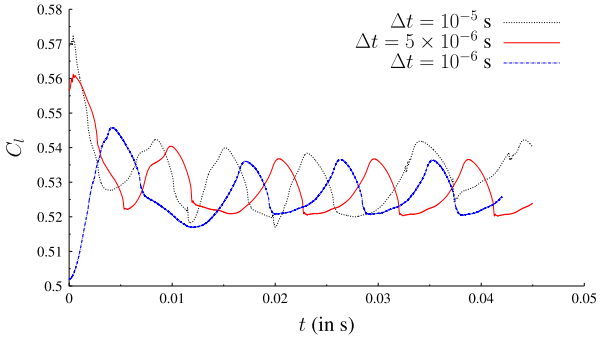

Fig. 2. Time series of the C_l coefficient for different time steps. For $\Delta t \leq 5 \times 10^{-6}$, convergence is reached.

2. Flow regime, numerical parameters and turbulence modelling

The configuration investigated is a supercritical AIRBUS A320 wing the rear part of which is deformable and vibrating according to specific frequencies dictated by the electroactive morphing studies carried out in the SMS European project for the cruise speed design. The free-stream Mach number is 0.78 and the chord-based Reynolds number is 2.06×10^6. The chord length is 0.15 m with respect to the experimental mock-up designed for the wind tunnel of the IMP-PAN Academy of Science in Gdansk (Flaszynski et al., 2018), Poland within the partnership of this European project. Two angles of incidence are investigated: $\alpha = 1.8°$ and $\alpha = 5°$. The first angle is a standard cruise speed angle. The second can also occur in cruise depending on the wind direction but it lasts shorter than the nominal cruise angle of 1.8°. Furthermore, this angle of 5° has been chosen because it enhances boundary layer separation and the transverse velocity gradients across the separated shear layers. Therefore, this angle allows a more pronounced interaction between the separated region and the shock, thus offering a comprehensive analysis of the mechanisms.

The morphing strategies investigated in the present study have the objective to accompany the prototype's design. The trailing edge region can be slightly deformed and vibrate thanks to piezoactuators at frequencies of a few hundred Hz up to an order of thousand Hz. This kind of piezoactuators have been studied for subsonic speed regimes by Jodin et al. (2017) and can be adapted in the present transonic speeds according to the present numerical simulations.

This 2D transonic flow simulation around an A320 airfoil is realised by using the Navier–Stokes Multi Block (NSMB) code (Hoarau et al., 2016), solving the complete system of the Navier–Stokes equations with advanced turbulence models in finite-volume formulation. Based on previous detailed studies of our research group by Grossi et al. (2014) and Szubert et al. (2015b), spatial fluxes are discretised using a 3rd order Roe scheme with MUSCL Van Leer limiter, while a 2nd order backward dual-time stepping scheme is chosen for time integration.

A two-dimensional multi-block structured grid has been used for the computations (Fig. 1). Two different grids have been examined and an exhaustive study of the grid influence, and time step has been carried out. Initially, a coarser grid of 160000 computational cells had been compared with a finer grid containing 190000-elements, both of C–H topology. This grid has been finally used for all the computations. The computational domain and geometry are deformed by using the Arbitrary Lagrangian–Eulerian (ALE) method to represent a dynamic deformation and motion of the trailing edge during morphing.

For this fine grid, a detailed sensitivity study in respect of the time step has been carried out. The results concerning the lift coefficient are presented in Fig. 2. It is shown that $\Delta t = 5 \times 10^{-6}$ s and $\Delta t = 10^{-6}$ s give practically similar results, therefore the value of $\Delta t = 5 \times 10^{-6}$ s has been finally chosen in order to obtain accurate results with a reasonable CPU time.

Please cite this article as: J.-B. Tô, N. Simiriotis, A. Marouf et al., Effects of vibrating and deformed trailing edge of a morphing supercritical airfoil in transonic regime by numerical simulation at high Reynolds number. Journal of Fluids and Structures (2019), https://doi.org/10.1016/j.jfluidstructs.2019.02.011.

Concerning the turbulence modelling, the Organised Eddy Simulation (OES) approach (Braza et al., 2006, Bourguet et al., 2008 and Szubert et al., 2015b) is used in order to simulate the present flows at high Reynolds numbers governed by the dynamics of coherent structures and chaotic turbulence. Based on our previous studies, this approach ensures a correct representation of the complex interaction between coherent structures and chaotic turbulence and it is efficient even in two-dimensional computations. Furthermore, it allows predicting the dynamics of the shock–vortex interaction.

3. Results

First, the static configuration will be examined as well as the dynamics of buffet. Secondly, vibration effects of the rear part will be investigated with respect to the buffet dynamics at angles of incidence $\alpha = 1.8°$ and $\alpha = 5°$. Finally, two morphing effects are discussed concerning the aerodynamic performances.

3.1. Analysis of the buffet dynamics in relation with the shear layer and wake structure

The buffet phenomenon displaying a periodic shock motion and the associated growth and thinning of the separated area is illustrated in Figs. 3(a)–3(f). These figures correspond to $\alpha = 5°$. This angle of incidence enhances the shearing mechanisms and the coherent structure appearance.

Fig. 4 shows the longitudinal density gradient isocontours together with streaklines generated from $x/c \approx 0.6$. The particles shed in the flow highlight the boundary layer separation, the shear layer and wake instabilities leading to Von Kármán vortices. Following the shock motion along the suction side, the boundary layer becomes thinnest as the shock is in the most downstream position (Fig. 4(a)) while the separated region becomes thickest as the shock reaches its most upstream position (Fig. 4(b)). This is accompanied by the appearance of Kelvin–Helmholtz vortices along the separated shear layer. A video with the overall motion of the flow dynamics can be found in http://smartwing.org/SMS/EU/streaklines_video_transonic_interaction_a320/. Fig. 4(c) is a zoom around the lambda shock pattern and the separated region. It displays the motion of the streakline particles below this pattern up to positions upstream of the shock foot. These facts indicate the strong feedback effect between the separated region and the shock and a momentum transfer upstream creating a local thickening of the boundary layer and an acceleration area above it. This is associated with the first oblique supersonic formation indicated by the arrow. This pattern is actually observed practically in a systematic way in a number of Schlieren experimental visualisations (Duncan et al., 1932 and https://history.nasa.gov/SP-440/ch7-2.htm). The overall separated area together with the upstream boundary layer thickness form an “effective obstacle” thicker than the nominal airfoil, surrounded by an irrotational flow. It would be possible to evaluate the shock positions by an Euler computation around the shape of this effective obstacle.

The interaction between two (or among three or more) predominant incommensurate frequencies governing a dynamic system issued from the development of the turbulent motion around the body is known to produce new frequencies towards a filling-up of the energy spectrum by a multitude of frequencies including distinct peaks due to the coherent structures and continuous frequency ranges due to the chaotic turbulence. This was shown in experimental studies past a cylinder in high Reynolds number by Braza et al. (2006, cf. spectrum in p. 761, fig. 2b) among other studies. A similar behaviour was obtained in the experimental study by Jodin et al. (2017, p. 285, fig. 28). Hence, the turbulent spectrum displays distinct peaks corresponding to these predominant frequencies and new frequencies which are combination of the previous ones, as well as interspersed continuous frequency regions associated with chaotic turbulence motion. The interaction among all these patterns leads to a complex turbulence motion in which persists the trace of the coherent motion related to each main predominant frequency. The generation of this chaos is known to be non-linear, despite the fact that the new generated frequencies are linear expressions of the initial predominant ones, of the kind $mf_1 \pm nf_2$. This scenario had been mathematically analysed by Newhouse et al. (1978), reported for instance in Guzman and Amon (1994, p. 2001), mentioned in previous studies by Braza et al. (1990, p. 1469), among others. The non-linearity can be also understood by the fact that the amplitudes of the predominant frequencies are not «doubled» if the upstream velocity is doubled. This fact is known by a number of studies, as for example in Hoarau et al. (2003, p.66, fig. 1a), where in the spectrum the amplitudes of the predominant peaks do not increase proportionally to an increase in the Reynolds number. In the present case, predominant frequencies shown in the spectrum of Fig. 10 are: the buffet mode, named f_B, the frequency corresponding to the von Kármán mode, f_{VK} which corresponds to the bump indicated in this figure. The bump formation around the von Kármán mode is due in the present case to a smearing of the alternating eddies in respect of amplitude and phase irregularities due to the high-Reynolds number chaotic motion. A representative frequency of this mode can be detected as a peak having a maximum amplitude within the bump, as was analysed in similar transonic regimes by Szubert et al. (2015b, p. 285). In the present study, it is indicated in Fig. 6 as f_{VK}, a representative peak in the bump region corresponding to the alternating vortex shedding, identified by tracking the vortices shed in the wake. These facts are associated to feedback effects as described in the following.

In the bump region, in addition to the main oscillations, there appears a smaller pattern characterised by a frequency named «f_p» of lower amplitude. The high amplitude of the main frequencies in the bump progressively diminishes towards lower frequency values (towards the left of the figure). Around the frequency range of 3500 towards 3000 Hz, an inversion in the magnitude of this amplitude and of the f_p peak occurs, because the amplitude of this mode becomes higher and is progressively merged with the harmonics of the buffet frequency for lower frequency values (left hand side of the figure).

Please cite this article as: J.-B. Tô, N. Simiriotis, A. Marouf et al., Effects of vibrating and deformed trailing edge of a morphing supercritical airfoil in transonic regime by numerical simulation at high Reynolds number. Journal of Fluids and Structures (2019), https://doi.org/10.1016/j.jfluidstructs.2019.02.011.

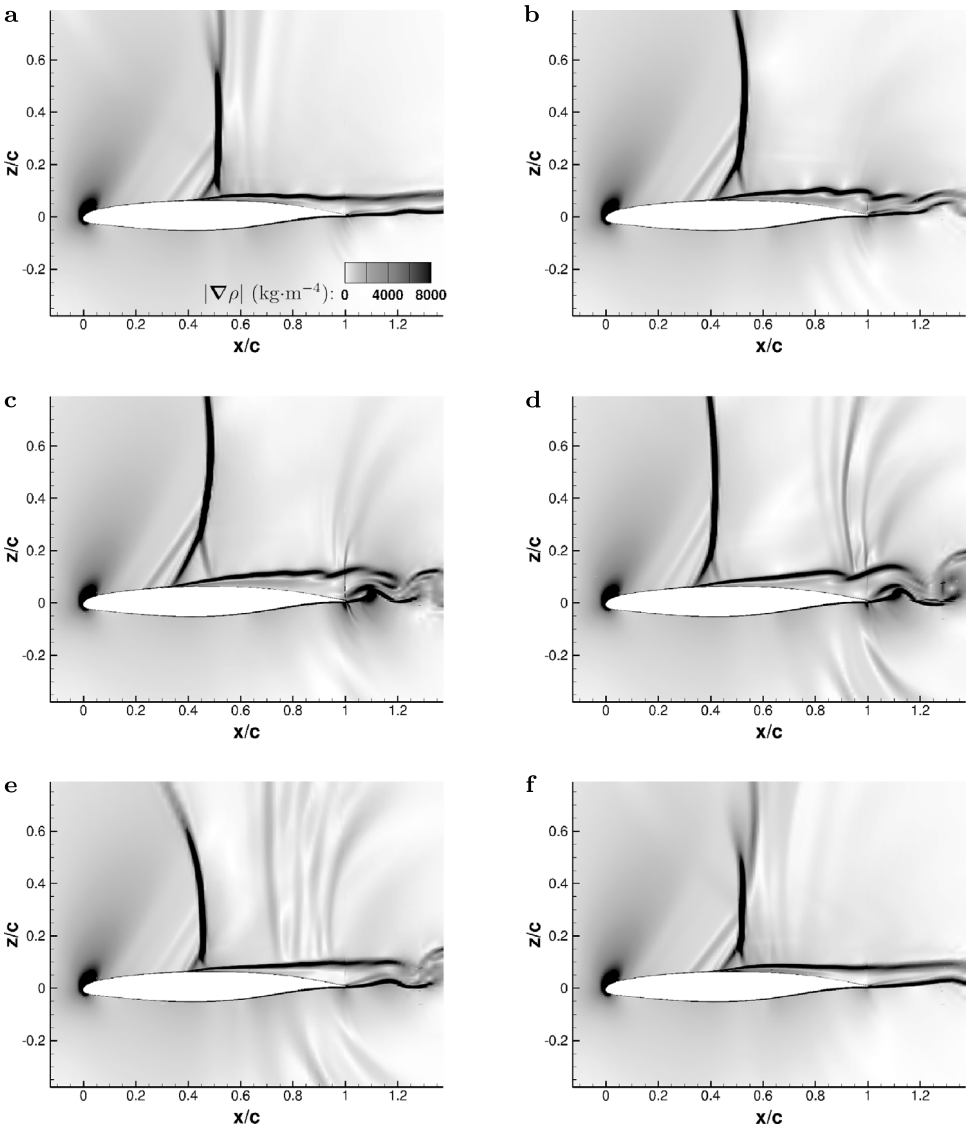

Fig. 3. One buffet period represented by 6 snapshots. From left to right, top to bottom, the pictures correspond to times $t^* = \{0; \frac{1}{5}; \frac{2}{5}; \frac{3}{5}; \frac{4}{5}; 1\}$ where t^* is a non-dimensional time defined by $t^* = \frac{t-t_0}{T_b}$, T_b being the buffet period and t_0 the arbitrary moment chosen as the beginning of one buffet period. Here, t_0 corresponds to a moment when the shock is weakest, i.e. when it reaches its most downstream position (see Tijdeman, 1977).

Due to the fact that the buffet frequency is in the low frequency range ($f_B \approx 110$ Hz), this mechanism occurs towards upstream spatial positions in the vicinity of the shock, illustrating therefore a feedback mechanism among the near wake region and the SWBLI. Furthermore, this figure indicates the appearance of the aforementioned interaction between f_B and f_{VK}, by considering for example the peak at $f_1 = f_{VK} - 8f_B$. It can be seen that any of the peaks at frequencies lower than f_1 are of the kind $f_{VK} - nf_B$ with n integer. Therefore, these elements illustrate the feedback mechanism between the near wake region and the shock motion upstream.

Therefore, the shear layer and wake instabilities growing in the separated area and in the near wake significantly affect the SWBLI region and the shock buffet. We will show that morphing appropriately uses the feedback effects from the near-trailing edge and wake area towards the shock area. This study will show the possibility of buffet attenuation by manipulating the shear layer and coherent structure dynamics, with high benefits in the aerodynamic performance.

3.2. The effects of morphing

3.2.1. The effect of a vibrating trailing edge

Morphing in this study is achieved numerically using the ALE method to deform the trailing edge (see Fig. 7) by either deflecting it upwards quasi-statically or making it vibrate at higher frequencies. This flexible high-frequency vibration

Please cite this article as: J.-B. Tô, N. Simiriotis, A. Marouf et al., Effects of vibrating and deformed trailing edge of a morphing supercritical airfoil in transonic regime by numerical simulation at high Reynolds number. Journal of Fluids and Structures (2019), https://doi.org/10.1016/j.jfluidstructs.2019.02.011.

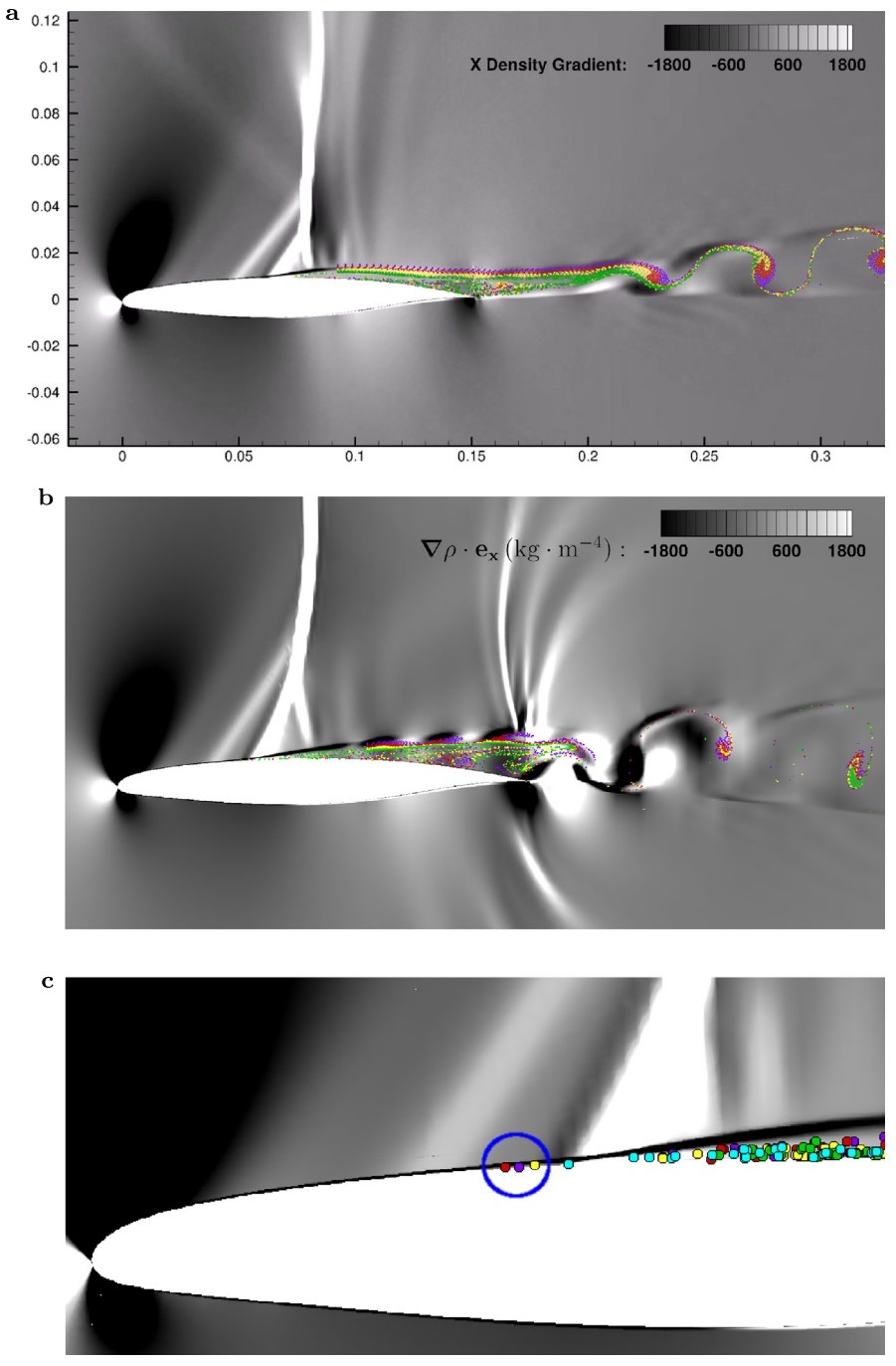

Fig. 4. Visualisation of the transonic interaction dynamics for $\alpha = 5°$ by means of longitudinal density gradient isocontours and streaklines (coloured particles): (a) Shock at the most downstream position corresponding to the thinnest separated boundary layer; (b) Shock at the most upstream position, corresponding to the thickest separated shear layer region (c) Zoom showing the particles moving upstream of the shock foot. (For interpretation of the references to colour in this figure legend, the reader is referred to the web version of this article.)

of the trailing edge, here denoted "flapping" can be performed at various frequencies and was experimentally realised by Jodin et al. (2017), where morphing at multiple time and length scales was done thanks to different classes of electric actuators, the so-called hybrid electroactive morphing (Scheller et al., 2015).

The effects of morphing on aerodynamic forces are firstly investigated for cases where the trailing edge is made to vibrate at various frequencies between 70 Hz and 500 Hz for an angle of incidence $\alpha = 1.8°$, of the same order or

Please cite this article as: J.-B. Tô, N. Simiriotis, A. Marouf et al., Effects of vibrating and deformed trailing edge of a morphing supercritical airfoil in transonic regime by numerical simulation at high Reynolds number. Journal of Fluids and Structures (2019), https://doi.org/10.1016/j.jfluidstructs.2019.02.011.

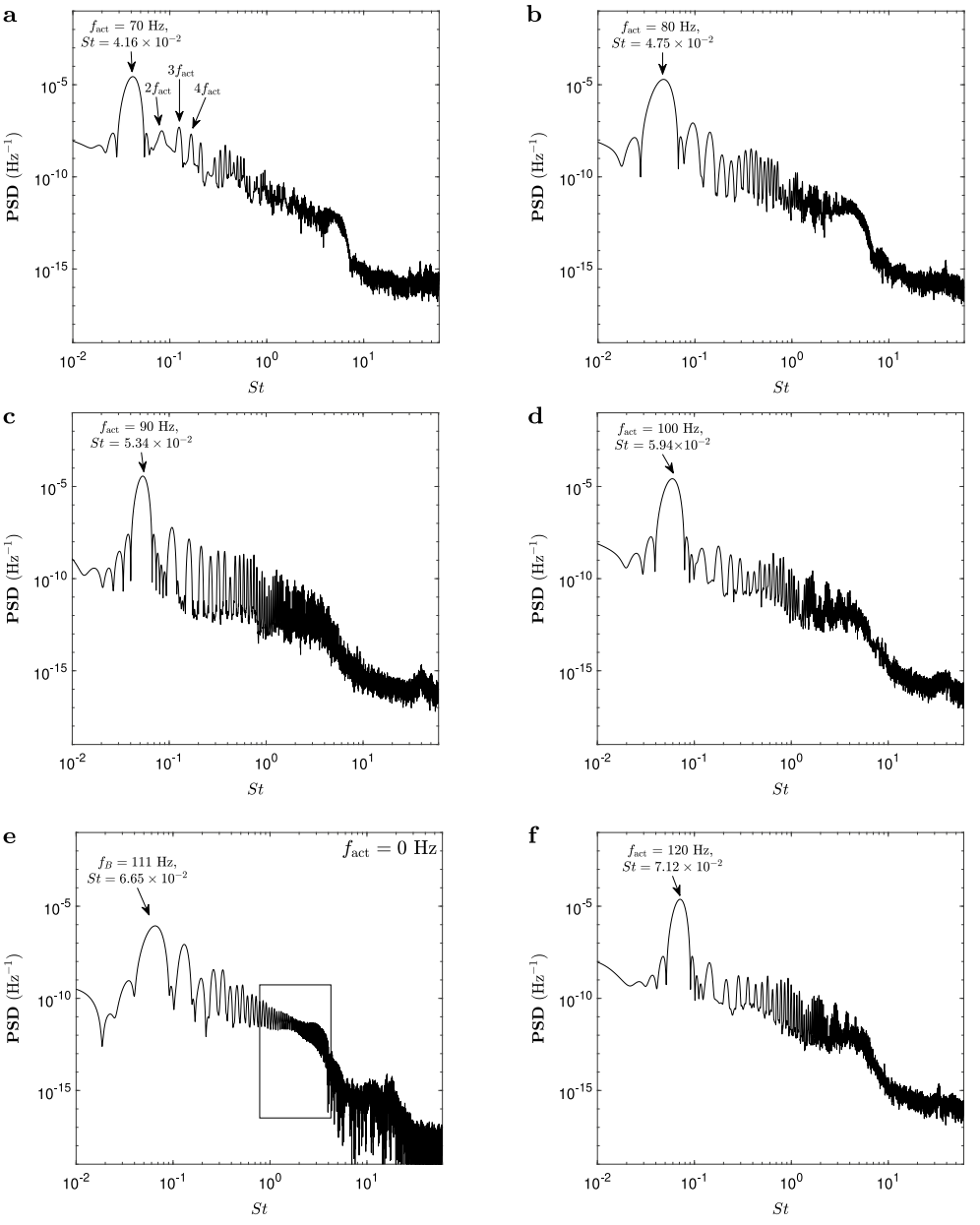

Fig. 5. Power spectral density of the lift coefficient for different actuation frequencies, for the following frequencies: $f_{act} = \{0; 70; 80; 90; 100; 120\}$ Hz. f_{act} (Fig. 5(e)) corresponds to the static case.

magnitude as the natural frequency of the buffet instability, which has been found to be $f_B = 111$ Hz, therefore a Strouhal number of $St = 6.65 \times 10^{-2}$.

Flapping is thus performed at $f_{act} = 70; 80; 90; 100$ and 120 Hz that are neighbouring the natural frequency of buffet $f_B = 111$ Hz for a static wing at an angle of incidence $\alpha = 1.8°$. Afterwards, the influence of higher frequency actuations in the range [200, 500] Hz have been investigated.

For all actuation frequency cases examined, it has been found the buffet frequency locks on the flapping frequency, as shown in Figs. 5(a)–5(d) and 5(f) by means of spectral analysis using a sliding windowing FFT (cf. Welch, 1967).

In fact, the upward movement of the trailing edge compresses the boundary layer, forcing it to move up while the downward movement in the second part of a flapping cycle induces a slight pressure decrease in the boundary layer over the suction side of the wing. This leads the boundary layer to follow the exact same motion as the trailing edge, thus imposing the frequency of the buffet instability.

Please cite this article as: J.-B. Tô, N. Simiriotis, A. Marouf et al., Effects of vibrating and deformed trailing edge of a morphing supercritical airfoil in transonic regime by numerical simulation at high Reynolds number. Journal of Fluids and Structures (2019), https://doi.org/10.1016/j.jfluidstructs.2019.02.011.

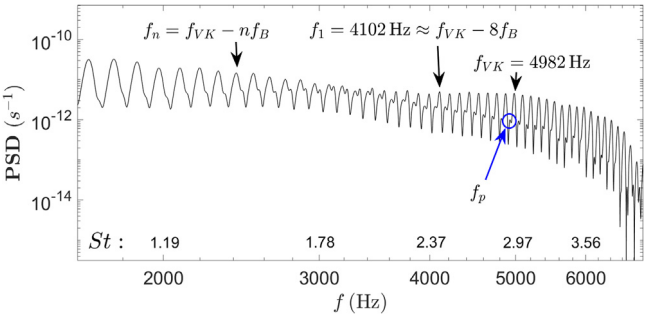

Fig. 6. Zoom of the rectangular box area in Fig. 5(e).

Table 1
Relative change (percentage) of lift, drag and lift-to-drag coefficients between the morphing case and the static case for various actuation frequencies.

Frequency of actuation (Hz)	200	300	400	500
$\frac{\langle C_l\rangle - \langle C_l\rangle_{\text{static}}}{\langle C_l\rangle_{\text{static}}} \times 100$	+1.18%	+1.31%	+0.95%	+1.43%
$\frac{\langle C_d\rangle - \langle C_d\rangle_{\text{static}}}{\langle C_d\rangle_{\text{static}}} \times 100$	+1.31%	+1.22%	+0.88%	+1.09%
$\frac{\langle C_l/C_d\rangle - \langle C_l/C_d\rangle_{\text{static}}}{\langle C_l/C_d\rangle_{\text{static}}} \times 100$	−0.21%	+0.09%	+0.06%	+0.33%

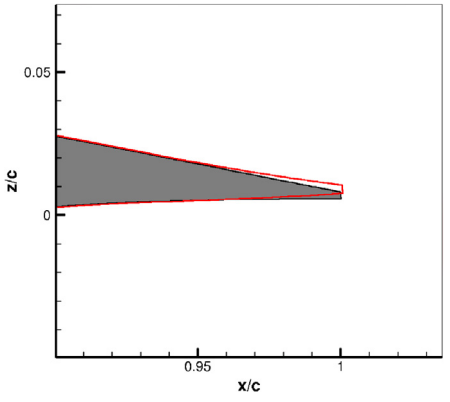

Fig. 7. Zoom on the upward deflected trailing edge area (red) compared to the static A320 trailing edge. (For interpretation of the references to colour in this figure legend, the reader is referred to the web version of this article.)

Additionally, the actuation was found to increase the amplitude of the force oscillations due to buffet as seen in Fig. 8 for instance. This arises from the increased aerodynamic loads due to the movement of the trailing edge, and the unsteady motion of the shock and boundary layer which has been locked on the actuation frequency.

This explains why the *rms* of the forces (cf. 8 and 9) increase.

Table 1 presents the relative changes of the average aerodynamic forces (lift, drag and lift to drag ratio). An increase of the lift coefficient can be noted in all cases. However this increase is more pronounced in the vicinity of 300 Hz and 500 Hz. The drag coefficient decreases in the range of 300 to 400 Hz. The lift to drag ratio increases as a function of the vibration frequency with a slight decrease around 400 Hz.

3.2.2. Effects of an upward trailing edge deflection in static configuration and combined with a vibrating motion

A slight deflection upwards of the trailing edge is considered (order of 2°, cf. Fig. 7). This deflection locally changes the incidence of the flow around the trailing edge and reduces the adverse pressure gradient causing a consequent thinning of the separated region. Therefore, the interaction between the shearing region and the shock is weaker than in the static case and consequently buffet is attenuated.

In Fig. 8, the lift coefficient is plotted versus time at $\alpha = 1.8°$. In the static case, the periodic motion is due to the buffet phenomenon. In the configuration corresponding to the upward deflection without vibration, a reduction in the lift

Please cite this article as: J.-B. Tô, N. Simiriotis, A. Marouf et al., Effects of vibrating and deformed trailing edge of a morphing supercritical airfoil in transonic regime by numerical simulation at high Reynolds number. Journal of Fluids and Structures (2019), https://doi.org/10.1016/j.jfluidstructs.2019.02.011.

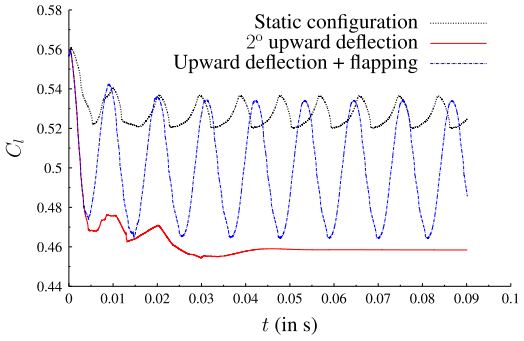

Fig. 8. Lift coefficients for $\alpha = 1.8°$.

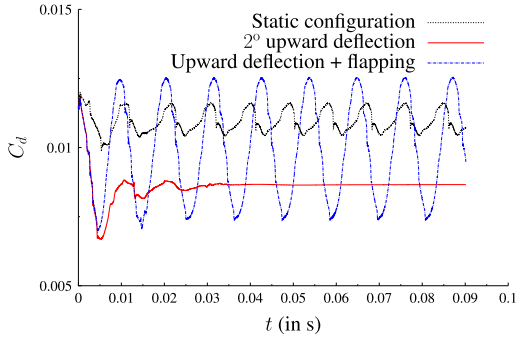

Fig. 9. Drag coefficients for $\alpha = 1.8°$.

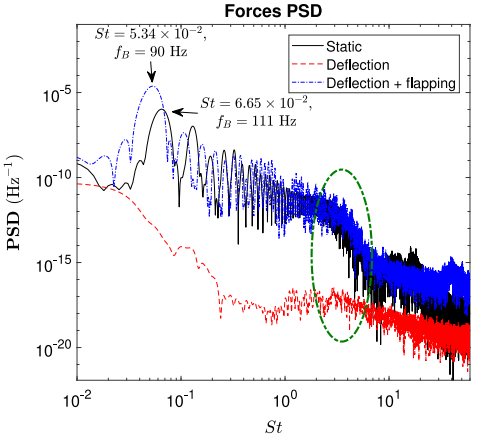

Fig. 10. Energy spectra for $\alpha = 1.8°$. The Von Kármán region is highlighted by the green ellipse.

coefficient is obtained but the lift *rms* becomes almost zero. As shown in Fig. 9 and by Table 3, the average drag coefficient value diminishes by 21.1% when a deflection of the trailing edge is applied. Finally, a combined deflection and vibration at 90 Hz shows a lower average lift decrease but higher lift *rms* values, cf. Table 4. For this case, the drag coefficient also shows a higher *rms* and a slightly higher mean value than the deflected case. The relative percentages are shown in Tables 3, 4.

The lift to drag ratio is presented in Table 2. While a good percentage increase corresponds to the combined case, an even higher benefit is obtained for the deflected case for the angle of incidence $\alpha = 1.8°$ corresponding to the cruise standard incidence.

The morphing effects in the frequency domain are shown in Fig. 10. The static case displays a bump in the low frequency range with a predominant frequency of 111 Hz. Harmonics of this fundamental frequency are also shown to

Please cite this article as: J.-B. Tô, N. Simiriotis, A. Marouf et al., Effects of vibrating and deformed trailing edge of a morphing supercritical airfoil in transonic regime by numerical simulation at high Reynolds number. Journal of Fluids and Structures (2019), https://doi.org/10.1016/j.jfluidstructs.2019.02.011.

Table 2
Relative change in terms of mean lift to drag ratio compared to the static case. Note that D means "2° deflection" and "D + F" is the superposition of an immobile upward deflection and a 90 Hz flapping motion.

Incidence	$\alpha = 1.8°$		$\alpha = 5°$	
Type of actuation	D	D + F	D	D + F
$\frac{\langle C_l/C_d\rangle - \langle C_l/C_d\rangle_{\text{static}}}{\langle C_l/C_d\rangle_{\text{static}}} \times 100$	+10.4%	+4.3%	+2.5%	+0.4%

Table 3
Relative change of mean drag compared to the static case.

Incidence	$\alpha = 1.8°$	
Type of actuation	D	D + FF
$\frac{\langle C_d\rangle - \langle C_d\rangle_{\text{static}}}{\langle C_d\rangle_{\text{static}}} \times 100$	−21.1%	−9.47%

Table 4
Relative change of mean lift compared to the static case.

Incidence	$\alpha = 1.8°$	
Type of actuation	D	D + FF
$\frac{\langle C_l\rangle - \langle C_l\rangle_{\text{static}}}{\langle C_l\rangle_{\text{static}}} \times 100$	−12.9%	−5.37%

extend towards Strouhal number ranges near 1, where a second frequency bump is formed. This corresponds to the Von Kármán instability mode and its interaction with the shear layer vortices past the trailing edge and in the near-wake.

The region between this bump and the buffet's bump illustrates the non-linear interaction and feedback effects from the trailing edge and near-wake coherent structures to the SWBLI region and vice versa.

It is clear that morphing manages to reduce both the average values lift and drag, as well as to increase the mean lift to drag ratio. The drag reduction is due to the diminution of the separated region's size thanks to the adverse pressure gradient decrease near the trailing edge by means of morphing. The flapping motion actuated with quite small amplitudes (order of 0.2 mm) generates small scale vortices interacting with the separated shear layers delimiting the Turbulent/Non-Turbulent (TNT) interfaces, creating a shear sheltering through the eddy-blocking effect (Szubert et al., 2015b and Hunt et al., 2008). This results in a shape drag reduction and consequently a reduction of the overall drag.

4. Conclusions

This paper enlightens the buffet dynamics strongly related with the shear layer and near-wake structure. The modification in the width of the separated region and of the coherent vortices near the trailing edge has been quantified and associated with the shock's motion along the suction side. It has been shown through streaklines visualisation that the reverse flow passes through the lambda shock region towards a position upstream of the shock. This explained the formation of an oblique shock region upstream of the normal shock, visible in a considerable number of Schlieren experimental visualisations and less discussed up to now.

This article thus makes evidence of considerable feedback effects of the near trailing edge dynamics in relation to the SWBLI. The actuations investigated made use of these effects to produce a lock-in of the buffet's frequency with the actuation frequency and furthermore to reduce the separated region and wake's width. The slight upwards deflection has proven the most efficient in respect of lift to drag increase and drag reduction as well as a simultaneous *rms* reduction. These facts are crucial for the design because buffet onset leads to a high rise of drag and in extreme conditions can trigger dangerous dip-flutter modes.

Acknowledgements

The authors are grateful to the LAPLACE (Laboratoire Plasma et Conversion d'Energie), France, UMR CNRS-INPT-UT3 No 5213, research group GREM3 on electrodynamics and to the National Supercomputing centers CALMIP, CINES and IDRIS for the Computer allocation, as well as the PRACE Supercomputing, France allocation N° 2017174208. This study has been realised under the H2020 European Research programme N° 723402: SMS, "Smart Morphing and Sensing for aeronautical configurations", http://smartwing.org/SMS/EU/.

Please cite this article as: J.-B. Tô, N. Simiriotis, A. Marouf et al., Effects of vibrating and deformed trailing edge of a morphing supercritical airfoil in transonic regime by numerical simulation at high Reynolds number. Journal of Fluids and Structures (2019), https://doi.org/10.1016/j.jfluidstructs.2019.02.011.

References

Barbut, G., Braza, M., Hoarau, Y., Barakos, G., Sévrain, A., Vos, J.B., 2010. Prediction of transonic buffet around a wing with flap. Notes Numer. Fluid Mech. Multidiscip. Des. 111, 191–204.
Bonne, N., 2018. Stabilité de l'interaction onde de choc/couche limite laminaire (Ph.D. thesis). Université Paris-Saclay.
Bouhadji, A., Braza, M., 1998. Physical analysis of unsteady viscous flow phenomena around a wing by Direct Navier–Stokes Simulation. In: Proceedings of the 4th ECCOMAS Computational Fluid Dynamics Conference.
Bourdet, S., Bouhadji, A., Braza, M., Thiele, F., 2003. Direct numerical simulation of the three-dimensional transition to turbulence in the transonic flow around a wing. Flow Turbul. Combust. 71 (1–4), 203–220, (formerly Applied Scientific Research).
Bourguet, R., Braza, M., Harran, G., El Akoury, R., 2008. Anisotropic organised Eddy simulation for the prediction of non-equilibrium turbulent flows around bodies. J. Fluids Struct. 24 (8), 1240–1251.
Braza, M., Barbut, G., Miller, M., Kania, W., Hoarau, Y., Barakos, G., Sévrain, A., 2011. NACA0012 with Aileron. Notes Numer. Fluid Mech. Multidiscip. Des. 114.
Braza, M., Chassaing, P., Minh, H. Ha, 1990. Prediction of large-scale transition features in the wake of a circular cylinder. Phys. Fluids A 2 (8), 1461–1471.
Braza, M., Perrin, R., Hoarau, Y., 2006. Turbulence properties in the cylinder wake at high Reynolds numbers. J. Fluids Struct. 22 (6–7), 757–771.
Brunet, V., 2003. Computational study of buffet phenomenon with unsteady RANS equations. In: 21st AIAA Applied Aerodynamics Conference. American Institute of Aeronautics and Astronautics, Reston, Virigina.
Chinaud, M., Rouchon, J.F., Duhayon, E., Scheller, J., Cazin, S., Marchal, M., Braza, M., 2014. Trailing-edge dynamics and morphing of a deformable flat plate at high Reynolds number by time-resolved PIV. J. Fluids Struct. 47, 41–54.
Deck, S., 2005. Numerical simulation of transonic buffet over an airfoil. AIAA J. 43 (7), 1556–1566.
Doerffer, P., Flaszynski, P., Hirsch, C., Dussauge, J. -P., Babinsky, H., Barakos, G.N., 2019. Sci. Eds., Transition Location Effect on Shock Wave Boundary Layer Interaction. Notes on Numerical Fluid Mechanics and Multidisciplinary Design, vol. (in print), Springer.
Doerffer, P., Hirsch, C., Dussauge, J. -P., Babinsky, H., Barakos, G.N., 2011. Sci. Eds., Unsteady Effects of Shock Wave Induced Separation. Notes on Numerical Fluid Mechanics and Multidisciplinary Design, vol. 114, Springer.
Duncan, W.J., Ellis, L., Scruton, C., 1932. First report on the general investigation of tail buffeting. Aeronaut. Research. Com. R. & M. 1457 (part I).
Flaszynski, P., Doerffer, P., Szwaba, R., Piotrowicz, M., Kaczynski, P., 2018. Laminar-turbulent transition tripped by step on transonic compressor profile. J. Therm. Stresses 27 (1), 1–7.
Grossi, F., Braza, M., Hoarau, Y., 2014. Prediction of transonic buffet by delayed Detached–Eddy simulation. AIAA J. 52 (10), 2300–2312.
Guzman, A.M., Amon, C.H., 1994. Transition to chaos in converging-diverging channel flows: Ruelle–Takens–Newhouse scenario. Phys. Fluids 6 (6), 1994–2002.
Hoarau, Y., Braza, M., Ventikos, Y., Faghani, D., Tzabiras, G., 2003. Organized modes and the three-dimensional transition to turbulence in the incompressible flow around a NACA0012 wing. J. Fluid Mech. 496.
Hoarau, Y., Pena, D., Vos, J.B., Charbonnier, D., Gehri, A., Braza, M., Deloze, T., Laurendeau, E., 2016. Recent developments of the Navier Stokes multi block (NSMB) CFD solver. In: 54th AIAA Aerospace Sciences Meeting. In: AIAA SciTech Forum, American Institute of Aeronautics and Astronautics.
Hunt, J.C.R., Eames, I., Westerweel, J., 2008. Vortical interactions with interfacial shear layers. In: Kaneda, Yukio (Ed.), IUTAM Symposium on Computational Physics and New Perspectives in Turbulence. Springer Netherlands, Dordrecht, pp. 331–338.
Jacquin, L., Molton, P., Deck, S., Maury, B., Soulevant, D., 2005. An experimental study of shock oscillation over a transonic supercritical profile. In: 35th AIAA Fluid Dynamics Conference and Exhibit. American Institute of Aeronautics and Astronautics, Reston, Virigina.
Jacquin, L., Molton, P., Deck, S., Maury, B., Soulevant, D., 2009. Experimental study of shock oscillation over a transonic supercritical profile. AIAA J. 47 (9), 1985–1994.
Jodin, G., Motta, V., Scheller, J., Duhayon, E., Döll, C., Rouchon, J.F., Braza, M., 2017. Dynamics of a hybrid morphing wing with active open loop vibrating trailing edge by time-resolved piv and force measures. J. Fluids Struct. 74, 263–290.
Levy, Jr., L.L., 1978. Experimental and computational steady and unsteady transonic flows about a thick airfoil. AIAA J. 16 (6), 564–572.
Marvin, J.G., Levy, Jr., L.L., Seegmiller, H.L., 1980. Turbulence modeling for unsteady transonic flows. AIAA J. 18 (5), 489–496.
McDevitt, J.B., Levy, Jr., L.L., Deiwert, G.S., 1976. Transonic flow about a thick circular-arc airfoil. AIAA J. 14 (5), 606–613.
Newhouse, S., Ruelle, D., Takens, F., 1978. Communications in Mathematical Physics, volume 64. Springer-Verlag, pp. 35–40.
Scheller, J., 2015. Electroactive morphing for the aerodynamic performance improvement of next generation airvehicles (Ph.D. thesis). Toulouse, INPT.
Scheller, J., Chinaud, M., Rouchon, J.F., Duhayon, E., Cazin, S., Marchal, M., Braza, M., 2015. Trailing-edge dynamics of a morphing NACA0012 aileron at high Reynolds number by high-speed PIV. J. Fluids Struct. 55, 42–51.
Seegmiller, H.L., Marvin, J.G., Levy, L.L., 1978. Steady and unsteady transonic flow. AIAA J. 16 (12), 1262–1270.
Szubert, D., Asproulias, I., Grossi, F., Duvigneau, R., Hoarau, Y., Braza, M., 2015a. Numerical study of the turbulent transonic interaction and transition location effect involving optimisation around a supercritical aerofoil. Eur. J. Mech. B/Fluids 55, 380–393.
Szubert, D., Grossi, F., Jimenez Garcia, A., Hoarau, Y., Hunt, J.C.R., Braza, M., 2015b. Shock-vortex shear-layer interaction in the transonic flow around a supercritical airfoil at high reynolds number in buffet conditions. J. Fluids Struct. 55, 276–302.
Tijdeman, H., 1977. Investigation of the Transonic Flow Around Oscillating Airfoils. National Aerospace Lab, Amsterdam, Netherlands, TR-77-090U.
Welch, P., 1967. The use of fast Fourier transform for the estimation of power spectra: A method based on time averaging over short, modified periodograms. IEEE Trans. Audio Electroacoust. 15 (2), 70–73.
Zilli, D.M., 2015. Numerical Simulation and modeling of morphing deformation on a supercritical airfoil wing at high Reynolds number (Eng. Diploma thesis), ENSEEIHT. Institut National Polytechnique Toulouse, Toulouse.

Please cite this article as: J.-B. Tô, N. Simiriotis, A. Marouf et al., Effects of vibrating and deformed trailing edge of a morphing supercritical airfoil in transonic regime by numerical simulation at high Reynolds number. Journal of Fluids and Structures (2019), https://doi.org/10.1016/j.jfluidstructs.2019.02.011.

Chapter 7

Parametric study on the morphing frequency and phenomenology

This section presents the results from 2D computations carried out on the A320 airfoil in the transonic regime, under the previously described physical conditions. At first, a parametric analysis has been made to determine the frequencies that yield an increase of lift, a decrease of drag and an increase of lift to drag ratio. The trailing edge is actuated at different frequencies belonging to the set

$$f = \{100, 150, 200, 250, 300, 350, 400, 450, 500, 700, 720, 750, 800, 1000, 1500\}$$

Hz.

In the second part of this study, an emphasis is given on understanding why some actuation frequencies result in better lift or drag coefficients, or weaker unsteady oscillations around the mean (weaker RMS values). Subsequent spectral analysis, time-frequency analysis by means of wavelet transforms as well as time-averaged wake velocity profiles help in extracting this information from the computations. The goal of this second part is to assess the effect of trailing-edge morphing on the manipulation of the SWBLI and the simultaneous reduction of pressure drag and friction drag linked to a decrease of wake thickness and the reduced intensity of flow recirculation over the wing due to a feedback effect.

After two optimal frequency regions were identified, a third study has been done to better characterize the nature of drag reduction and lift increase

for these frequencies. Focusing on the parametric study around the two optimal frequency ranges has enabled more effort to be spent on time-frequency analysis to help pinpoint the reason for wake shrinking and a diminished adverse pressure gradient at the aft end of the airfoil.

7.1 Comparison between different types of trailing edge morphing and parametric study

A first paragraph presents a comparison between two types of morphing: a periodic oscillation of the trailing edge by $\pm 1°$ about the airfoil's cross sectional neutral axis and a second type of actuation which involves the combination of the aforementioned periodic oscillation superimposed over a slight upward deformation of the trailing edge by 2° (fig. 7.1).

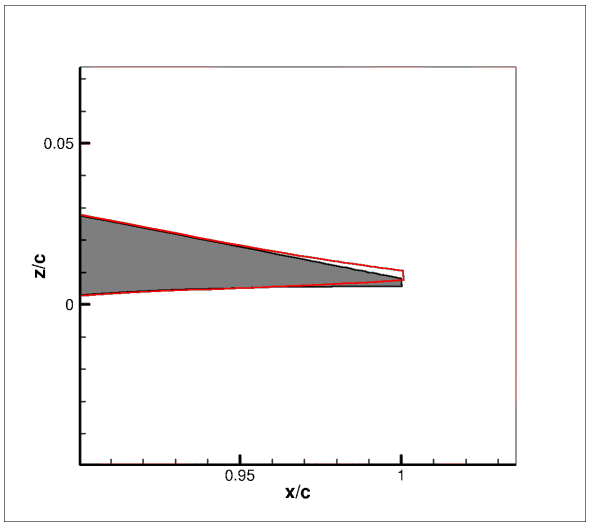

Figure 7.1: The gray shape is the airfoil's trailing edge while the red outline represents the upward deflection of the trailing edge by an angle of 2°.

The time series of the lift coefficient and drag coefficient are represented below in figures 7.2(a) and (b):

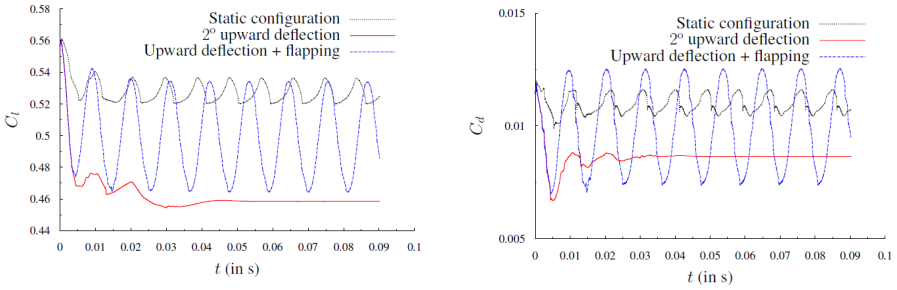

(a) Lift coefficient (b) Drag coefficient

Figure 7.2: Time series of the force coefficients for the static case (black line) and two types of morphing.

It can be remarked that the static configuration, depicted by the black dotted curve in figure 7.2 (a) and 7.2 (b), presents a quasi-periodic unsteadiness. This is the hallmark of buffet. This instability results from an interaction between the shock – that comes from the strong flow acceleration over the curved airfoil – and the boundary layer as well as near-wake unsteadiness and related instability modes. The onset of buffet is characterized by a spontaneous and coordinated oscillatory motion of both the shock and the boundary layer, inducing quasi-periodic pressure and viscous forces on the surface of the airfoil. When integrated over the airfoil, these local forces lead to a periodic behaviour of the aerodynamic forces.

The red curve depicts aerodynamic forces in the case of a slight upward deflection of the trailing edge (cf. Fig. 7.1). It is obvious that for this configuration, the unsteadiness that was observed in the static case quickly vanishes until the force remains constant over time. This deflection is thus showed to inhibit the onset of buffet although it comes at the price of aerodynamic performance: The time-average of the lift coefficient appears to decrease. But the same is true for drag, which also decreases by a significant amount thus leading to an increased L/D.

The blue curve shows that the force unsteadiness is reinforced when applying the second type of morphing whereby a periodic trailing edge motion is imposed on top of the upward deflection. The peak to peak amplitude, which is linked to the root mean square (rms) of the force time series is indi-

cated to increase for both lift and drag curves. The lift and drag average also appear to decrease compared to the static case, albeit not by as much as is the case for the upward deflection. The following study aims to detect which frequencies provide an improvement in terms of aerodynamic performance and to find explanations as to how morphing acts to control buffet in order to hinder this instability mode and enhance flight efficiency in the transonic regime. It is however important to note that in the following study, morphing is hereafter performed as a vibrational oscillation of the trailing edge around the airfoil neutral axis: No deflection is applied beforehand.

7.1.1 Time-averaged force coefficients for various actuation frequencies

The time-averaged values of the aerodynamic force coefficients are hereby computed for frequencies belonging to the set F. Compared to the static value, the lift coefficient increases for actuation frequencies $f_{ac} = 200$ Hz, $f_{ac} = 400$ Hz, $f_{ac} = 450$ Hz, $f_{ac} = 500$ Hz (fig. 7.3-a and fig. 7.4-a) while there is also a significant increase of drag for these same frequencies (fig. 7.3-b and fig. 7.4-b).

It is noticed that mean lift and drag follow the same trends (fig. 7.3-a and fig. 7.3-b). This suggests that the underlying mechanism explaining lift and drag increase or decrease through vibrational trailing edge morphing is the same. This theory, explaining how trailing edge morphing acts on the pressure distribution around the wing will be explored in more details in a following section.

Several frequencies stand out in terms of performance improvement. In particular, it is noticed that actuation frequency $f_{ac} = 720$ Hz decreases drag by 1.2% and increases lift by 0.3%. This is the only occurrence of an actuation frequency that decreases drag while increasing lift, for an increase of lift to drag by 1.58%. In contrast, it is observed that two frequencies in the lower frequency region ($f_{ac} < 500$ Hz) provide a local maximum of lift to drag ratio: drag is decreased by 3.5% for $f_{ac} = 300$ Hz and by 8.9% for $f_{ac} = 350$ Hz. This is achieved for a minimal decrease in lift, by 1.1% and 3.8% for $f_{ac} = 300$ and 350 Hz respectively. This signifies that lift to drag ratio increases by up to 5.5% in the case of an actuation frequency of 350 Hz.

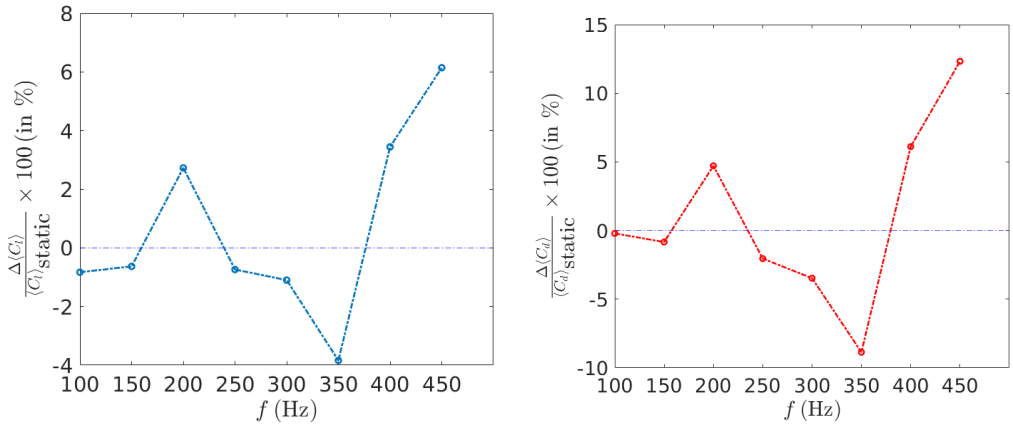

(a) Mean lift force

(b) Mean drag force

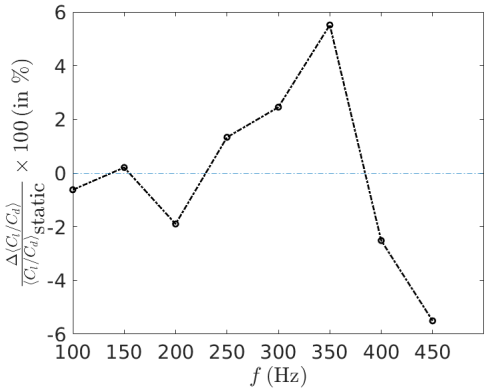

(c) Mean lift to drag ratio

Figure 7.3: Comparison of time-averaged force coefficients for actuation frequency $f_{ac} \leq 450$ Hz.

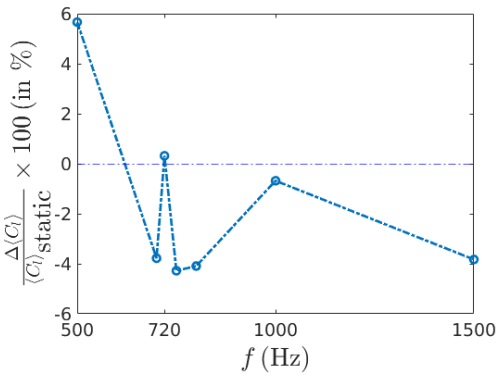

(a) Mean lift force

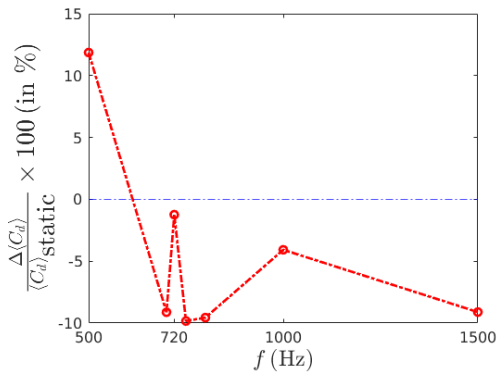

(b) Mean drag force

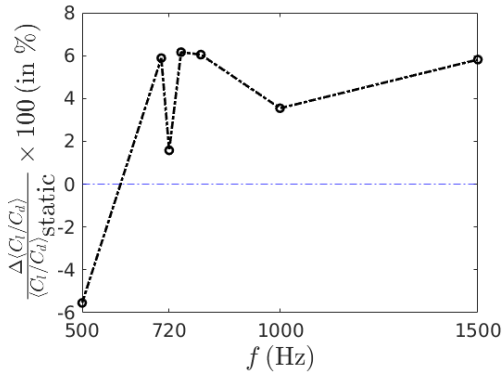

(c) Mean lift to drag ratio

Figure 7.4: Comparison of time-averaged force coefficients for actuation frequency $500 \leq f_{ac} \leq 1500$ Hz.

Frequency (Hz)	100	150	200	250	300	350	400	450
$100 \times \frac{\langle C_d \rangle - \langle C_d \rangle_{\text{static}}}{\langle C_d \rangle_{\text{static}}}$	-0.21%	-0.84%	4.71%	-2.07%	-3.47%	-8.87%	6.11%	12.33%
$100 \times \frac{\langle C_d \rangle - \langle C_d \rangle_{\text{static}}}{\langle C_d \rangle_{\text{static}}}$	-0.83%	-0.63%	2.73%	-0.74%	-1.10%	-3.84%	3.45%	6.12%
$100 \times \frac{\langle C_l/C_d \rangle - \langle C_l/C_d \rangle_{\text{static}}}{\langle C_l/C_d \rangle_{\text{static}}}$	-0.62%	0.20%	-1.89%	1.33%	2.46%	5.51%	-2.52%	-5.50%

Table 7.1: Relative change (percentage) of time-averaged force coefficients with respect to the static case for actuation frequencies ≤ 450 Hz. A positive (resp. negative) value means an increase (resp. decrease) in percents of the force coefficient compared to the static case.

Frequency (Hz)	500	700	720	750	800	1000	1500
$100 \times \frac{\langle C_d \rangle - \langle C_d \rangle_{\text{static}}}{\langle C_d \rangle_{\text{static}}}$	11.86%	-9.13%	-1.24%	-9.83%	-9.56%	-4.07%	-9.11%
$100 \times \frac{\langle C_l \rangle - \langle C_l \rangle_{\text{static}}}{\langle C_l \rangle_{\text{static}}}$	5.66%	-3.78%	0.31%	-4.23%	-4.09%	-0.68%	-3.83%
$100 \times \frac{\langle C_l/C_d \rangle - \langle C_l/C_d \rangle_{\text{static}}}{\langle C_l/C_d \rangle_{\text{static}}}$	-5.54%	5.88%	1.58%	6.16%	6.04%	3.55%	5.81%

Table 7.2: Relative change (percentage) of time-averaged force coefficients with respect to the static case for actuation frequencies $500 \leq f_{ac} \leq 1500$ Hz. A positive (resp. negative) value means an increase (resp. decrease) in percents of the force coefficient compared to the static case.

It is clear from Table 7.1 that an actuation frequency of 350 Hz shows both an important increase in terms of lift to drag ratio (+5.51%) while drag is considerably reduced (-8.87%), at the cost of a relatively small lift increase (+3.84%). This needs to be put in contrast with the actuation frequency $f_{ac} = 720$ Hz which simultaneously presents a decrease of drag (-1.24%)

and a slight increase of lift (+0.31%), for an increase of lift to drag ratio of 1.58%. These two frequencies are deemed to be optimal for transonic flight as they decrease drag, hence potentially cutting fuel consumption whereas lift to drag is enhanced, that is the aerodynamic quality of the morphing wing is bettered over a static wing for these frequencies.

7.1.2 Comparison of mean velocity profile

The mean velocity profile at $x/c = 1.19$ is compared for actuation frequencies 300 Hz, 350 Hz and 400 Hz along with the static case. The width of the velocity profile is found from figure 8.

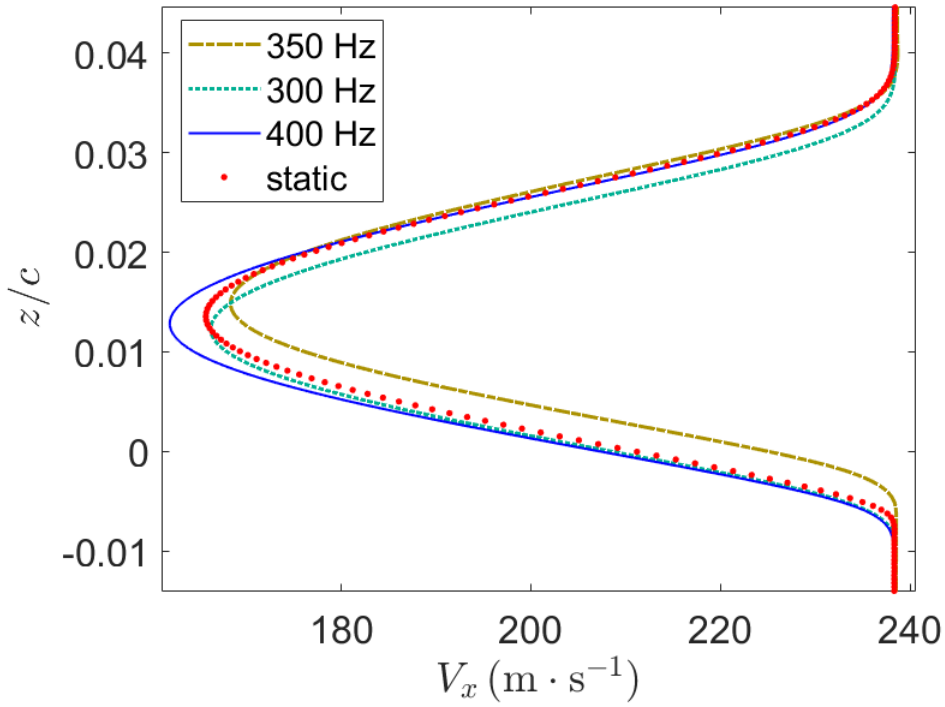

Figure 7.5: Plot of the time-averaged velocity profiles inside the wake at $x/c = 1.19$.

The values of the wake width for actuation frequencies 300 Hz, 350 Hz, 400 Hz and the static case are listed in Table 7.3:

	300 Hz	350 Hz	400 Hz	static
Wake width (in m)	3.33×10^{-2}	3.22×10^{-2}	3.45×10^{-2}	3.43×10^{-2}
Relative width variation compared to the static case	-2.91%	-6.12%	+0.58%	0%

Table 7.3: Wake width for different actuation frequencies and relative width variation compared to the static case (in percents)

It is clear from Table 7.3 that the wake becomes thinner for actuation frequencies 300 Hz and 350 Hz with the lowest thickness reached for $f_{ac} = 350$ Hz, as the wake loses 6.12% of the static wake thickness, while it becomes thicker relative to the static case for $f_{ac} = 400$ Hz. This coincides with the observation that drag is reduced for actuation frequencies 300 and 350 Hz, while it increases for an actuation frequency of 400 Hz. This seems to point to a reduction of wake thickness through a reduction of the strength of adverse pressure gradients via trailing edge morphing, which in turn tends to inhibit the destabilization of the wake and keeps it thinner.

7.1.3 Effect of morphing on the pressure coefficient C_p

The wall pressure coefficient, denoted C_p, is a non-dimensional measure of the wall-pressure value. It is generally computed along a slice that intersects the surface of the wing and is aligned with the streamwise direction. It is found from the following formula :

$$C_p = \frac{2(P - P_\infty)}{\rho_\infty U_\infty^2} \tag{7.1}$$

where:

- P is the surface pressure in Pascals.
- P_∞ is the free-stream static pressure in Pascals.

- ρ_∞ is the free-stream density in kg/m^3.
- U_∞ is the free-stream velocity magnitude in m/s.

C_p profiles are often used as a means of identifying typical flow behavior at particular Reynolds numbers, angles of attack and Mach number, as well as a way to characterize the aerodynamic performance of a certain airfoil under known conditions and provide useful data for later numerical validation.

Figure 7.6 shows the slice along which the C_p is computed and measured:

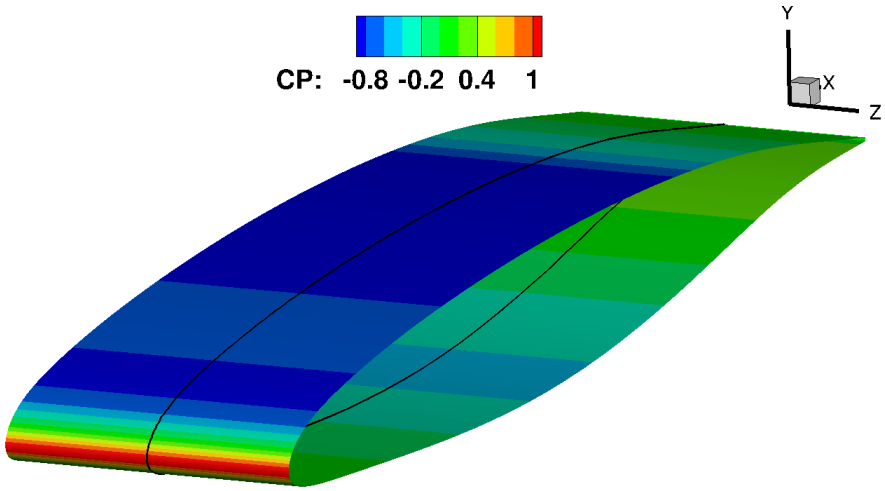

Figure 7.6: Surface pressure coefficient iso-contours with the mark of a slice cutting the wing along the streamwise direction.

The time-averaged C_p curve for actuation frequencies 200 Hz, 350 Hz, 400 Hz and the static case have been compared. From figure 7.7, it can be noted that the area under the time-averaged C_p distribution for an actuation frequency of 400 Hz is more important than that of 350 Hz and static case. This observation demonstrates that a trailing edge oscillation performed at 400 Hz increases pressure compared to the static case, while 350 Hz diminishes the pressure difference near the aft end of the wing. This ultimately impacts both lift and pressure drag. As has been noted in the variation tables and graphs (graphs table 7.1) The impact that morphing has on the

C_p curve is the sign that most of the influence of morphing on aerodynamic performance comes from a modification of the pressure distribution around the wing.

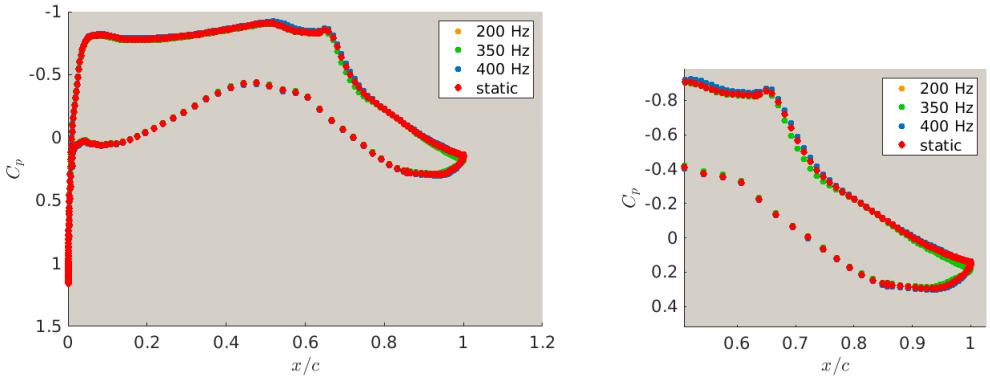

(a) Time-averaged pressure coefficient curve for 350 Hz, 400 Hz and static case

(b) Zoom on the trailing edge portion ($x/c > 0.5$)

Figure 7.7: Time-averaged pressure coefficient C_p extracted along the airfoil circumference

7.1.4 Power Spectral Density (PSD) of Pressure forces

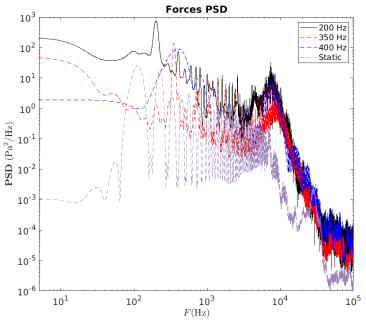

(a) Monitor point at $x/c = 1.1$

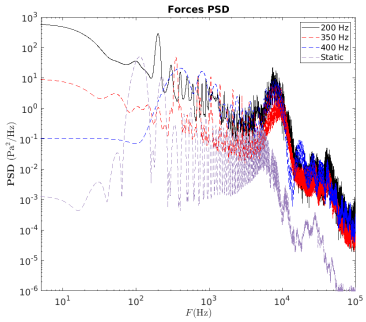

(b) Monitor point at $x/c = 1.2$

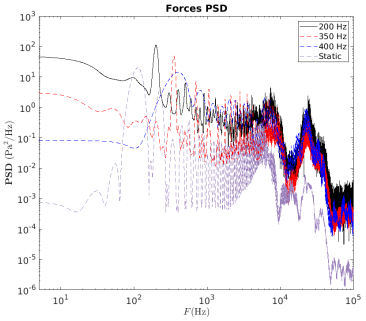

(c) Monitor point at $x/c = 1.3$

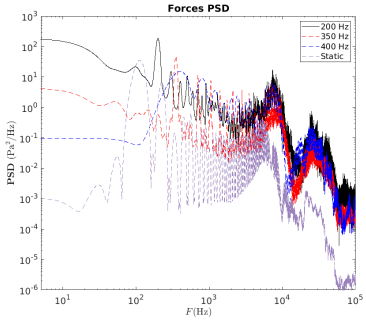

(d) Monitor point at $x/c = 1.4$

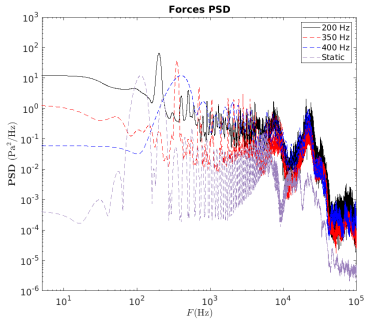

(e) Monitor point at $x/c = 1.5$

Figure 7.8: Power Spectral Density (PSD) plots of pressure forces for $f_{ac} =$ 200, 300, 400 Hz and for the static case as "measured" along monitor points distributed in the wake of the airfoil.

Monitor points are placed at different locations in the wake corresponding to $x/c = 1.1$, 1.2, 1.3, 1.4 and 1.5. Power Spectral Density of pressure forces on these monitor points for actuation frequencies 200 Hz, 350 Hz, 400 Hz and the static case are plotted hereafter.

It is noted in the figures above (fig. 7.8) that the energy associated to the first harmonic of the von Kármán mode increases with the distance aft the trailing edge, in comparison to the fundamental frequency. This observation is true for all actuation frequencies. In contrast, the energy level for the frequency of the von Kármán mode decreases the further downstream the monitor point is located. In addition to this, the power density spectrum of the static case is less energetic than those of all other actuation frequencies, which means that energy is added to the wake instability modes through morphing.

Most importantly, it can be seen in the spectra that for each actuation frequency, a first energetic lobe appears at the actuation frequency. This peak is representative of a mode that is synchronized with the actuation frequency. It is later shown that this corresponds to the buffet instability which often synchronizes with the actuation frequency, which we denote here as a lock-in effect.

7.1.5 Wavelet analysis

The wavelet transform computes the degree of correlation between a signal and a wavelet, that is a function that has compact support and presents an oscillatory behaviour. By shifting a "mother wavelet" through the time domain and changing its shape factor (which relates to the frequency it "measures"), it is possible to map a time-dependent function to the degree it correlates with a certain frequency at any given time. This way, it is possible to find the frequency content of the signal at any moment in the signal.

The wavelet transforms of the static case, 200 Hz, 350 Hz and 400 Hz are computed from pressure time series monitored with a probe located at $x/c = 1.1$ ($0.1\,c$ downstream the trailing edge).

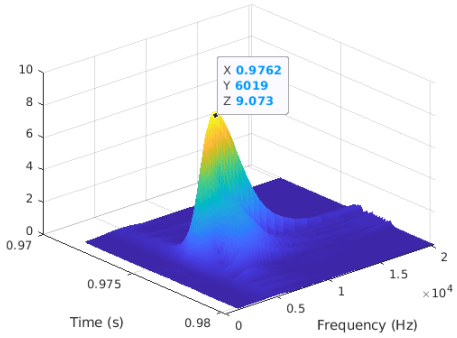

(a) Wavelet transform of pressure forces at $x/c = 1.1$ (static case)

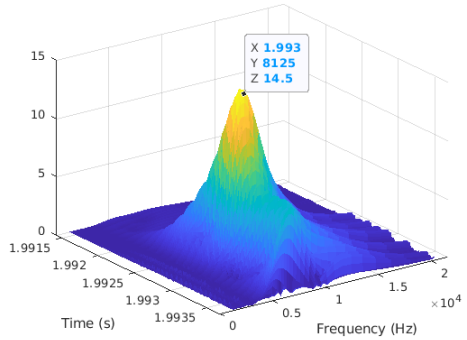

(b) Wavelet transform of pressure forces at $x/c = 1.1$ (350 Hz)

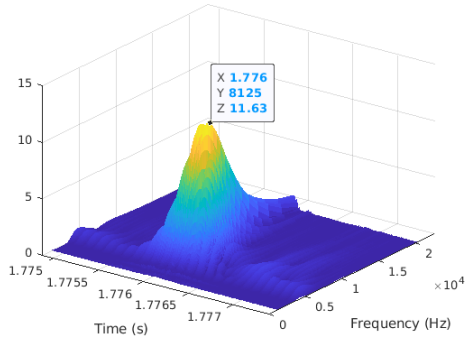

(c) Wavelet transform of pressure forces at $x/c = 1.1$ (200 Hz)

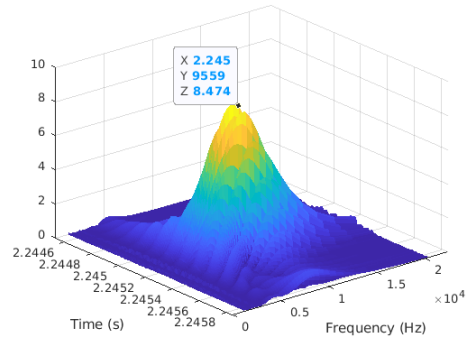

(d) Wavelet transform of pressure forces at $x/c = 1.1$ (400 Hz)

Figure 7.9: Wavelet Transform of pressure signals for static case and $f_{ac} =$ 200 Hz, 350 Hz and 400 Hz

7.2 Focus on the two optimal regions

As is discussed in section section 7.1, several studies have been carried out to find the optimal morphing frequencies, that is actuation frequencies that manage to reduce drag or improve lift. Two optimal regions have been identified as they provide values of the lift to drag ratio that are more impor-

tant than other actuation frequencies. These two cases are located about $f_{ac} \approx 350$ Hz and $f_{ac} \approx 700$ Hz. We will explore frequency ranges around these two optimal cases: 350 Hz and 700 Hz.

A study on frequencies ranging from 720 Hz to 750 Hz is initially performed, namely 710 Hz, 720 Hz, 730 Hz and 750 Hz. We will then focus on a range between 350 Hz and 400 Hz with the following actuation frequencies: 365 Hz, 380 Hz and 390 Hz.

7.2.1 Probe location

In order to carry out local time-frequency and spectral analysis, the following probes were placed in the computational domain at various locations inside the wake and along the suction side of the airfoil (see fig. 7.10). This allows to monitor and analyze the unsteady and frequential behavior of the flow at certain points of interest and figure out the corresponding phenomena through data visualization.

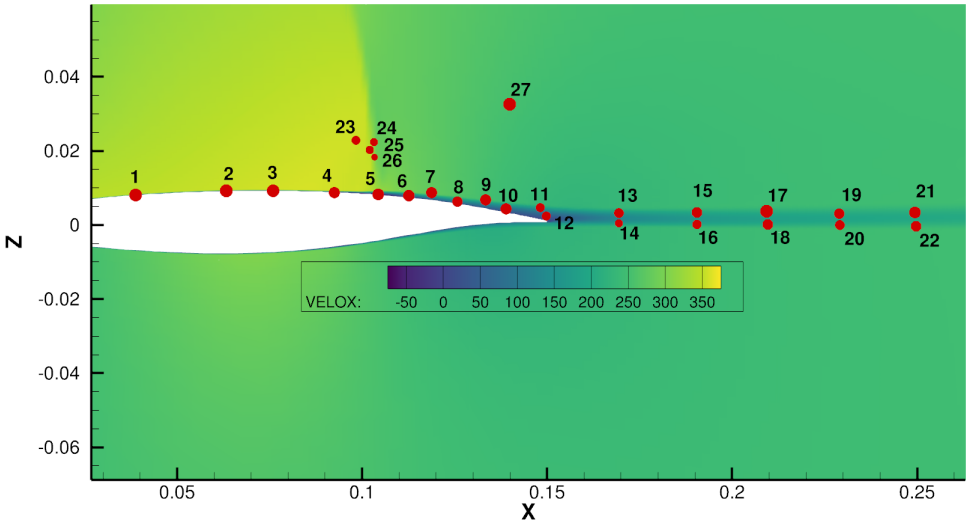

Figure 7.10: Position of the probes around the wing (red circles) on top of a longitudinal velocity iso-contour map

7.2.1.1 Actuation frequencies around 720Hz

We propose here an aerodynamic performance study for morphing frequencies around 720Hz, the latter being assumed as an optimal case according as was found in the previous part. Three different vibration frequencies have been chosen: 710 Hz, 730 Hz and 750 Hz, the results of which are compared to 720 Hz as well as a vibration-free case (static case).

7.2.1.2 Performance analysis

The aerodynamic performance of each frequency in relation to the static case is computed and a short sample of the time series is represented in figures 7.11 and 7.12.

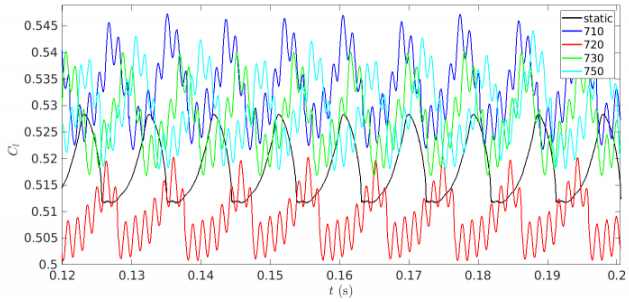

Figure 7.11: Time series of the lift coefficient for f_{ac} = 710 Hz, 720 Hz, 730 Hz, 750 Hz and the static case.

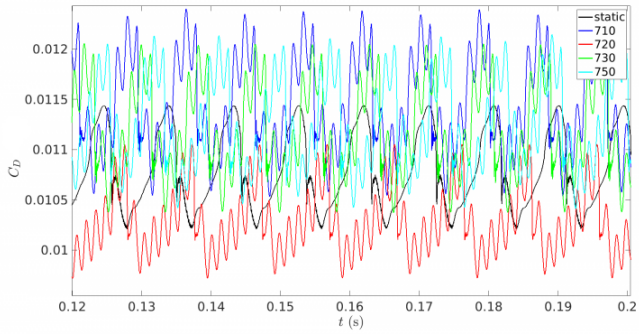

Figure 7.12: Time series of the drag coefficient for f_{ac} = 710 Hz, 720 Hz, 730 Hz, 750 Hz and the static case.

In order to assess the aerodynamic performance of each actuation frequency compared to the static case, the relative change of lift/drag/lift to drag with respect to the static configuration is computed with a simple Matlab script. The newly computed variable is then multiplied by 100 so as to be expressed as a percentage of variation in regard to the static case:

Frequency (Hz)	710	720	730	750
$100 \times \frac{\langle C_l \rangle - \langle C_l \rangle_{\text{static}}}{\langle C_l \rangle_{\text{static}}}$	2.96%	-1.84%	1.79%	2.14%
$100 \times \frac{\langle C_d \rangle - \langle C_d \rangle_{\text{static}}}{\langle C_d \rangle_{\text{static}}}$	6.21%	-4.48%	3.84%	4.32%
$100 \times \frac{\langle C_l/C_d \rangle - \langle C_l/C_d \rangle_{\text{static}}}{\langle C_l/C_d \rangle_{\text{static}}}$	-3.11%	2.77	-1.97%	-2.09%

Table 7.4: Relative change (percentage) of time-averaged force coefficients with respect to the static case for actuation frequencies ≤ 450 Hz. A positive (resp. negative) value means an increase (resp. decrease) in percents of the force coefficient compared to the static case.

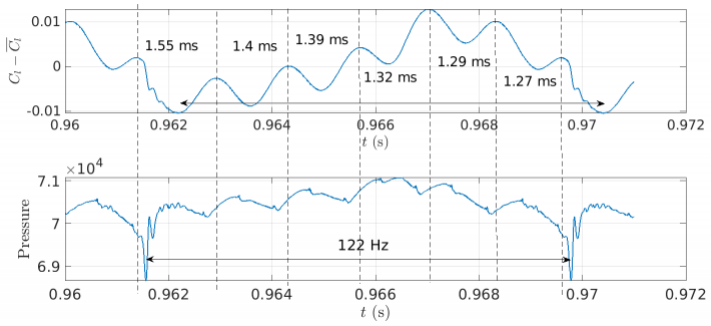

Figure 7.13: Evolution of the lift coefficient (top) and pressure (bottom) as functions of time.

It can be noticed that the actuation frequency 720 Hz is optimal among the others because this is the only frequency that creates a gain of lift to drag ratio and the only to substantially decrease drag (by nearly 4.5%). On the other hand, the slight lift reduction (-1.8%) does not significantly impact the performance improvement brought by diminishing drag, in contrast to the other frequencies.

After identifying the frequency of buffet and the frequency of actuation. We would like to identify the effects of morphing on the force time series, such as the lift coefficient which will be studied because the unsteadiness of lift is generally more pronounced. First, the unsteady behaviour of the signals is visualized over a short time duration which would correspond to a buffet period.

Figure 7.13 shows the variation of the lift coefficient over a period of buffet which corresponds to the lowest frequency mode (122 Hz). This time series is juxtaposed with a pressure signal recorded by a monitor probe placed right above the trailing edge over the same time period. The second plot shows two minima (downward peaks). The interval that separates these two minimum values corresponds to a buffet period, because pressure variations that are recorded inside the separated shear layer are directly correlated to the motion of the shock through the SWBLI. It has been observed that such a strong pressure variation accompanies the destabilization of the detached shear layer over the suction side of the airfoil, which in turn triggers the destabilization of the wake.

The 122 Hz frequency value — which corresponds to the buffet mode — is found in the time series of the lift coefficient. It is expected that a maximum of the lift coefficient would correspond to a minimum of pressure over the suction side of the airfoil. This is true to a certain extent : a small phase shift can be found between the local maxima of lift and minima of pressure. This means that the fluid does not compress instantly and a buffer duration delays the appearance of the pressure fluctuation over the airfoil.

This strong variation in pressure comes from a change in the position of the trailing edge due to morphing:

- When the trailing edge is deflected downwards during half an actuation period, there exists a minimum of pressure.

- When the trailing edge is deflected upwards, this results in a maximum of pressure.

A power spectral density is now computed from the lift coefficient time series over a long duration:

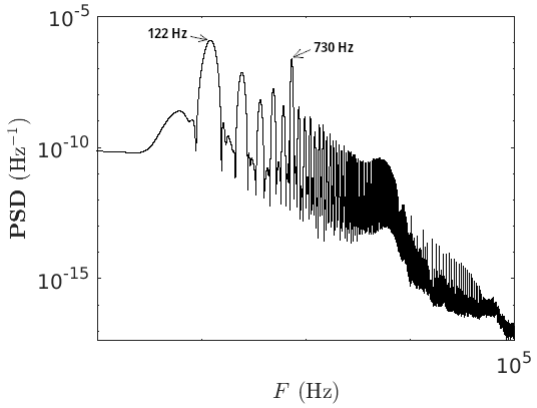

Figure 7.14: PSD transformation for the signal of the lift coefficient for the frequency 730 Hz.

As can be seen in figure 7.14, the prominence of both the buffet mode (122 Hz) and the actuation mode located at the 730 Hz frequency mark is highlighted: These two modes are the most energetic in the lift time series while most of the other peaks are harmonics of either of these modes. By decomposing the lift signal into small intervals corresponding to intervals between two consecutive maximum values (fig. 7.27 or 7.28 for instance), supposedly due to morphing, it is expected that each of these intervals is a constant duration equalling a period of $1/730 \approx 1.37$ ms. Yet it is noticed that each of the intervals do not last exactly 1.37 ms but the duration fluctuates around this value so that by summing all these durations and dividing by 6 — the number of intervals, the average time period is equal to $1/730$. It appears that this fluctuating time interval between two consecutive peaks of the lift coefficient is caused by a changing shock position and velocity: In one buffet period, the shock moves back and forth and back to its initial position. When superimposing a trailing edge motion on top of the naturally occurring instability, the observed lag or interval shortening could coincide with the fact that the information that is carried by a pressure disturbance does not take the same time to travel within the boundary layer depending on whether the shock travels forward or backward .

7.2.2 Spectral analysis and time-frequency analysis of a buffet period for different actuation frequencies

7.2.2.1 Spectral analysis

The Power Spectral Density diagrams of the pressure signals extracted from monitor probes located inside the wake or above the trailing edge are hereby plotted: PSD diagrams are computed from pressure time series taken at probe n° 12 (see fig. 7.10) for actuation frequencies f_{ac} = 710 Hz, 720 Hz, 730 Hz, 750 Hz.

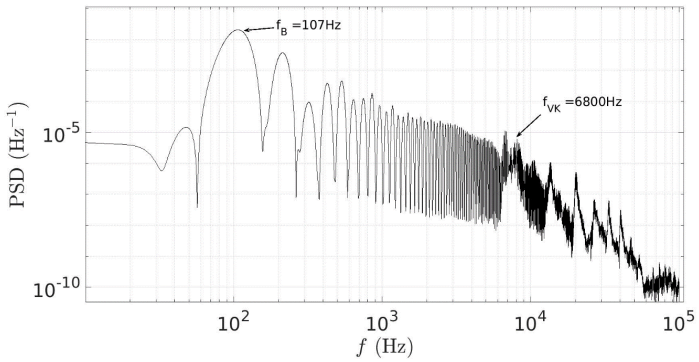

Figure 7.15: PSD diagram of the pressure signal at the trailing edge (probe 12) for the static case.

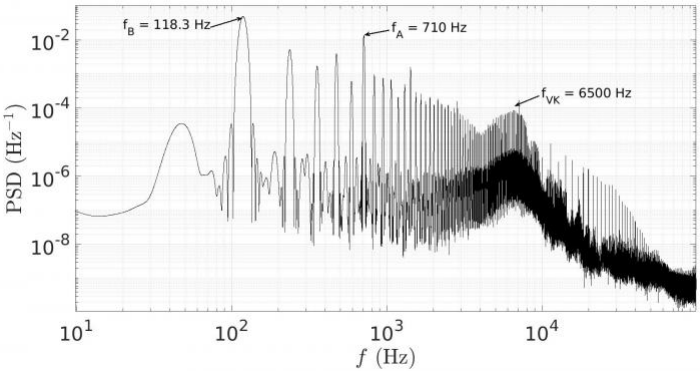

Figure 7.16: PSD diagram of the pressure at the trailing edge (probe 12) for a 710 Hz actuation frequency.

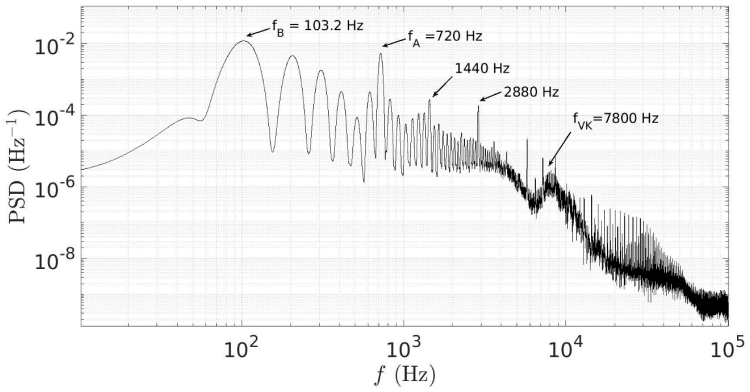

Figure 7.17: PSD diagram of the pressure at the trailing edge (probe 12) for an actuation frequency of 720 Hz.

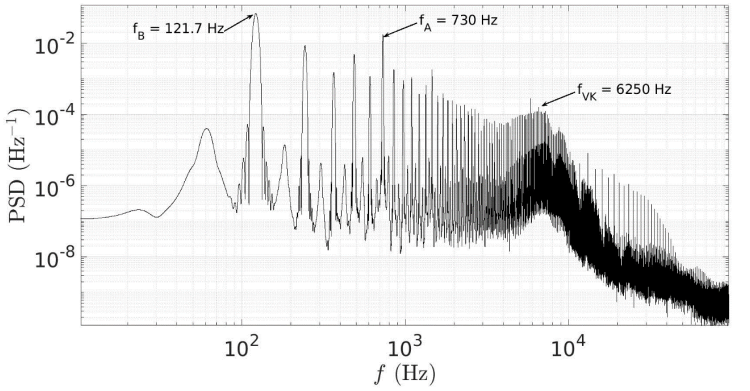

Figure 7.18: PSD diagram of the pressure at the trailing edge (probe 12) for a 730 Hz actuation frequency.

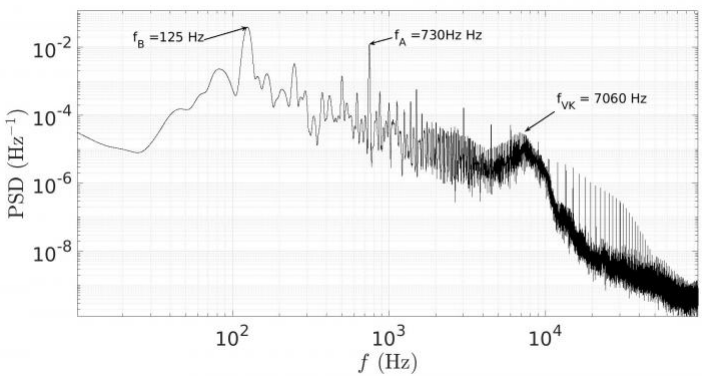

Figure 7.19: PSD diagram of the pressure at the trailing edge (probe 12) for an actuation frequency of 750 Hz.

There are two main peaks for morphing cases which respectively correspond to the buffet frequency (or fundamental) f_0 and its fifth harmonic f_5 for $f_{ac} = 710$ Hz, 730 Hz or 750 Hz, and the sixth harmonic for $f_{ac} = 720$ Hz:

- $f_{ac} = 710$ Hz: $f_0 = 118.3$ Hz and $f_5 = 710$ Hz.
- $f_{ac} = 720$ Hz: $f_0 = 103.2$ Hz and $f_6 = 720$ Hz.
- $f_{ac} = 730$ Hz: $f_0 = 121$ Hz and $f_5 = 730$ Hz.
- $f_{ac} = 750$ Hz: $f_0 = 125$ Hz and $f_5 = 750$ Hz.

For the static case, the most powerful mode is the buffet mode and its harmonics have a decreasing power, as expected. It is worthwhile noting that the buffet frequency f_0 is 7 times smaller than the actuation frequency for $f_{ac} = 720$ Hz, against 6 times for the other cases. This results in a lower buffet frequency f_0 for the 720 Hz case compared to the other morphing configurations, and even a lower frequency than the natural frequency of buffet (static case).

It seems that morphing acts as a forcing mechanism for the transonic buffet instability. Not only does buffet synchronize with the actuation frequency in some cases, but in some others the buffet frequency becomes a

sub-harmonic of the actuation frequency so long as it remains "close" to the natural frequency of the non-actuated case at a given angle of incidence and Mach number.

In order to verify that the previous frequencies f_0 are indeed those of buffet and that they correspond to the time interval separated by two minimum peaks of pressure as shown in figs. 7.20, 7.21 and 7.22), the pressure time series for the static case, $f_{ac} = 720$ Hz and 730 Hz are compared:

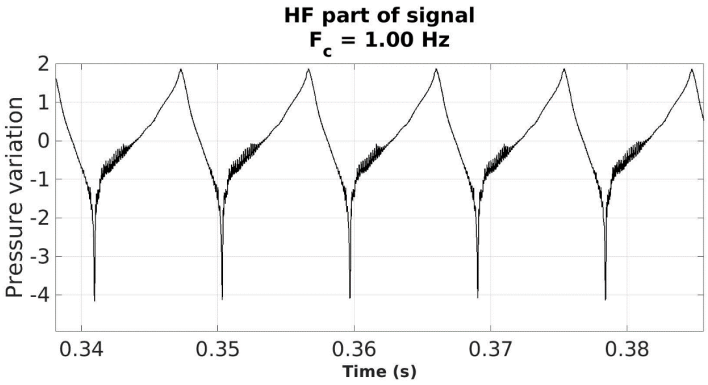

Figure 7.20: Signal of the pressure variation as a function of time at the trailing edge (probe 12) for the static case.

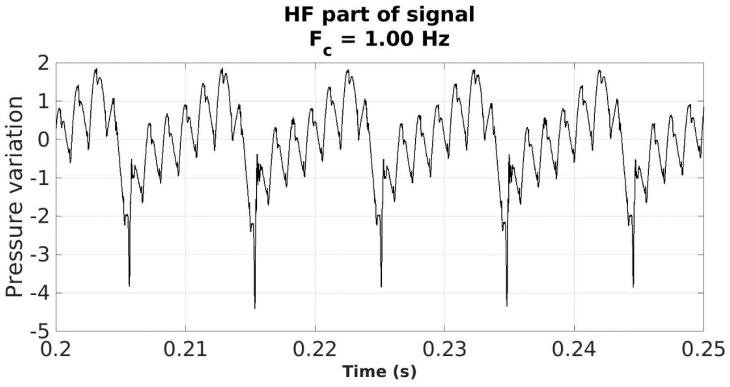

Figure 7.21: Signal of the pressure variation as a function of time at the trailing edge (probe 12) for a morphing frequency of 720Hz.

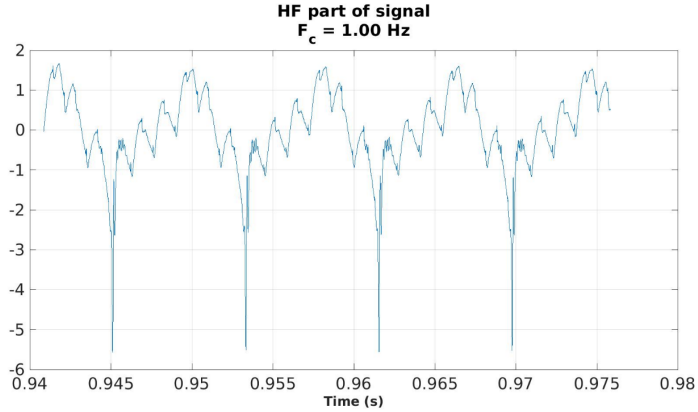

Figure 7.22: Signal of the pressure variation as a function of time at the trailing edge (probe 12) for a morphing frequency of 730Hz.

On the three pressure signals, the repetition of a pattern initiated by a large downward peak can be observed. These peaks correspond to the release of a rapid succession of vortices, or burst, which takes place when the shock reaches its maximum velocity during a buffet cycle. The frequency of this phenomenon is assessed by calculating the wavelet transform of a section of the signal between the two peaks, which supposedly corresponds to a buffet period (figs. 7.20 to 7.22).

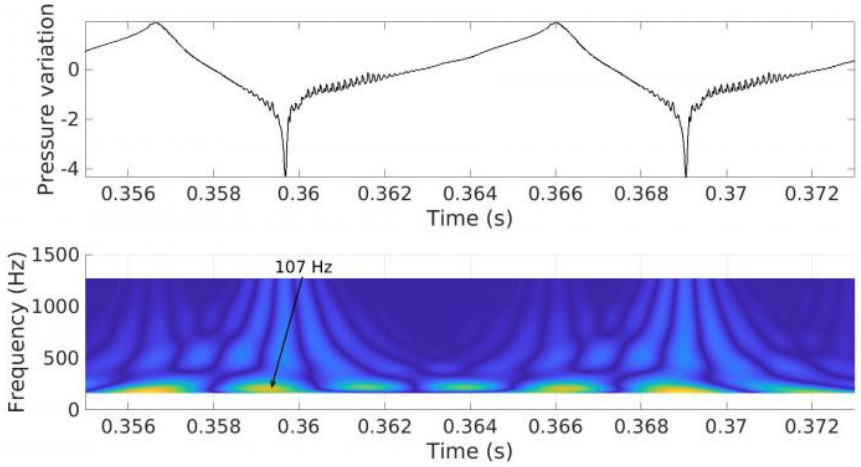

Figure 7.23: Wavelet analysis of the pressure signal for the static case just above the trailing edge (probe 12).

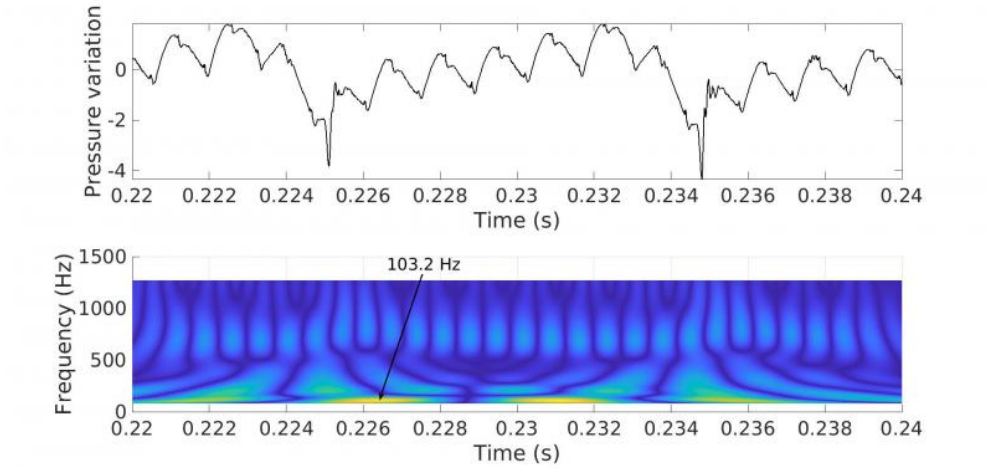

Figure 7.24: Wavelet analysis of the pressure signal for an actuation frequency of 720 Hz just above the trailing edge (probe 12).

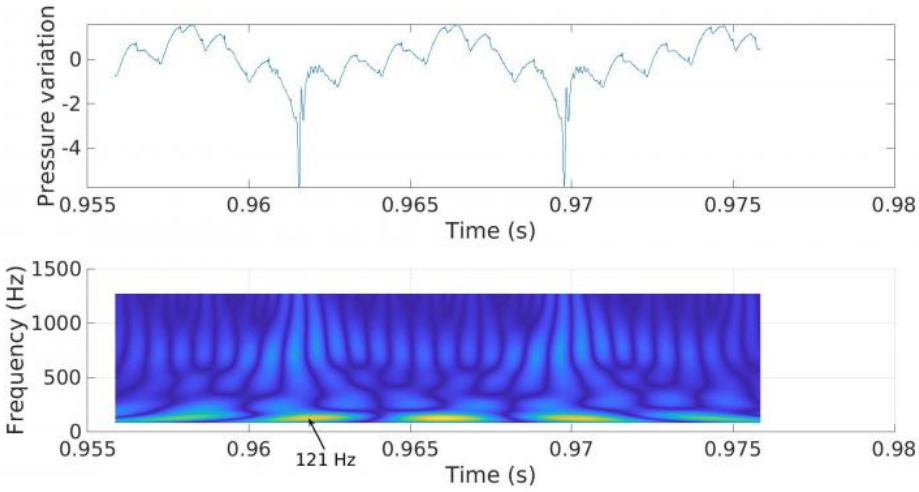

Figure 7.25: Wavelet analysis of the pressure signal for a frequency of 730 Hz just above the trailing edge (probe 12).

We indeed find, through this wavelet analysis, the frequencies previously identified on the PSD diagram, namely 107 Hz, 103.2 Hz and 121 Hz, corresponding to the natural frequency of buffet (static case), morphing at 720

Hz and 730 Hz respectively. This leaves no doubt that these frequencies do correspond to the buffet mode.

In brief, it has been observed that in some instances, the choice of the actuation frequency shifts the natural frequency of the buffet mode towards a sub-harmonic of said actuation frequency. Considering that buffet is generally avoided as the instability could resonate with a structural mode of the airframe, morphing offers a way to control the frequency at which buffet occurs through a lock-in effect. Synchronization can either be direct or the buffet mode is synchronized with a sub-harmonic of the actuation frequency, depending on the value of said frequency.

7.2.2.2 Local study of the morphing-flow interaction

In this part, a local analysis of the impact of morphing on the pressure time series is performed. A buffet period is first targeted. The flow is then visualized in that time-span, and a time-frequency study is also carried out over the same time interval. This analysis is done for the static configuration and morphing actuation at 720 Hz and 730 Hz (the 710Hz and 750Hz cases being analogous to 730Hz). Figures 7.23 to 7.25 show the pressure time series near the trailing edge (probe n°12) for each configuration and over a single buffet period.

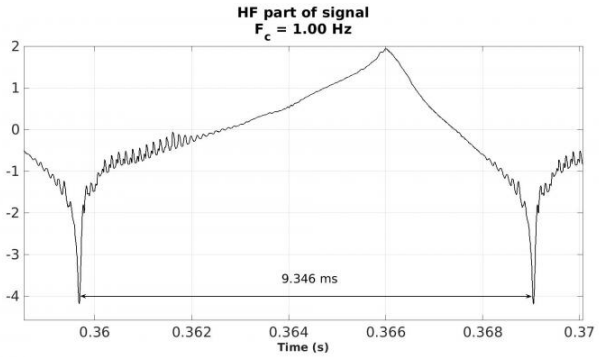

Figure 7.26: Pressure time series (for pressure time series, the left axis is a measure of pressure in Pascals relative to the time-averaged pressure level) for a single buffet period near the trailing edge (probe 12) for the static case.

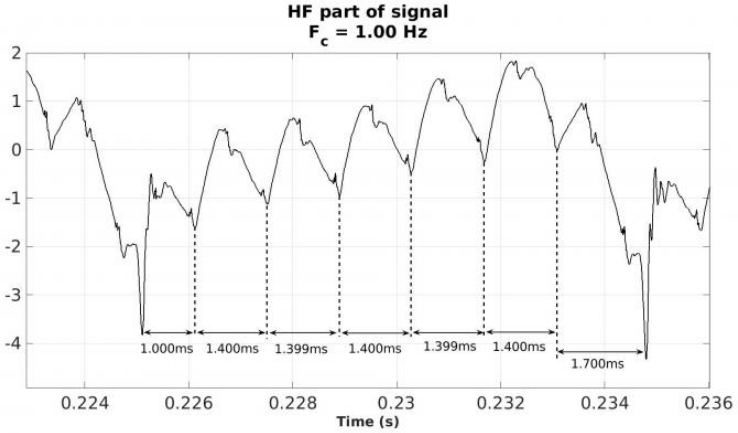

Figure 7.27: Pressure time series for a single buffet period at the trailing edge (probe 12) for a morphing frequency of 720 Hz.

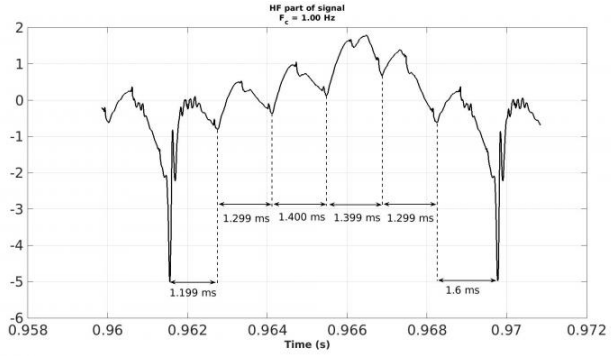

Figure 7.28: Pressure time series for a single buffet period at the trailing edge (probe 12) for a morphing frequency of 730 Hz.

As was already found in the previous part, the overall trend characterized by a global increase then decrease of pressure, punctuated by two brutal peaks can be observed in figures 7.26 to 7.28. It is also acknowledged that the time interval between two local minima is not constant, as presented in figures 7.27 and 7.28. However, the average time interval is found to be the same as the actuation frequency, which becomes obvious by plotting a wavelet transform (fig. 7.29). This time, the signal is filtered so as to remove the low-frequency content. With $F_c = 1$ Hz, all frequencies lower than 1 Hz — slowly evolving trends that last more than a second — are filtered out. This

allows to restrict the frequency domain and benefit from a better contrast when plotting the intensity of the wavelet transform.

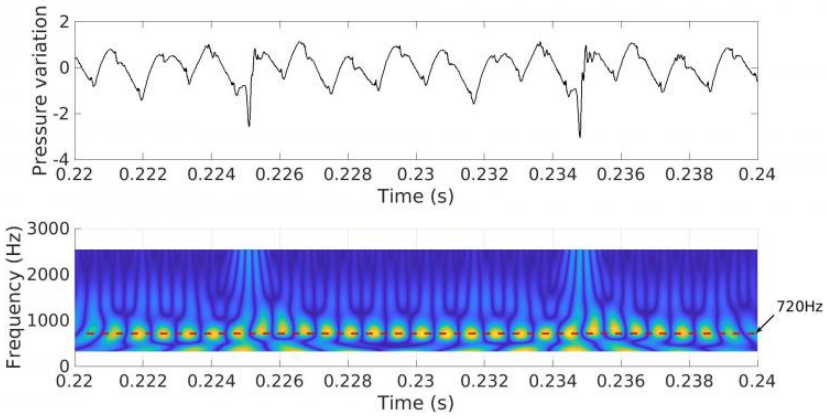

Figure 7.29: Wavelet analysis of the pressure signal captured above the trailing edge (probe 12), $F_c = 1$ Hz.

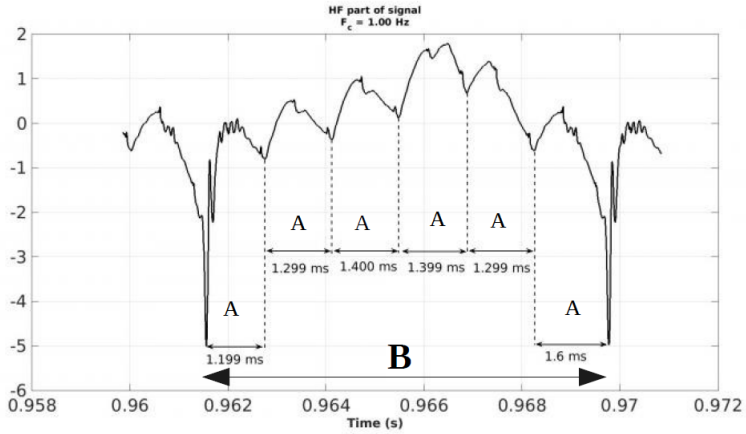

Figure 7.30: Breakdown of the pressure signal for an actuation frequency of 730 Hz just above the trailing edge (probe 12), $F_c = 1$ Hz.

More specifically, it is noticed that the periods of each small pattern A, which stands for "actuation" (fig. 7.30) appear to follow the overall trend of

pressure, and therefore it can be said that the time period of each pattern A depends on the position of the shock. Indeed, during a buffet cycle B, the period of the pattern increases with the pressure, then tends to decrease. However, we note that when vortices are shed, the time interval increases again and reaches a maximum (1.6 ms for $f_{ac} = 730$ Hz). The 720 Hz case has an additional period compared to the 710 Hz, 730 Hz and 750 Hz cases.

7.2.2.3 Study of the large vortical release

In this section, the mechanism that governs the sudden burst is explored to explain the onset of vortex shedding after pressure reaches a minimum over the trailing edge (circled in fig. 7.23 to 7.25). It has been found that the separated shear layer over the suction side of the airfoil destabilizes periodically during each buffet period. Our visualizations, both for an angle of incidence of 1.8° and 5° have shown that this destabilization occurs when the shock is moving upstream towards the leading edge. This is succinctly described in the following schematic from Hartmann, Feldhusen, and Schröder, 2013:

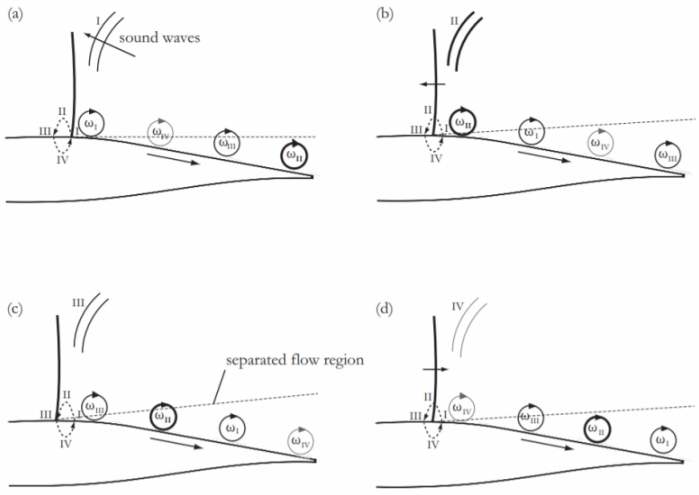

Figure 7.31: Schematics from Hartmann, Feldhusen, and Schröder, 2013 showing the flow behaviour during one buffet oscillation cycle. (a) Position I: the shock is in its most downstream position (b) Position II: the shock moves upstream and reaches its maximum velocity (c) Position III: the shock is in its most upstream position (d) Position IV: the shock moves back downstream at maximum velocity.

In figures 7.31 (a), (b), (c) and (d), the dotted ellipse at the shock foot schematizes the relative velocity of the shock with respect to the airflow. In its extremal positions I and III, the shock is immobile relative to the wing, but its lowest velocity and highest velocity relative to the airflow are reached in positions IV and II respectively: As the shock travels downstream, its velocity points in the same direction as the airflow hence the flow travels at a lower velocity relative to the shock, and the opposite applies when the shock travels upstream.

This relative velocity governs the intensity of the shearing forces at the shock foot. When the shock travels upstream, the resulting shearing strongly destabilizes the shear layer which causes an intense vortex (the circulation of which is denoted ω_{II}) to form near the shock foot, materialized by the thick circle that appears near the shock in figure 7.31 (b). The shock then decelerates. This decreases the shearing intensity, and therefore the destabilization strength.

It was found in our computations that the intense peaks observed in the pressure signals (figures 7.23 to 7.25) do not correspond to an extremal shock position, but instead coincide with the moment when the shock travels upstream and reaches its maximum velocity relative to the flow.

One can identify a large vortical release which translates as a disturbance in the Q-criterion field — cf. figure 7.41. This release corresponds to the large pressure variation observed during a buffet period. Comparing graphs 7.23, 7.24 and 7.25 to the evolution of the shock position, one observes that the shock brutally rushes upstream at the moment of the vortical release, but that it then continues to travel upstream more slowly afterwards.

More specifically, it is found that the shock reaches its maximum upstream position around a time $t = 0.9628$ s, before setting off again downstream. Looking at the location of the trailing edge at this instant, it is clear that it reaches its lowest position (within an actuation cycle) corresponding to the first local pressure minimum after the large vortex release, here marked by the dotted vertical line at $t = 0.9628$ s in fig. 7.32. Hence to clearly depict when vortices are shed during the buffet cycle, the pseudo-periodic pressure time series at probe 12 can be broken down into different instants: For an actuation frequency of 730 Hz for instance, it is shown in figure 7.32 that pressure on top of the trailing edge increases as the trailing edge moves upwards and decreases whenever it moves downwards.

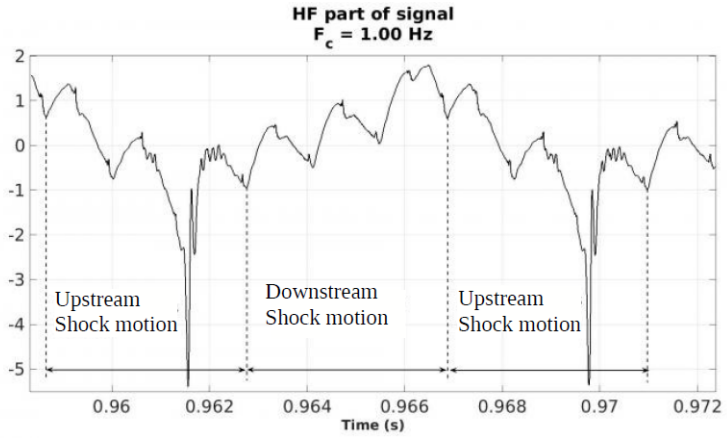

Figure 7.32: Signal of the pressure variation for a buffet period abov the trailing edge (probe 12) for a morphing frequency of 730 Hz.

It has been observed that as the shock moves upstream, a trailing edge downward motion (here at $t = 0.9617$ s for example) when the shock is close to reaching its most upstream position is enough to cause vortical release. The shock then moves downstream, coinciding with an upward trend in curves 7.26, 7.27 or 7.28.

At 710 Hz, 730 Hz and 750 Hz, the buffet cycle is forced such that one buffet period contains 6 actuation periods of the trailing edge. This results in a symmetrical split of the buffet period into a forward and backward motion that contain the same number of actuations: 6 being an even number, the buffet period is split into two parts of three actuation periods each (cf. fig. 7.30).

In contrast to the previous actuation frequencies, the buffet period is decomposed into 7 actuation periods in the case of a 720 Hz actuation frequency (fig. 7.27). It is found that there is an imbalance between the respective duration of the upstream motion and the downstream motion.

More studies would be required to investigate a potential control of the shock speed throughout its motion by acting on wake and shear layer instabilities.

Spectral analysis of the wake

This part will be devoted to the study of signals and phenomena observed in the wake. To perform the analysis, a focus is made on the probes located between positions 13 and 22.

First, we conduct a study far aft the trailing edge, by monitoring pressure data at probe 22. Then a frequency analysis is performed by computing the PSD diagrams from the pressure signal for the static case and actuation frequencies 710 Hz, 730 Hz, and 750 Hz (figures 7.33 to 7.37).

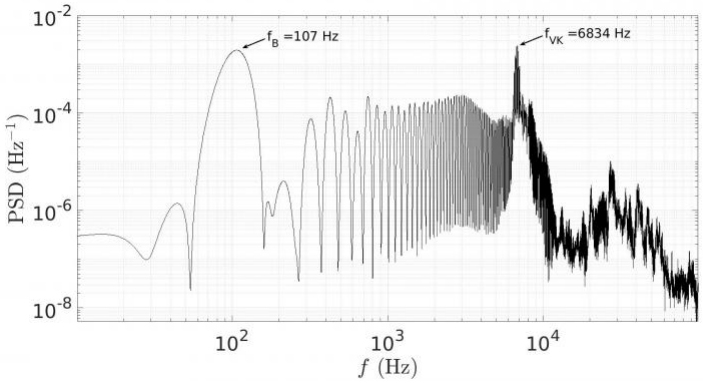

Figure 7.33: PSD diagram of the pressure time series captured at probe 22 for the static case.

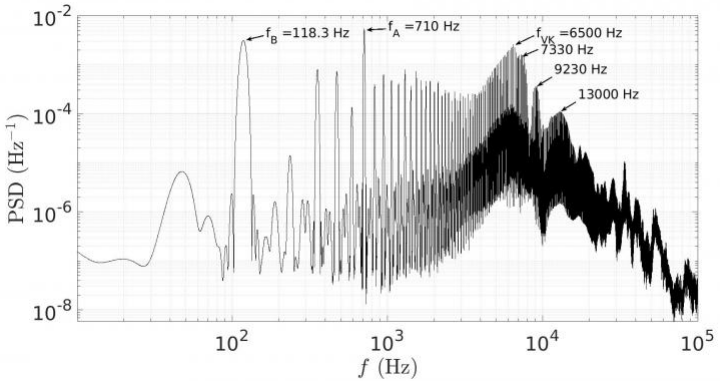

Figure 7.34: PSD diagram of the pressure time series captured at probe 22 for an actuation frequency of 710 Hz.

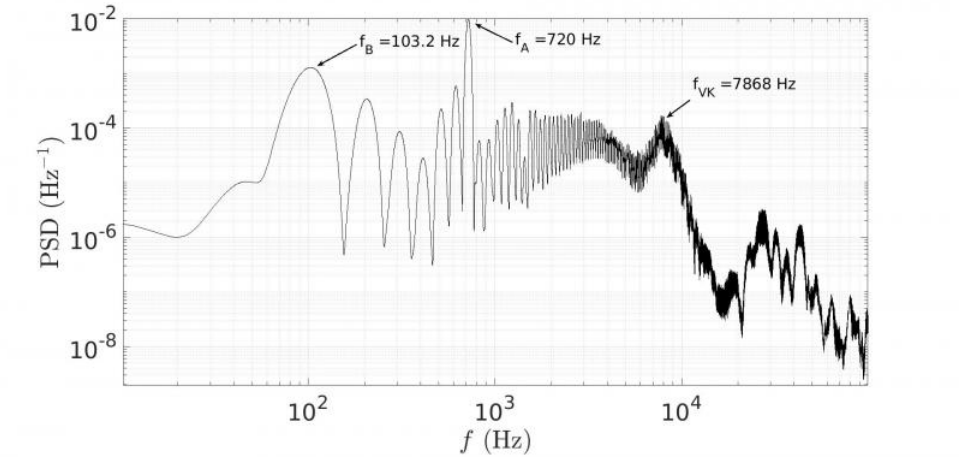

Figure 7.35: PSD diagram of the pressure time series captured at probe 22 for an actuation frequency of 720 Hz.

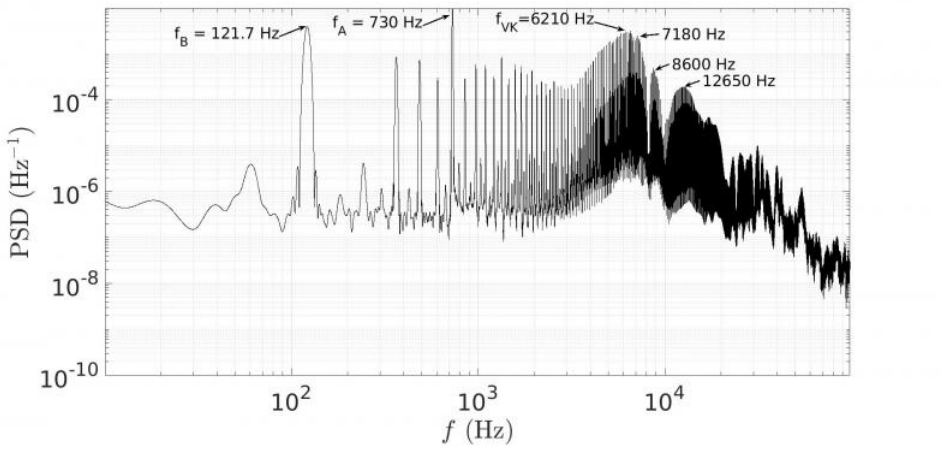

Figure 7.36: PSD diagram of the pressure time series captured at probe 22 for an actuation frequency of 730 Hz.

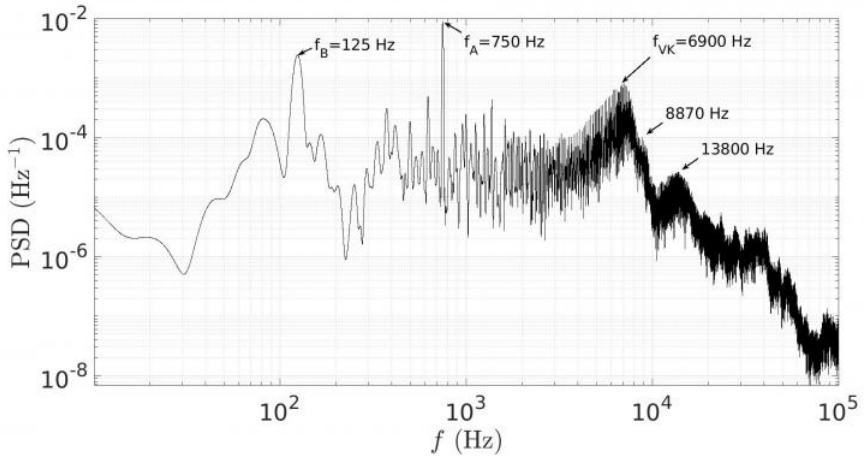

Figure 7.37: PSD diagram of the pressure time series captured at probe 22 for an actuation frequency of 750 Hz.

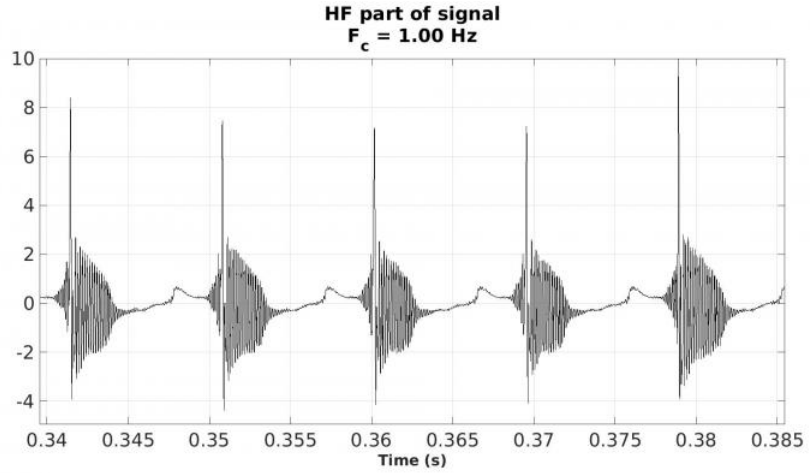

Figure 7.38: Signal of the pressure variation as a function of time in the wake (probe 22) for the static case.

The buffet mode, which was extensively studied in the previous part, is still identified as being the first spectral bump associated to a high energy. The frequency values are consistent with the pressure measurements performed close to the trailing edge.

To understand the phenomena corresponding to higher frequencies, the pressure signals of the static cases, 720 Hz and 730 Hz (710 Hz and 750 Hz being similar to 730 Hz) are plotted at probe 22 (figures 7.38 to 7.40). The Q-criterion is drawn in an attempt to visualise coherent vortices. Indeed, the

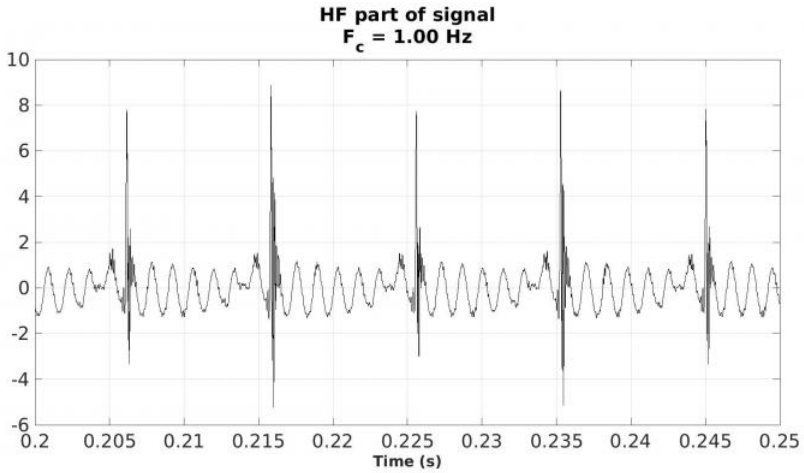

Figure 7.39: Time series of the pressure variation as a function of time in the wake (probe 22) for a morphing frequency of 720 Hz.

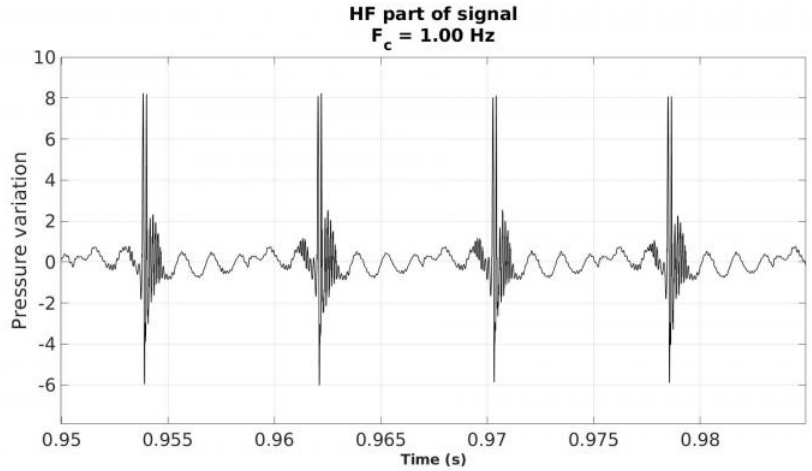

Figure 7.40: Time series of the pressure variation as a function of time in the wake (probe 22) for a morphing frequency of 730 Hz.

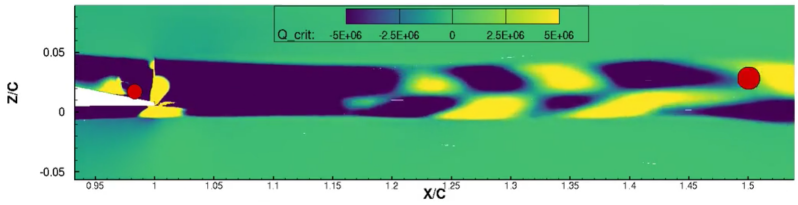

Figure 7.41: Contour criterion Q concentrated on the trailing edge and in the wake.

Q-criterion, defined by $Q = \frac{1}{2}(||\Omega||^2 - ||S||^2) > 0$ where $\Omega = \frac{1}{2}\left(\partial_j u_i - \partial_i u_j\right)$ is the rotation rate tensor and $S = \frac{1}{2}\left(\partial_j u_i + \partial_i u_j\right)$ is the strain rate tensor, compares the amount of vorticity relative to the amount of strain rate within the flow, ruling that a vortex is a zone where vorticity – or the tendency of a patch of fluid to rotate – is more important than shear strain. This improves the detection of vortices as they are generally difficult to observe because of their important advection velocity in the transonic regime.

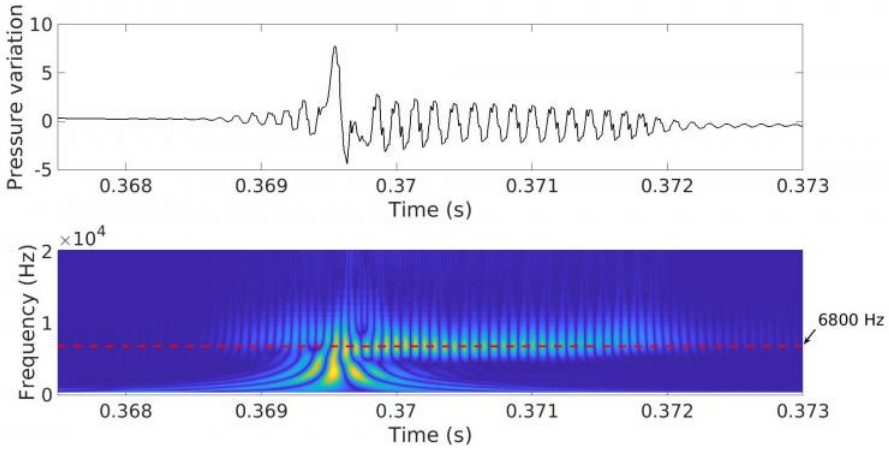

Figure 7.42: Wavelet transform of the pressure signal in the wake (probe 22) for the static case, $F_c = 5000$ Hz.

We observe on these signals the presence of a cycle containing a large disturbance in each period. This disturbance corresponds to the release of a strong vortex coming from the destabilization of the boundary layer, quickly

followed by a succession of smaller, less powerful coherent eddies. The first vortex comes from an upstream shock motion, which can be observed in both the static case or through a forcing of the buffet mode by employing trailing edge morphing (see part "Study of the large vortical release"). In any case, the pressure time series far downstream in the wake invariably records the appearance of an abrupt variation followed by regularly spaced pressure disturbances. A wavelet transform of the previous signals (cf. fig. 7.42, 7.43 and 7.44) is plotted to help identify the frequency of said disturbances (Figures 7.38 to 7.40). Because the frequencies involved are much higher than 5000 Hz, it has been chosen to filter out frequencies lower than $F_c = 5000$ Hz to focus the view on higher frequency modes.

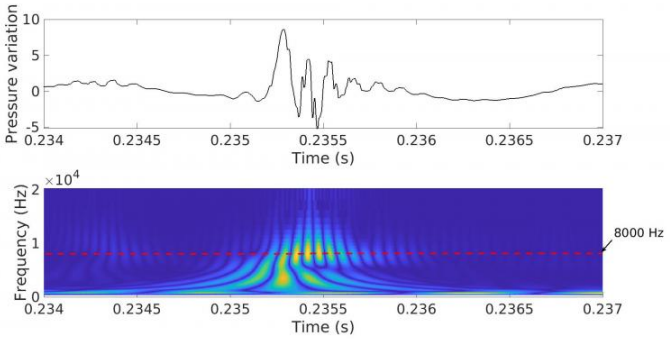

Figure 7.43: Wavelet transform of the pressure signal in the wake (probe 22) for a morphing frequency of 720 Hz, $F_c = 5000$ Hz.

There exists a strong correlation (yellow color) around 6500 Hz and 7000 Hz coinciding with the strong disturbance appearing between 0.962 s and 0.9625 s for $f_{ac} = 730$ Hz, as can be seen in figures 7.42, 7.43 and 7.44. By comparing these numerical results with the Q-criterion visualizations, it is possible to deduce that this frequency range corresponds to the von Kármán vortices that develop from a destabilization of the wake. We observe a phenomenon analogous to the 730 Hz case for morphing frequencies 710 Hz and 750 Hz.

It can be remarked in figure 7.43 that the time series of the pressure signal for an actuation frequency of 720 Hz is distinct from the other cases. Indeed, the burst does not last as long as is the case for other actuation frequencies or even for the static configuration (figs. 7.38 to 7.40 and figs. 7.42 to 7.44).

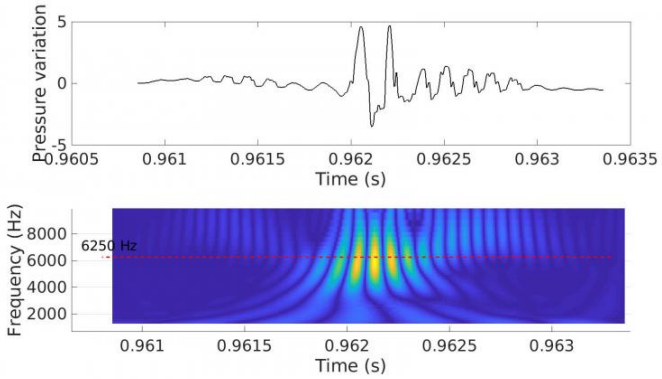

Figure 7.44: Wavelet transform of the pressure signal in the wake (probe 22) for a morphing frequency of 730 Hz, $F_c = 5000$ Hz.

It would seem that the von Kármán instabilities are suppressed more for an actuation frequency of 720 Hz as for other vibration frequencies.

Using the PSD diagrams presented at the beginning of the section, a sharp peak can be observed around the respective frequency of 9200 Hz and 8600 Hz for the cases of morphing at 710 Hz and 730 Hz. For the other actuation frequencies, this peak is much less marked.

7.2.3 Partial conclusion

The actuation frequencies 710 Hz, 730 Hz and 750 Hz did not present any performance improvement compared to the 720 Hz case which was determined to be one of the optimal frequencies in section 7.1.

This character is explained by a reduction in the strength of buffet and weaker vortex shedding resulting from a less pronounced adverse pressure gradient. This indicates once again the strong interdependence between the buffet and vortex shedding.

As a matter of fact, the strength of the SWBLI is governed by the intensity of the shear stresses caused by the adverse pressure gradient generated by a sudden flow compression through the shock. By quickly deforming the trailing edge, a pressure disturbance is locally created near the aft end of the wing. This disturbance compresses or dilates the flow and propagates

along the shear layer, providing a *feedback* to the region of SWBLI. This information thus modifies the behavior of the interaction and the relative velocity of the shock as well as the period of the buffet instability.

7.2.4 Actuation frequencies between 350 Hz and 400 Hz

7.2.4.1 Analysis of the averaged forces

Spectral analysis

We seek to identify the frequency of the buffet mode for the three investigated morphing frequencies. As was done previously for frequencies around 700 Hz, a spectral analysis is carried out by computing the PSD of the lift coefficient for $f_{ac} = 365$ Hz, 380 Hz and 390 Hz.

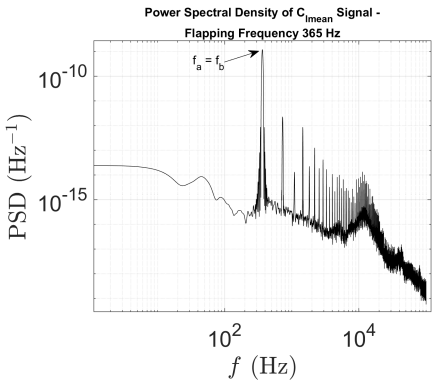

Figure 7.45: PSD graph of the lift coefficient, for a flapping frequency of 365 Hz.

From this spectral analysis of the lift force coefficient (cf. fig. 7.45), it is found that for an actuation frequency of 365 Hz, there is a synchronization between the morphing mode and the buffet mode (the frequency of which is here denoted f_b), such that $f_{ac} = 365$ Hz $= f_b$.

On the other hand, for the 380 Hz and 390 Hz cases, the actuation frequency is, in both configurations, a multiple of the buffet frequency such that:

- If $f_{ac} = 380$ Hz, then $f_{ac} = 3f_b$ where $f_b \approx 127$ Hz
- If $f_{ac} = 390$ Hz, then $f_{ac} = 3f_b$ where $f_b = 130$ Hz

The following figures illustrate this result:

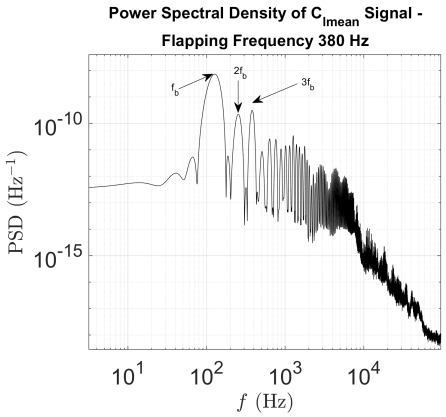

Figure 7.46: PSD graph of the lift coefficient, for a flapping frequency of 380 Hz.

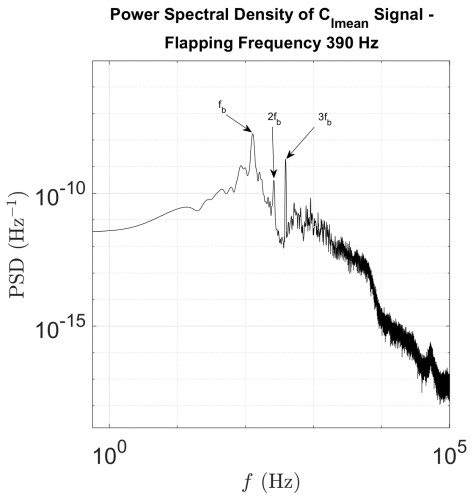

Figure 7.47: PSD graph of the lift coefficient, for a flapping frequency of 390Hz.

As shown in figures 7.45 to 7.47, lock-in does not manifest itself as a perfect synchronization between the actuation frequency and the buffet frequency, but like actuation frequencies in the 700 Hz range, the effect of morphing is to force buffet to take place at a frequency that is a sub-harmonic of the actuation frequency. The only exception to this happens for an actuation frequency of 365 Hz whereby the frequency of the buffet mode happens to perfectly match the frequency of actuation (fig. 7.45). Remarkably, it is observed that the power level corresponding to the buffet mode is approximately 10 times lower for the frequency 365 Hz than for an actuation frequency of 380 Hz or 390 Hz. For the former actuation frequency, the power level associated to lift is generally substantially lower than it is for higher actuation frequencies, and has been observed to be hundreds or thousands of times lower across a wide range of frequencies.

Aerodynamic performance in the vicinity of 350 Hz and 400 Hz

The following figure is a short fragment of the lift coefficient time series for $f_{ac} = 365$ Hz, 380 Hz, 390 Hz and the static case:

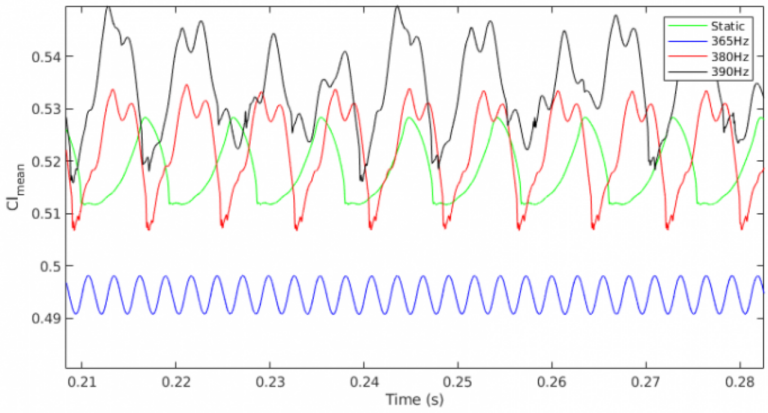

Figure 7.48: Signals of the lift forces for the static case and various actuation frequencies between 350 Hz and 400 Hz.

It is seen in figure 7.48 that lift is reduced in the case of a flapping frequency of 365 Hz, while it increases for an actuation frequency of 390 Hz. The peak to peak amplitude of the lift time series, however, appears to diminish when an actuation frequency of 365 Hz is applied. This coincides

with the previous finding that the power level in the spectra is generally lower for an actuation frequency $f_{ac} = 365$ Hz. Another aspect worthy of attention is the important periodicity of the lift time series for $f_{ac} = 365$ Hz which is not observed for other frequencies or even for the static case. This is also obvious in the power spectrum at fig. 7.45 as the buffet mode is seen to be much stronger than all other modes coherent or chaotic modes of the signal. In the case of an actuation frequency of 365 Hz, morphing seems to act on the whole SWBLI as on a single, coherent system moving in perfect synchronization, so much that the trailing edge motion causes the detached boundary layer to move flatly, as if locked with the shock and the trailing edge motion.

For 380 Hz and 390 Hz, animations have shown that the boundary layer compresses and expands under the effect of the trailing edge actuation, thus causing additional pressure surges and deficits near the trailing edge which in turn propagate back towards the shock and through a complex feedback effect, contribute to accelerate it, forcing its motion and the frequency at which the mode takes place.

The results are gathered and summarized inside the following table:

Frequency (Hz)	350	365	380	390	400
$100 \times \frac{\langle C_l \rangle - \langle C_l \rangle_{\text{static}}}{\langle C_l \rangle_{\text{static}}}$	-	-4.62%	0.82%	2.98%	-
$100 \times \frac{\langle C_d \rangle - \langle C_d \rangle_{\text{static}}}{\langle C_d \rangle_{\text{static}}}$	-	-9.96%	1.12%	5.80%	-
$100 \times \frac{\langle C_l/C_d \rangle - \langle C_l/C_d \rangle_{\text{static}}}{\langle C_l/C_d \rangle_{\text{static}}}$	5.5%	5.92%	-0.29%	-2.66%	-2.5%

Table 7.5: Summary table of aerodynamic performance for actuation frequencies between 350 Hz and 400 Hz. Performance values for the variation of average lift and drag for 350 Hz and 400 Hz can be taken from table 7.1

It is found that morphing performed at 365 Hz is the optimal case in this frequency range given that it achieves the highest relative variation in lift to drag ratio (+ 5.92%) with respect to the static case. Indeed, although lift is diminished, an even greater drag loss is recorded on average (reducing it by 9.96% relative to the static case). The 365 Hz case is not only the most optimal in comparison with 380 Hz and 390 Hz but also when compared to

350 Hz and 400 Hz.

Identification of vortex instabilities

Using the Tecplot visualization software, a graph is plotted in fig. 7.49 to show the position of the two monitor probes mainly used in the present study, namely one that is close to the trailing edge, probe 11 located at around $x/c = 1$, and one taken at the farthest location away from the wing, probe 22 positioned at around $x/c = 1.7$ (fig. 7.49). In particular, the pressure fluctuations near the trailing edge, over the suction side of the airfoil (probe 11) and in the wake (probe 22) are of particular interest as they carry the information of the transport of coherent eddies as well as pressure variations induced by the motion of the trailing edge. Two similar studies are conducted for both the 380 Hz and 365 Hz morphing cases, the aim of which is to help determine whether an even more beneficial actuation frequency exists in this range.

- **The 380 Hz morphing case:**

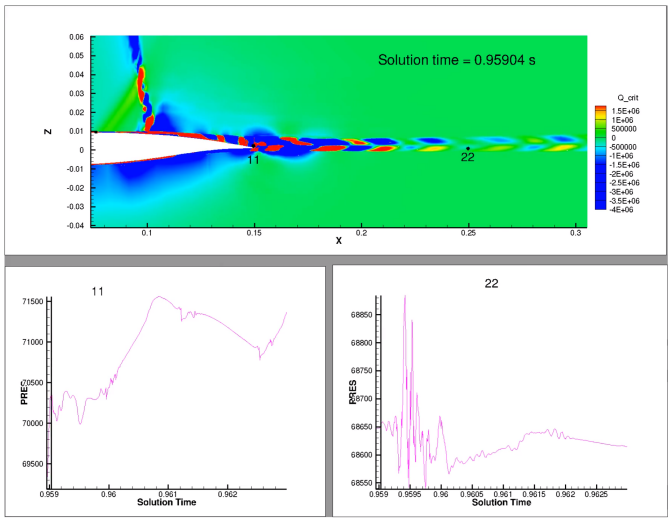

Figure 7.49: Instantaneous snapshot showing morphing at 380 Hz displaying (a) A computed iso-contour of the Q-criterion; (b) The pressure time series recorded by probe 11 over about a buffet period; (c) The pressure time series recorded by probe 22 over about a buffet period.

Figure 7.49 shows a snapshot captured by means of the data visualization software Tecplot, for the an actuation frequency of 380 Hz:

As shown in figure 7.49 (b) which is the pressure signal measured at probe 11, the analyzed signal corresponds to approximately half a buffet period.

Furthermore, we note that a large pressure fluctuation takes place at time $t_b = 0.959$ s on probe n° 11 — which is located on the upper surface and close to the trailing edge. At the same moment, the visualizations show the presence of a vortical burst which advects past probe 11. This is the signature of the von Kármán instability.

To identify this phenomenon, we carried out a spectral study of the pressure signal recorded at probe 11, which allowed us to note how often these instabilities take place.

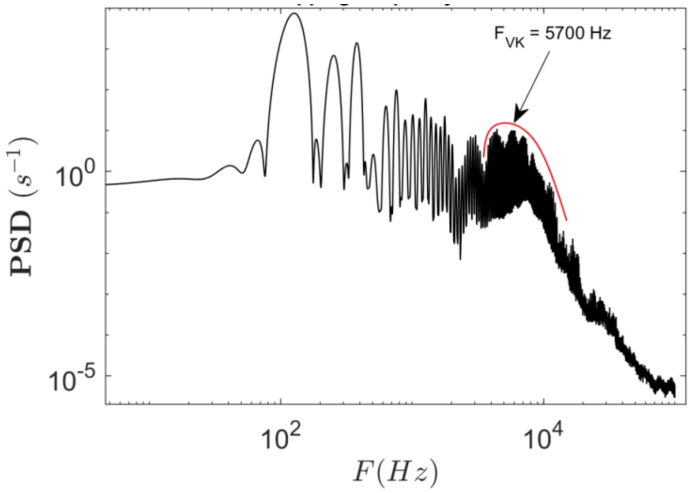

Figure 7.50: PSD diagram of the pressure signal at the upper surface (probe 11), for a 380Hz morphing actuation frequency.

From the PSD diagram in figure 7.50, it is determined that the frequency of the von Kármán vortices is associated to the energetic bump around 5700 Hz.

A wavelet analysis on the pressure signal at probe 11 is then shown in figure 7.51. A burst appears to happen slightly before $t_b = 0.959$ s, as indicated in the same figure:

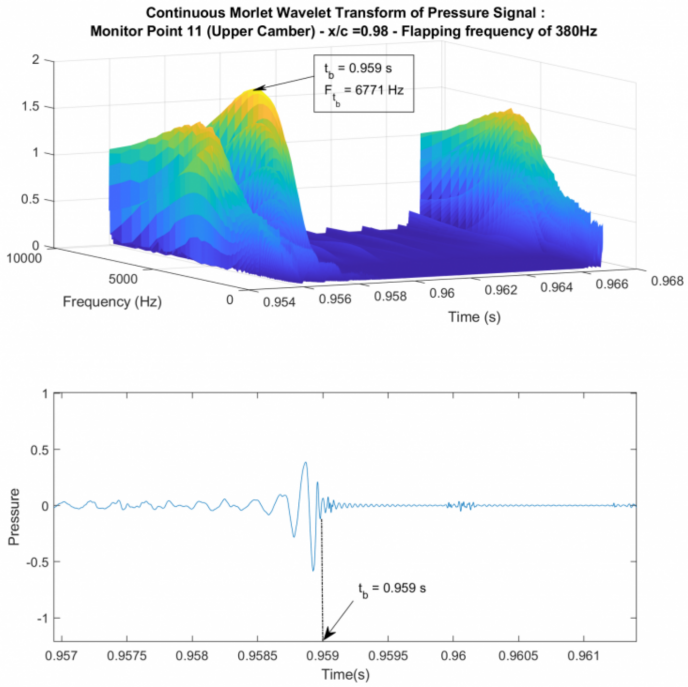

Figure 7.51: Wavelet analysis of the pressure signal at the upper surface (probe 11), for a flapping frequency of 380 Hz.

From the wavelet analysis, it is remarked that at $t_b = 0.959$ s, a considerable pressure fluctuation occurs at a frequency of $f_{t_b} = 6771$ Hz.

We can therefore deduce that the frequency of the von Kármán instability is roughly equal to fVK = 6770 Hz for $f_{ac} = 380$ Hz.

Pressure signals extracted at probe 22 are also analyzed in order to identify the vortex instabilities captured in the wake at that location for an actuation frequency of 380 Hz (fig. 7.53). Because both probes 11 and 22 are accessible in the time-frequency analysis, it is possible to deduce the velocity at which coherent vortices are transported, by identifying the time delay $t_{b,deph} - t_b$ that separates the burst measured at probe 11 from the one measured at probe 22. This way, it is possible to make sense of the nature of the high frequency modes in the time series: each time coherent eddies are transported past a monitor probe, high-frequency events are captured and a wavelet analysis is able to identify the associated frequencies. The wavelet transform thus helps to identify the physical source of certain modes that

are detected thanks to a spectral analysis, while the PSD provides better spectral resolution and a more general view of all the modes contained in the signal.

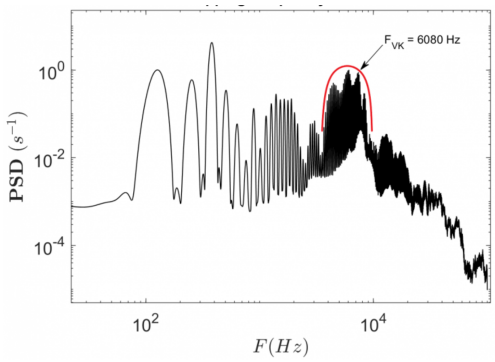

Figure 7.52: PSD diagram of the pressure signal at the wake (probe 22), for a morphing frequency of 380 Hz.

From the PSD diagram in fig. 7.52, it is assessed that vortices are shed inside the wake at a frequency of about 6080 Hz. These correspond to a von Kármán instability.

By employing a similar approach, a wavelet analysis is performed on the pressure measurements extracted from probe 15, as shown in the following figure:

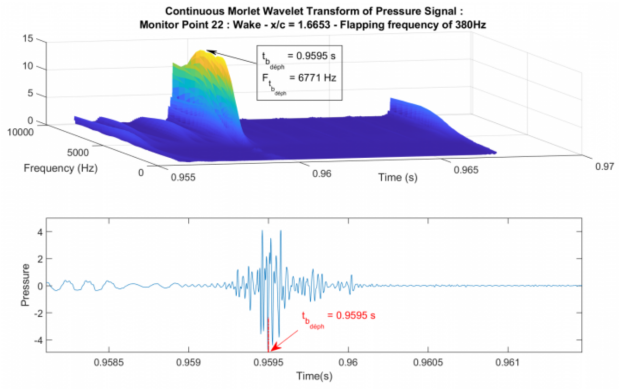

Figure 7.53: Wavelet analysis of the pressure signal at the wake level (probe 22), for a 380 Hz flapping frequency.

It is found from figure 7.53 that a strong fluctuation in pressure takes place around the timestamp $t_{b,deph} = 0.9595$ s, such that $t_{b,deph} = t_b + \delta t = t_b + 5 \times 10^{-4}$ s recorded at the level of probe 11. The frequency of instabilities in this case is also of the order of 6700 Hz, and are therefore identified as von Kármán vortices.

The time lag Δt observed between the two probes is the time taken by coherent eddies to travel the distance d that separates probe 11 from probe 22. It is thus possible to deduce the advection velocity by dividing d by Δt. It is found that vortices are advected at a velocity approximately equal to $V_{adv} = 203$ m/s for a corresponding shedding frequency of vortices is then about $F_{adv} = 104$ Hz.

- **The 365 Hz morphing configuration**

After studying the case of a 380 Hz flapping frequency, we are interested in the case of a flapping frequency of 365 Hz in order to compare between the vortex instabilities displayed.

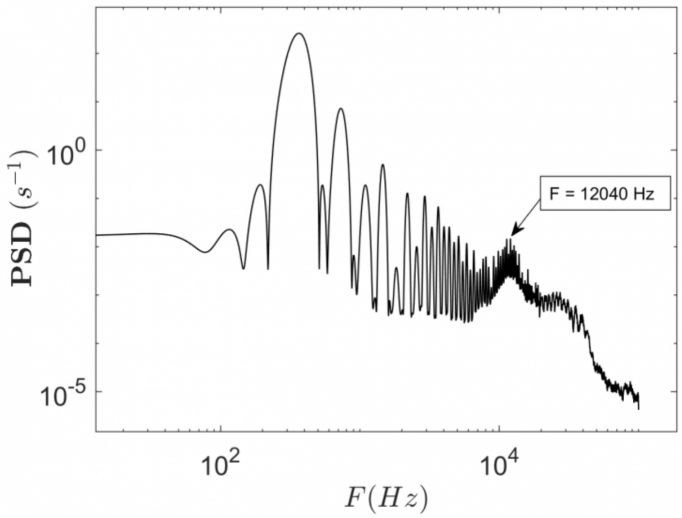

Figure 7.54: PSD diagram of the pressure signal at the upper surface (probe 11), at a vibration frequency of 365 Hz.

In particular, we looked at the flow at the upper surface, around probe 11.

It can be verified, according to figure 7.54, that morphing at an actuation frequency of 365 Hz considerably reduces the intensity of the spectral power level by a factor of the order of 102 compared to morphing performed at 380 Hz, while the higher frequency modes are pushed back to frequencies of the order of 12×10^3 Hz. This shows that morphing at 365 Hz is able to diminish the strength of wake instabilities.

7.2.4.2 Shock motion and pressure coefficient

Here, the position of the shock with respect to time is studied in the case of two frequencies, namely 365 Hz and 380 Hz, as well as the interaction between the shock and the detached boundary layer. Then the average pressure coefficient is computed from the surface pressure in an attempt to explain where the lift or drag variations arise.

Shock position

Visualizing the evolution of the pressure gradient across the shock allows to track the shock along its motion and monitor its position over time. It has been observed that the shock travels over a longer distance in the case of an actuation frequency of 380 Hz compared to 365 Hz. This confirms the result obtained in the previous section where it has been determined that the amplitude of buffet oscillations is weaker in the 365 Hz case in comparison to 380 Hz. Furthermore, it is found that vorticity in the separated shear layer is more pronounced for $f_{ac} = 380$ Hz than it is for $f_{ac} = 365$ Hz on average. This shows that for $f_{ac} = 380$ Hz, **morphing increases strain rate inside the shear layer which in turn accentuates the strength of the interaction** between the shock and the separated boundary layer, causing a stronger buffet instability, hence increasing force RMS.

It has already been found in previous studies such as Grossi, Braza, and Hoarau, 2014, Szubert, 2015 and Tô et al., 2019 that the thickness of the separated region increases as the shock moves upstream towards the leading edge, which diminishes the lift coefficient. Indeed, as lift is mostly due to the amount of difference between suction-side and pressure-side pressure, the relative intensity of this force can be estimated by how much area is

encompassed within the C_p curves. It is apparent that the C_p curve for $f_{ac} = 380$ Hz comprises a bigger area than that of $f_{ac} = 365$ Hz, hence coinciding with the data emerging from figure 7.48 and table 7.5. However, the pressure slope between $x = 0.1$ m and $x = 0.12$ m (equivalently between $x/c = 2/3$ and $x/c = 4/5$

Average pressure coefficient

The average pressure coefficient as a function of the longitudinal coordinate x is examined in further detail to visually inspect the peculiarities of the pressure distribution around the wing for several actuation frequencies.

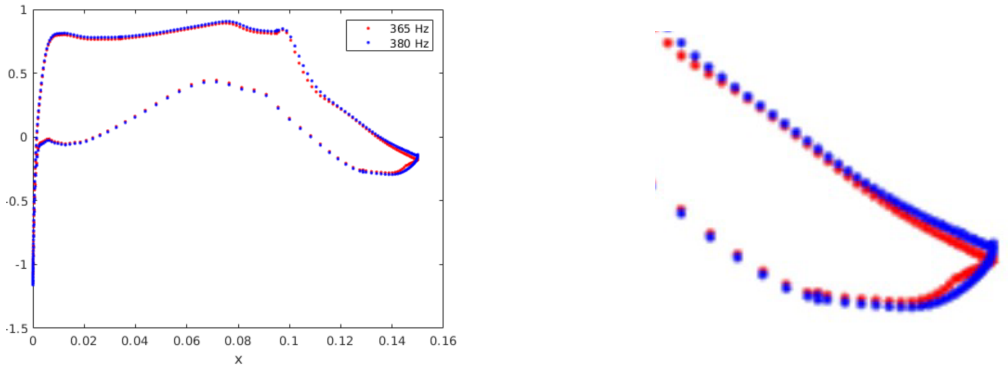

(a) (b)

Figure 7.55: (a) Average pressure coefficient as a function of x for two actuation frequencies 365 Hz and 380 Hz. (b) Zoom on the trailing edge portion ($x/c > 0.7$)

In figure 7.55, it can be seen that the pressure coefficient for an actuation frequency of 380 Hz has a slightly thicker tail ($x > 0.11$) than the pressure coefficient profile for $f_{ac} = 365$ Hz, and therefore a higher pressure difference between the suction side and pressure side of the trailing edge can be noted for the 380 Hz actuation frequency. This naturally results in an increased lift for the 380 Hz case compared to the 365 Hz case, as shown by the integration of the average lift coefficient which equals 0.5227 for $f_{ac} = 380$ Hz while it is equal to 0.4944 for $f_{ac} = 365$ Hz. The aforementioned averaged pressure difference signifies that shape drag (as a consequence of an increased induced drag) is more significant in that zone. Therefore, this explains that the 380

Hz actuation frequency produces more drag than the 365 Hz case which correlates with the results of table 7.5. In addition, it can be noted that the average pressure coefficient is slightly steeper in the compression zone (where the shock lies) for the 365 Hz case compared to an actuation frequency of 380 Hz. This means that, on average, the shock travels a smaller length along the top of the airfoil for an actuation frequency of 365 Hz. This result shows that the SWBLI being rendered weaker by the actuation is the reason why specific actuation frequencies effectively reduce the RMS of the pressure.

Time-averaged wake velocity profile

Finally, we focus the study around the analysis of the thickness (or width) of the velocity profile in the wake for several actuation frequencies. The graph 7.55 compares the effect of a 365 Hz actuation frequency and a 380 Hz frequency on the time-averaged velocity profile in the wake at a non-dimensional coordinate $x/c = 1.20$:

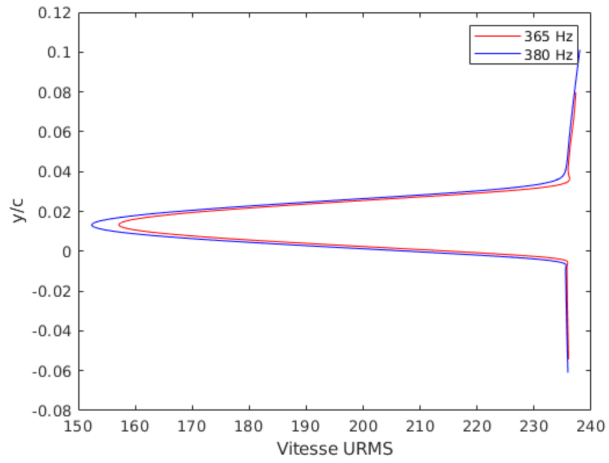

Figure 7.56: Time-averaged longitudinal velocity profile as a function of the vertical direction for two frequencies 365 Hz and 380 Hz.

It can be seen that the velocity profile is thicker, that is it has a greater vertical extension for an actuation frequency of 380 Hz compared to 365 Hz, which appears to be consistent with the previous observation that the shock moves back and forth with a higher motion amplitude for 380 Hz. Therefore, it creates a thicker detached shear layer and thus a thicker wake

on average. The wake velocity deficit is also more important in the 380 Hz case which means that the adverse pressure gradient is more important for that actuation frequency. Indeed, since the amplitude of the shock motion is more pronounced in the $f_{ac} = 380$ Hz case, the velocity of the shock relatively to the shear layer is more important, creating a more significant BL separation since it depends on the flow velocity relative to the shock, as is mentioned by Babinsky and Harvey, 2011. Indeed, it has been seen that in the case of an actuation frequency of 380 Hz, the buffet instability is not weakened but it is rather reinforced (fig. 7.48).

7.2.4.3 Partial conclusion

From this analysis, an optimal frequency is found: $f_{ac} = 365$ Hz. This frequency allowed decreasing the intensity of the buffet mode, hence reducing the rms of the lift. Drag was also observed to decrease considerably. In turn, the lift to drag ratio is strongly increased, potentially enabling a gain of efficiency and a reduction of fuel consumption in cruise flight.

In addition, the inhibition of the buffet mode helps to prevent this flow instability from interacting with the structural modes of the wing such as bending or twisting. Suppressing buffet, or at least reducing its intensity can be effective in preventing the occurrence of dip flutter which arises in the same range of Mach numbers.

References

Babinsky, H. and J. K. Harvey (2011). *Shock Wave-Boundary Layer Interactions*. ISBN: 9780521848527.

Grossi, Fernando, Marianna Braza, and Yannick Hoarau (2014). "Prediction of Transonic Buffet by Delayed Detached-Eddy Simulation". In: *AIAA Journal* 52.10, pp. 2300–2312. ISSN: 0001-1452. DOI: 10.2514/1.J052873.

Hartmann, A., A. Feldhusen, and W. Schröder (2013). "On the interaction of shock waves and sound waves in transonic buffet flow". In: *Physics of Fluids* 25.2. ISSN: 10706631. DOI: 10.1063/1.4791603.

Szubert, Damien (2015). "Physics and modelling of unsteady turbulent flows around aerodynamic and hydrodynamic structures at high Reynold number by numerical simulation". In.

Tô, J.-B. et al. (2019). "Effects of vibrating and deformed trailing edge of a morphing supercritical airfoil in transonic regime by numerical simulation at high Reynolds number". In: *Journal of Fluids and Structures*. ISSN: 0889-9746. DOI: 10.1016/J.JFLUIDSTRUCTS.2019.02.011.

Chapter 8

Manipulation of a turbulent shock-wave/boundary layer interaction around a supercritical airfoil in the transonic regime via trailing edge morphing

In this soon to be published co-authored work, part of the numerical results of the present thesis are compared to experimental results performed by IMP-PAN on the tRS "transonic Reduced Scale" morphing A320 wing prototype of the SMS project provided by one of the coordinators within INPT — the Laboratoire Plasma et Conversion d'Energie (LAPLACE) — and made available together with specific piezoactuator power supply for the experiments in IMP-PAN. The experiments used flow conditions similar to those of the numerical simulations which help confirm the main conclusions.

Manipulation of a turbulent shock-wave/boundary layer interaction around a supercritical airfoil in the transonic regime via trailing edge morphing

J.-B. TÔ*, M. BRAZA*

*Institut de Mécanique des Fluides de Toulouse, France

Introduction

A considerable number of experimental and numerical studies have been devoted to the investigation of the transonic interaction around a wing and particularly on buffet appearance, i.e the unsteady quasi-periodic shock's motion over a wing, occurring in a specific Mach number range of (from roughly $Ma = 0.7$ to $Ma = 0.8$) (McDevitt, Levy Jr., and Deiwert, 1976). This range corresponds to cruise conditions for which it is crucial to analyse the buffet dynamics in order to attenuate or suppress it, because it could create critical conditions for dip-flutter instability amplification with negative damping. Transonic buffet is a result of a fluid's unsteadiness, due to a strong interaction among the shock, the boundary layer and the separated shear layers as well as the coherent vortices formed downstream of the trailing edge, whose dynamics influence each other in a closed loop. Pioneering experimental studies driven by Seegmiller, Marvin, and Levy, 1978, McDevitt, Levy Jr., and Deiwert, 1976 and Levy Jr., 1978, Marvin, Levy Jr., and Seegmiller, 1980 and more recently by Jacquin et al., 2005 and Jacquin et al., 2009 who investigated the SWBLI associated with the buffet dynamics and its effects on the wall pressure and the aerodynamic forces including PIV measurements. Collected experimental studies of the transonic buffet can be also found by Doerffer et al., 2010 in the context of the European research programme UFAST (Unsteady Effects in Shock Wave Induced Separation) and of the European research programme TFAST (Transition Location Effect on Shock Wave Boundary Layer Interaction) [1].

In the last twenty five years, in parallel with experimental investigations, numerical studies examined the transonic interaction and the buffet phenomenon. Starting from the low Reynolds number range, the successive stages of instabilities amplification as Mach number increases had been studied through DNS and 2D numerical simulation by Bouhadji and Braza, 2003. It was shown that first, a von Kármán instability mode is amplified in the wake and makes undulation of the two separated shear layers over a NACA0012 airfoil at Reynolds number of 10,000. As Mach number increases from 0.5 to 0.6, a progressive formation of a slightly supersonic region upstream of the shock is formed and remains steady, while the von Kármán amplitude progressively increases. At Mach number of 0.7, a much lower-

[1] `http://tfast.eu` by Doerffer et al., 2010

frequency mode appears in the forces fluctuations, that envelopes a considerable number of periods of the von Kármán mode, while the upstream of the shock supersonic area starts oscillating according to this low frequency and gives birth to the buffet mode. These lower Reynolds number studies allowed precisely the follow-up of the above successive stages and made evidence of the history in the appearance of the different instability modes, a fact that is difficult to observe experimentally, because the amplification of these modes in the high Reynolds number range occurs quite fast. As Mach number increases in the range (0.7 - 0.8), the buffet amplitudes increase and continue enveloping the von Kármán mode periods, while the averaged shock position progressively moves downstream. As Mach number increases up to 0.85, only the von Kármán mode persists up to Mach numbers 0.9 in the forces fluctuations, while the wall pressure is practically steady. This is due to the shock wave occurrence in most downstream positions because of the progressive increase of the hyperbolic character of the flow with the Mach number increase. At Mach numbers in the range (0.9 - 0.95) the shock wave has moved in the wake and the forces are steady. Bourdet et al., 2003 studied the buffet instability amplification by DNS and by means of the Landau global oscillator model around a NACA0012 airfoil. The DNS study illustrated the secondary instability amplification and the formation of spanwise undulated vortex structures in the near wake, governed by predominent large-scale wave lengths. This pattern persists in the high Reynolds number range concerning the three-dimensional character of the coherent structures past the trailing edge, as shown by Delayed Detached Eddy Simulation in Grossi, Braza, and Hoarau, 2014 around a supercritical wing, the OAT15A a Mach numbers corresonding to the buffet ocurrence and Reynolds numbers of order 3 million, studied in the context of the European research programme ATAAC . In these studies, the shock wave structure and the buffet dynamics were found not considerably affected by the three-dimensionnality. For these reasons, as mentioned below, a two-dimensional approach can be used in order to ensure a rich parametric study concerning the morphing effects. Moreover, the Zonal Detached Eddy Simulations, ZDES by Deck, 2005 presents a quite complete analysis of the transonic interaction around the OAT15A and a promising turbulence modelling approach. Moreover, 2D URANS studies by (Brunet, 2003) have also provided a detailed physical analysis of the buffet around the same configuration. More recently, Szubert et al., 2015b, studied the transonic interaction among the buffet, the shear layer vortices and the von Kármán vortices by 2D numerical simulation using

the Organised Eddy Simulation, OES (see Braza, Perrin, and Hoarau, 2006 and Bourguet et al., 2009). Through this method, able to capture the instabilities amplification and the coherent structure dynamics in 2D and 3D, the aforementioned interaction was studied as well as its impact on the pressure and forces fluctuations, by means of wavelets and Proper Orthogonal Decomposition (POD). The role of the higher-order modes in producing a shear sheltering effect in the separated shear layers past the SWBLI was analysed and used to create a stochastic forcing by re-injection of turbulence in these layers and in the shock's shearing region, as source terms in the turbulence transport equations, in the so-called IOES (Improved OES) approach. This forcing acts as an eddy-blocking effect as described in Hunt, Eames, and Westerweel, 2008 resulting in a considerable thinning of the shear layers and of the wake's width. This effect, besides a significant improvement of the pressure coefficient and the forces evaluation, is used in the present study in order to enhance the benefits from the morphing as described in the results discussion. Moreover, the transition location effects on the buffet have been studied and optimised in the same high Reynolds number range for the supercritical wing V2C design by Dassault Aviation in the context of the TFAST European project. Szubert, 2015 studied transonic buffet via a combined DDES-OES approach and carried out an optimisation of the transition location. The study by Bonne, 2018 proposed quite successful physical models of the laminar SWBLI that allowed analysis of the multi-modal coupling in the high Reynolds number range, offering physical mechanisms comprehension of high interest for the industrial applications, including buffet study in swept wings by numerical simulation.

The objective of the present article is to study the effects of morphing on the flow dynamics regarding an unconfined 2D configuration to help the design the A320 morphing prototype in the context of the H2020 European research project Smart Morphing and Sensing (SMS) . This study served to implement the best type of actuations near the trailing edge of the experimental prototype, in order to obtain optimal increase of the aerodynamic performance. To this end, the actuations studied in the present paper by means of numerical simulation fit the hardware actuations studied in a number of experimental works of the present research group in the context of the SMS research platform, supported by the French Foundation « Sciences et Technologies pour l'Aéronautique et l'Espace » – (STAE), and in other recent studies as follows.

It has been shown in Scheller, 2015 and Scheller et al., 2015 that vortex breakdown occurs by trailing edge vibrations using PUSH-PUSH piezoactuators in the trailing-edge region of a NACA0012 wing, with a singificant lift improvement, drag and noise sources decrease, in the context of the STAE Research projects research project EMMAV - Electroactive Morphing for Micro-Airvehicles using Shape Memory Alloys (SMA) (Chinaud et al., 2014) and DYNAMORPH: Dynamic Regime Electroactive Morphing", by means of a combined action of SMA and piezoactuators (Scheller et al., 2015). Furthermore, the European research programme SARISTU had considered morphing trailing edge devices through SMA and MEMS. The European programme SADE developed morphing devices for the leading edge and the wings by using flexible matrix composites (FMC). In particular, the MFC piezoactuators provided good performances in subsonic flow conditions (cf. Scheller et al., 2015 and Jodin et al., 2017). The actuation concept associating different degrees of deformation and vibration at multiple time scales is called hybrid electro-active morphing in these studies by the multidisciplinary research group IMFT-LAPLACE. It was demonstrated that the flow dynamics are significantly affected by the trailing edge actuation. An important reduction of the wake's width and spectral energy associated to drag and aerodynamic noise respectively was quantified by means of Particle Image Velocimetry (PIV) measurements. In the context of these studies, the aim of the hybrid morphing concept is to use the turbulence itself, in order to manipulate part of the "harmful" eddies and to enhance the beneficial ones thanks to the « eddy blocking effect » Hunt, Eames, and Westerweel, 2008 previously mentioned. The objective is to increase the aerodynamic performances and simultaneously decrease the intensity of acoustic sources generated from predominant coherent instability modes as well as turbulent stresses. Hence, at a given controlled camber, the vibrating trailing edge adds kinetic energy in the wake which fosters the suppression of coherent turbulent structures. This kind of actuation is precisely studied numerically in the present article at different frequencies and an amplitude of about $\pm$ 1° around the clean and immobile airfoil, which is named the « static » case. It is worth mentioning that in transonic speeds, only slight deformations of the rear region are recommended, whereas in low subsonic speeds, large deformations are needed due to the different turbulent scales dictated by different Reynolds number and angles of incidence. Therefore, the present article will examine the effects of a slightly deformed and vibrating trailing-edge in a wide frequency range. It will then focus on determining a mechanism through which morphing acts

to improve aerodynamic forces in cruise flight.

There do not exist, to our knowledge, studies concerning morphing in transonic regimes where the target is to increase lift-to-drag ratio and to decrease drag as well as acoustic generation. The numerical study by Barbut et al., 2010 by means of DDES (Delayed Detached Eddy Simulation) investigated the dynamics around a NACA0012 wing with an oscillating trailing edge in the transonic regime. An experimental and numerical study around this wing can be found in a work by Doerffer et al., 2010.

Therefore, the objectives of this paper are to examine the effects of morphing of the rear part of the wing by suitable deformations and vibrations able to manipulate the surrounding turbulence and vortex dynamics and able to be realised in experimental environment and in real flight.

This paper is thus articulated as follows: In the first section, the numerical parameters and turbulence modelling are introduced. Secondly, the results are presented investigating the effects of morphing on the aerodynamic performance of the wing by different trailing-edge vibrations, by a slight deformation upwards and by combining both actuations. The results are discussed regarding optimal behaviours in respect of aerodynamic performance and finally the conclusions are drawn in the last part of the article.

Experimental setup

Two reduced models of an Airbus A320 extruded airfoil in clean configuration were used to conduct this study. One of them – the static or « reference » prototype – is unactuated while a piezoelectric actuator was implemented in the second one, namely the « morphing » transonic Reduced-Scale A320 prototype of the SMS project (or tRS). The wing model has a chord of 15 cm in order to fit the test section and it fills the entire width of the test section. Both the static prototype as well as the actuated prototype were installed in a wind tunnel section in the IMP-PAN transonic wind tunnel. The test section is 10 cm wide (cf. Figure 8.1).

The choice of the flow conditions for these tests were motivated by the requirement that the Mach number $\mathrm{Ma} = 0.78$ should remain similar to that of real flight conditions in cruise phase for a commercial A320 aircraft. The

chord had to be adjusted for the wing prototype to enjoy enough vertical clearance in order to avoid ground and wall effects, while pressure and temperature were set by operating conditions within the transonic wind tunnel. The angle of attack AoA = 1.8°, similarly to the Mach number, is identical to real flight conditions in order to respect the parameters that would cause the onset or absence of buffet in real flight. The resulting Reynolds number of both the experiments and the numerical simulations is $Re = 2.06 \times 10^6$ and the inlet turbulence intensity is 0.5 %.

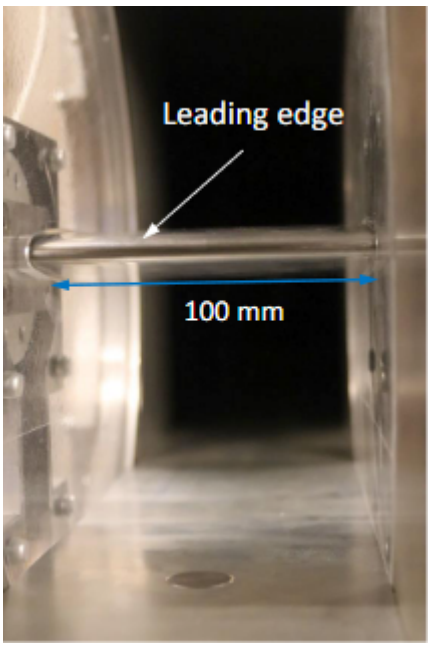

Figure 8.1: Picture of the reference prototype in the assembled test section.

Two pressure taps were installed along the suction side of the reference prototype at distances $x/c = 0.57$ and $x/c = 0.9$ on both sides of the shock in order to measure unsteady pressure disturbances created by the SWBLI upstream and downstream the shock.

Velocity profile measurements have been performed aft the trailing edge of the prototype via Laser Doppler Anenometry (LDA).

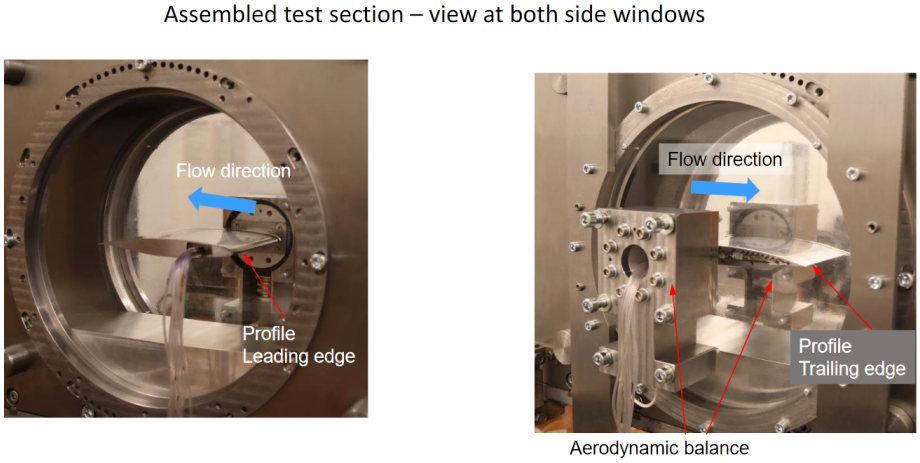

Figure 8.2: Forward and backward views of the test section, showing the implementation of an aerodynamic balance for the measure of lift and drag.

Numerical setup

Numerical simulations were performed with the Navier-Stokes Multi-Block (NSMB) parallel solver jointly developed by a consortium of players in the aerospace industry; among those EPFL-CFSE, CERFACS, KTH, IMFT, ICUBE, University of Karlsruhe, ETH-Ecole Polytechnique de Zurich, AIRBUS and others. It was made available for launching CFD simulations thanks to our long-time partnership with CFS Engineering within the Smart Morphing and Sensing (SMS) European H2020 programme which was piloted by IMFT and took place over a period of three years, from 2017 to 2020.

Past studies such as Szubert et al., 2015b and Grossi, Braza, and Hoarau, 2014 have already defined the numerical framework that should be employed for similar simulations in the transonic regime. As such, an implicit dual time-stepping scheme based on the LU-SGS approach was chosen while a third order upwind Roe scheme was used to discretize the spatial fluxes.

Turbulence is modelled with the use of an Organised Eddy Simulation (OES) approach (cf. Braza, Perrin, and Hoarau, 2006 and Szubert et al., 2015a), a formulation that effectively distinguishes coherent structures from the chaotic and random diffuse background of turbulence. As such, variables

are not split into a statistical average and a modelled fluctuation, but their phase average is taken so as to capture the spatio-temporal repetitiveness of coherent eddies, depicted by a strong self-correlation in two-point statistics. From a frequential point of view, this is equivalent to discretising the energy spectrum of a spatial or temporal signal into the sum of an organised part, distinguishable by the presence of peaks describing repetitive modes, and a chaotic part characterised by a continuous decaying spectrum. It was shown by TRPIV experiments (cf. Braza, Perrin, and Hoarau, 2006) that the slope of the turbulence spectrum in the inertial range is drastically modified compared to equilibrium turbulence spectra where the slope typically scales as $-5/3$. This slope modification due to the coherent structures dynamics is directly related to strong stress-strain misalignments that have been also quantified by Perrin, 2005 and Bourguet et al., 2008. Therefore, the latter part of the spectrum has to be modelled in such a formulation, and one has to account for the slope modification of the chaotic spectrum in the inertial range caused by the non-linear mechanisms that cause the organised eddies to appear in the first place: Regions where turbulence is in a state of non-equilibrium — such as in the rear part of a cylinder where both friction and adverse pressure gradients are important.

Therefore, the Boussinesq approximation has to be reconsidered to take into account this stress-strain misalignment. This has been accomplished through a tensorial eddy viscosity concept (cf. Bourguet et al., 2009), yielding a directional C_μ eddy-diffusion coefficient varying in the range $0.02 - 0.03$, by projecting a second-order moment closure on the principal directions of the strain rate.

Thus, the diffusive parameter C_μ that intervenes in the expression of the eddy viscosity as per Boussinesq's assumption has to be modified according to results in Bradshaw, 1973 showing that the quantity $C_\mu^{1/2} \approx \frac{-\overline{uv}}{k}$ is non-constant in the context of turbulent boundary layers in the presence of an adverse pressure gradient, and takes significantly smaller values in the inertial subrange than is the case for a flat plate in similar flow conditions.

This was further discussed in Hoarau, 2002 who evaluated an equivalent C_μ coefficient by means of second order modelling and by DNS over a highly separated NACA0012 wing at high Reynolds number, among other works. In addition, the previously mentioned studies in the wake of a cylinder at high Reynolds numbers quantified the change of slope in the spectrum caused by the interaction between coherent and incoherent eddies, reflecting a deviation from homogeneous and isotropic turbulence in the inertial range, manifesting

as non-equilibrium turbulence involving different length scales and ultimately leading to less turbulent diffusion in these zones, thus allowing the correct representation of coherent structures and more accurate quantification of turbulence properties. Furthermore, a change in the variation of the turbulence damping function f_μ has been adopted, reported by Jin and Braza, 1994, where a lower slope of the f_μ variation was proven efficient to deal with the development of coherent structures.

Simulations were carried out in coordination with the Gdańsk team who were in charge of experimental measures using their transonic wind tunnel to cross-validate test cases. This means that many numerical parameters had to be chosen beforehand to accommodate and respect flow conditions found in the transonic wind tunnel. It is worth noticing that the optimal vibration detection by the numerical simulations performed in the present thesis were carried out prior to the experiments (especially the first optimal range detected around 300 Hz) and helped the conducted experiments to apply the same frequency ranges within the SMS project.

A two-dimensional multi-block structured grid generated by NUMECA - IGG was used for the purpose of the computations. It is made of 200000 mesh cells arranged in a C topology with a first layer of cells located at $y^+ < 0.1$ around the wing profile (cf. figure 8.3). The time step of the simulation was $\Delta t = 5 \times 10^{-6}$ s.

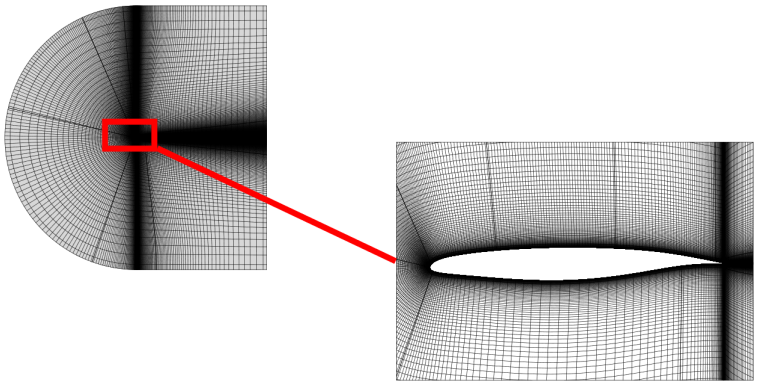

Figure 8.3: Schematic diagram showing the computational mesh and the domain topology.

Results

Phenomenology

Experimental and numerical testing was carried out at an angle of incidence of 1.8° in two configurations – that is in the morphing case and the static case – in order to demonstrate the effects of morphing on the alteration of aerodynamic stresses around the wing profile, as well as to analyse the modification of the qualitative behavior of airflow in the transonic regime.

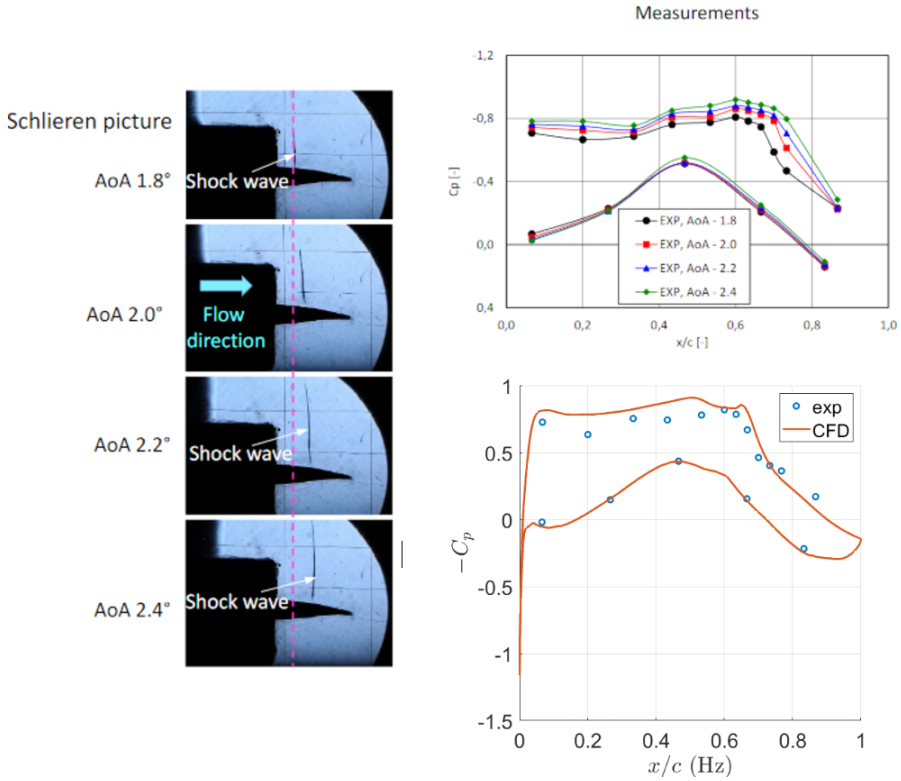

Figure 8.4: (a) Schlieren pictures showing the incidence-angle dependence of the shock position along the suction side of the wing profile. (b) Measurements quantifying the displacement of the shock downstream as the angle of incidence increases. (c) Comparison between CFD (IMFT) and experimental results (IMP-PAN).

A first campaign of wind tunnel tests aimed to determine the shock posi-

tion along the upper surface as a function of the angle of attack. In particular, numerical simulations have demonstrated a good agreement in terms of shock position.

These Schlieren images were used to qualitatively verify that an increase in the angle of attack has the effect of moving the shock downstream. Numerical simulations show a good agreement in terms of the shock position as shown in figure 8.4-c.

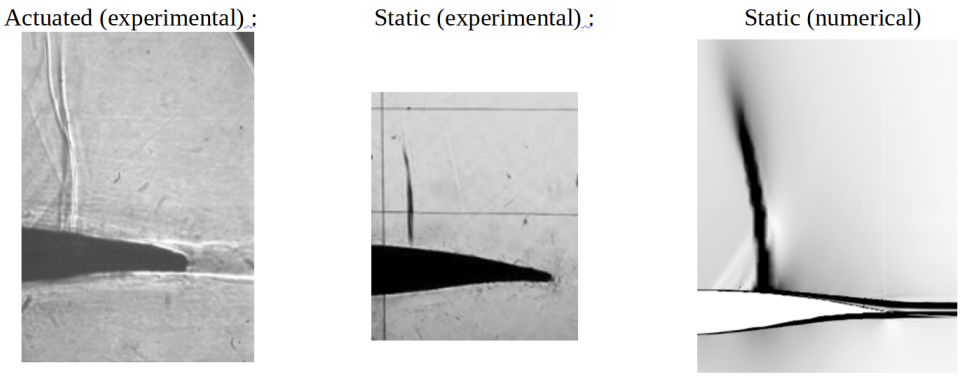

Figure 8.5: Experimental and numerical Schlieren images. From left to right: (a) In the case of a morphing prototype (b) For a static prototype (c) A numerical Schlieren representing the longitudinal density gradient around a static wing.

Figure 8.5 also shows the appearance of the lambda shock pattern in both experimental tests and numerical simulations.

These Schlieren results show the presence of a characteristic lambda shock over the suction side of the wing in the transonic flow regime. This lambda-shaped shock foot is caused by an initial separation of the boundary layer along the suction side of the wing which results from a natural transition towards turbulence, emphasized by the curvature of the wing profile. This transition may be emphasized by the presence of surface roughness, unevenness, an important curvature of the profile or specific flow regimes.

Figure 8.6 shows a numerical Schlieren taken from the results of a CFD simulation, displaying longitudinal iso-contours of density gradients on top of which streaklines are superimposed in order to demonstrate the flow re-

circulation that takes place after the shock.

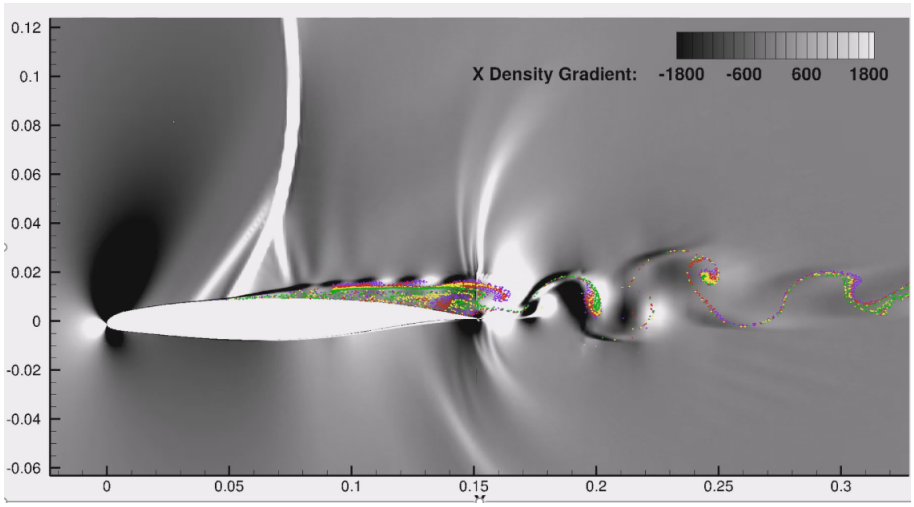

Figure 8.6: iso-contours of density gradient displaying the lambda shock and other flow features in the transonic regime for $Ma = 0.78$ and $Re = 2.06 \times 10^6$. The angle of attack chosen for this simulation is 5° in order to better highlight the flow recirculation that takes place as well as feedback effects that send information back towards the shock foot.

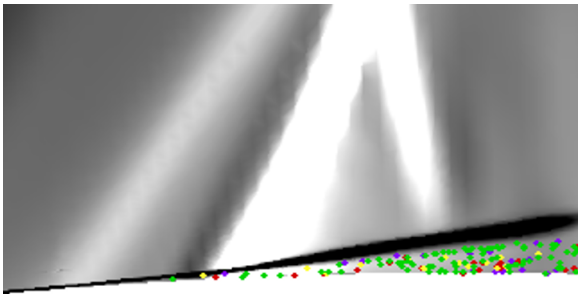

Figure 8.7: Zoom of figure 8.6 around the shock foot. Streaklines are transported upstream along the boundary layer and are shown to travel until they overshoot the shock foot.

Indeed, although the flow can be modelled as inviscid in the irrotational part, boundary layer flow takes place at low speeds and can be seen as a viscous layer wherein diffusive transport takes place at comparable or higher velocities than advective transport. The parabolic nature of the Navier-Stokes equations within this viscous layer means that information may propagate

along all directions, including in the upstream direction. And the presence of reverse flow due to the separation of the boundary layer under the effect of pronounced body curvature contributes to the advective transport of pressure disturbances coming from the trailing edge (see figures 8.6 and 8.7).

Moreover, it was shown that the shock-wave and boundary layer interaction comes from a self-interaction occurring within the boundary layer in the vicinity of the shock foot, cf. Lagrée, 2010. The curvature of the airfoil naturally causes the flow to accelerate in the inviscid region and promotes the formation of a shock when the flow has reached criticality. Since the shock suddenly compresses the flow and increases the strength of the reverse pressure gradient, its presence tends to thicken up the boundary layer close to the shock foot, which deviates streamlines within the boundary layer and causes the displacement thickness of the boundary layer to increase locally. However, this thickness variation of the effective obstacle as seen by the inviscid external flow, represented by the displacement thickness of the boundary layer, retroacts on the inviscid flow and induces pressure fluctuations which then influence the thickness of the boundary layer in that region. This explains why it is possible to observe the boundary layer becoming thicker ahead of the shock foot, because shock-wave boundary layer instabilities behave as self-induced interactions which sustain themselves over time when conditions in terms of Mach number and angle of attack allow their existence.

This strongly suggests that any perturbation coming from the trailing edge influences the solution close to the shock foot where the aforementioned interaction takes place. This is due to the elliptic nature of the Navier-Stokes equations within the boundary layer. Such an observation would suggest that this upstream advection, which acts as a feedback effect, allows pressure disturbances coming from the trailing edge to manipulate buffet and possibly augment or alleviate the strength of the instability.

Hence, experimental tests were carried out in both morphing and static configuration in order to investigate and identify possible effects that would point to this feedback loop coming from the trailing edge towards the shock foot. A previous study had already exhibited the existence of a lock-in phenomenon which reflects a synchronization between the deformation frequency of the trailing edge and the frequency of buffet Tô et al., 2019. In order to

demonstrate this experimentally, a Schlieren apparatus made it possible to visualize the movement of the shock along the upper surface of the wing over time. A shock detection algorithm was then implemented to determine the time evolution of the shock position as being measured along a line at a fixed height of $y = 10^{-2}$ m from the surface of the wing at the shock foot, shown in figure 8.8.

By calculating the Fourier transform of the shock motion time series obtained on the one hand without any vibration of the trailing edge and on the other hand with a vibration of the trailing edge, it is possible to note the presence of an energetic mode at 300 Hz in the case of a vibrating trailing edge, cf. figure 8.9. This demonstrates that the instability resulting from an interaction between shock and boundary layer is excited by the activation of the trailing edge and that its frequency is synchronized with that of the trailing edge.

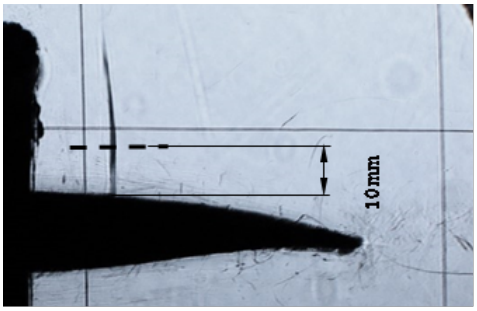

Figure 8.8: Schlieren image of the reference prototype installed in the wind-tunnel. The line the time evolution of the shock position.

From the fact that the shock moves back and forth at the same frequency as the trailing edge, it is possible to presume that there are disturbances propagating from the trailing edge upstream through the subsonic boundary layer. This frequential synchronization can also be observed in numerical calculations, as shown in figure 8.10. Indeed, the power spectral density of the lift coefficient over time shows the presence of a peak in the spectrum at a frequency of 350 Hz, the same frequency as that which the trailing edge vibrates in that case. This peak is followed by a succession of harmonics indicating the highly periodic nature of the oscillating aerodynamic forces exerted on the wing caused by the vibrating trailing edge.

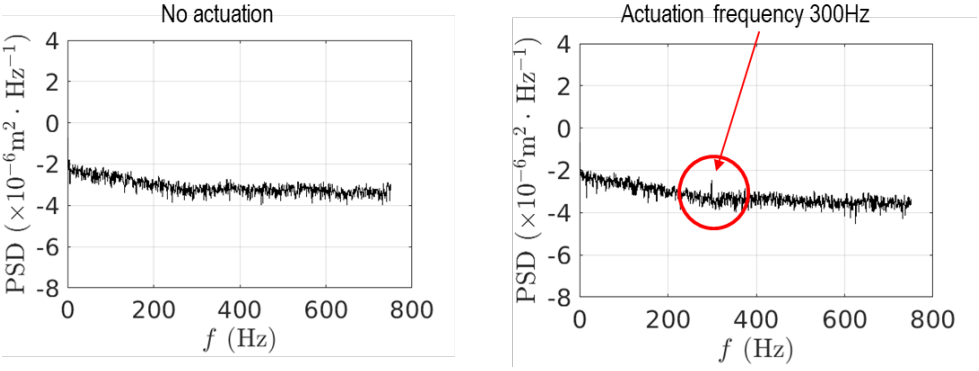

Figure 8.9: Power spectra of the shock position time series showing the presence of an energetic mode at 300 Hz when the trailing edge is actuated.

This contrasts with the power spectrum calculated from the aerodynamic forces on a static wing (in black), where we can see a predominant mode at 111 Hz, which is the natural frequency of buffet at that particular flow regime and angle of incidence.

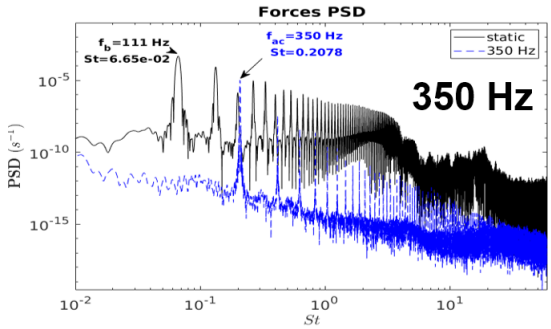

Figure 8.10: Power spectral density of the lift coefficient time series resulting from 2D numerical simulations.

8.0.1 Comparison of the aerodynamic performance of the actuated wing profile against the static wing

A parametric study has been carried out over a span of frequencies ranging from 100 to 450 Hz in order to determine the effect of the actuation frequency on the time-averaged aerodynamic forces. The time-averaged relative change

of lift (L), drag (D) and lift over drag ratio (L/D) induced by morphing in relation to the static case have been determined from numerical calculations about the transonic flow around a 2D wing profile with the same physical and numerical parameters mentioned in the section referring to the numerical setup. The time averages were calculated from time series of the forces which were computed over a duration exceeding 1 second of physical time.

It is found that actuation frequencies 150 Hz, 250 Hz, 300 Hz and 350 Hz both decrease drag and increase lift to drag ratio while other frequencies such as 100 Hz and 200 Hz present a simultaneous decrease of drag and lift to drag ratio or an increase of these parameters respectively. Among the first four actuation frequencies, both 300 Hz and 350 Hz display significant improvements in terms of drag and L/D, with a drag reduction of nearly 3.5 % for a trailing edge frequency of 300 Hz and a drag reduction close to 8.9 % for a frequency of 350 Hz. This has to be set against a lift decrease in both cases, since lift is being reduced by 1.1 % for 300 Hz and by close to 3.8 % for an actuation frequency of 350 Hz. However, since lift is not being reduced as much as drag is decreased by the trailing edge vibration, the lift to drag ratio is increased by as much as 5.5 % for the 350 Hz case and by 2.5 % for the 300 Hz case.

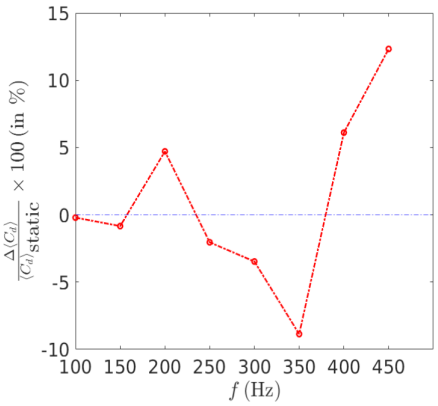

Figure 8.11: Time-averaged relative change of the drag coefficient relative to the static case $\frac{\langle C_{d,morphing}\rangle - \langle C_{d,static}\rangle}{\langle C_{d,static}\rangle} \times 100$ (in percents) for several actuation frequencies.

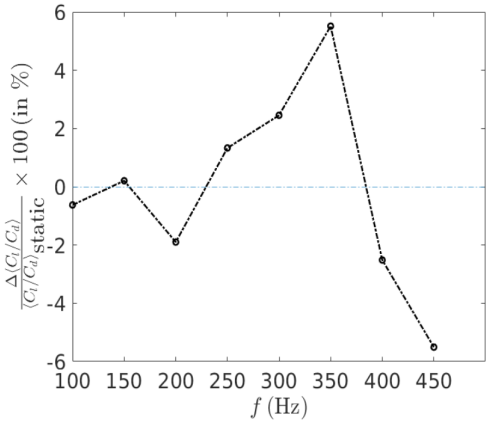

Figure 8.12: Time-averaged relative change of the lift to drag coefficient relative to the static case $\frac{\langle C_l/C_{d,morphing}\rangle - \langle C_l/C_{d,static}\rangle}{\langle C_l/C_{d,morphing}\rangle} \times 100$ for several actuation frequencies.

Frequency (Hz)	100	150	200	250	300
$100 \times \frac{\langle C_d\rangle - \langle C_d\rangle_{\text{static}}}{\langle C_d\rangle_{\text{static}}}$	-0.21%	-0.84%	4.71%	-2.07%	-3.47%
$100 \times \frac{\langle C_d\rangle - \langle C_d\rangle_{\text{static}}}{\langle C_d\rangle_{\text{static}}}$	-0.83%	-0.63%	2.73%	-0.74%	-1.10%
$100 \times \frac{\langle C_l/C_d\rangle - \langle C_l/C_d\rangle_{\text{static}}}{\langle C_l/C_d\rangle_{\text{static}}}$	-0.62%	0.20%	-1.89%	1.33%	2.46%

Frequency (Hz)	350	400	450
$100 \times \frac{\langle C_d\rangle - \langle C_d\rangle_{\text{static}}}{\langle C_d\rangle_{\text{static}}}$	-8.87%	6.11%	12.33%
$100 \times \frac{\langle C_d\rangle - \langle C_d\rangle_{\text{static}}}{\langle C_d\rangle_{\text{static}}}$	-3.84%	3.45%	6.12%
$100 \times \frac{\langle C_l/C_d\rangle - \langle C_l/C_d\rangle_{\text{static}}}{\langle C_l/C_d\rangle_{\text{static}}}$	5.51%	-2.52%	-5.50%

Table 8.1: Relative change (percentage) of time-averaged force coefficients with respect to the static case for actuation frequencies ≤ 450 Hz. A positive (resp. negative) value means an increase (resp. decrease) in percents of the force coefficient compared to the static case.

Experimental tests performed in the transonic wind tunnel of Gdansk only compared the static case and an actuation frequency of 300 Hz. They showed that the performance improvements were of a similar order of magnitude compared to numerical calculations, with a lift coefficient reduction of 1.5 % when trailing edge morphing is applied at a fixed vibration frequency of 300

Hz while drag is reduced by 4.1 % and L/D being also reduced by nearly 3.1 % according to the following table:

Actuation	C_l	C_d	C_l/C_d
0 Hz	0.205	0.169	1.212
300 Hz	0.202	0.162	1.249

Table 8.2: Aerodynamic forces measured experimentally on the static prototype – denoted by an actuation performed at 0 Hz – and the morphing prototype – denoted by 300 Hz.

Discussion

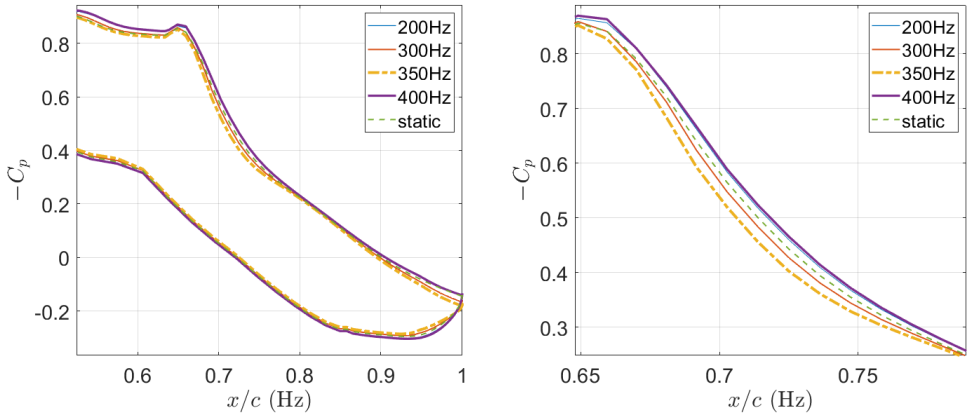

(a) Pressure distribution around the airfoil for $x/c > 0.5$

(b) Zoom

Figure 8.13: Simulated Cp profile for various actuation frequencies and the static case. (a) Display of the pressure distribution for $x/c > 0.5$ (b) Zoom of the pressure distribution in the region of the shock (sharp pressure gradient along the suction side in (a)).

Plotting the numerically calculated time-averaged pressure coefficient around the wing profile shows that the pressure differential between the pressure side and the suction side of the wing is less important than the static case when

the chosen actuation frequency causes a reduction of drag, namely for 300 Hz and 350 Hz, in contrast with cases that present a significant increase of drag, such as 200 Hz and 400 Hz, for which the pressure differential between the top and the bottom of the wing is more important than the static case.

Moreover, the compression zone that showcases the presence of the shock along the suction side of the airfoil, shown in figure 8.13-b, is not only more slanted in the static case, but also for frequencies of 200 Hz and 400 Hz whereas it is slightly more upright for a frequency of 300 Hz and 350 Hz. This means that the amplitude of the shock oscillations, which is due to the strong interaction between the shock and the boundary layer, diminishes. This indicates that for some actuation frequencies, the strength of the buffet instability can be reduced, which in turn alleviates the intensity of the oscillating shear layer separation. This is also indicated by reduced pressure differentials close to the trailing edge as can be seen in figure 8.13-a in the region close to the trailing edge ($x/c > 0.9$).

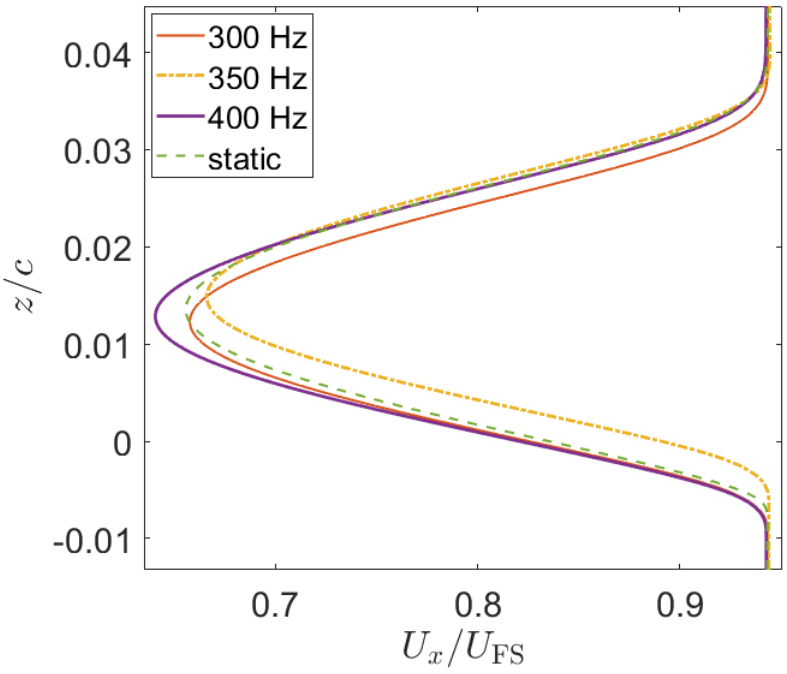

Figure 8.14: Time-averaged velocity profiles in the wake at a distance of x/c = 1.26 from the leading edge.

	300 Hz	350 Hz	400 Hz
$100 \times \Delta Z / Z_{static}$ (in %)	-2.9	-6.1	+0.6

Table 8.3: Variation of the wake width compared to the static case in three morphing configurations: an actuation frequency of 300 Hz; 350 Hz and 400 Hz. A positive number means that the wake width has increased, and a negative number signifies a width reduction. The extremal coordinates z_1 and z_2 that define the wake width $Z = \max(z_1, z_2) - \min(z_1, z_2)$ were chosen based on the criterion $U_x(z_1) = U_x(z_2) = 0.9 \times U_{FS}$ along a constant position $x/c = 1.26$; U_x being the longitudinal component of the velocity field and U_{FS} being the free-stream velocity magnitude.

As a result, since the shock strength is lessened and the instability is dampened by the action of suitable trailing edge vibrations, the shear layer becomes less separated on average and the wake becomes thinner.

This was shown by plotting the time-averaged velocity profiles in the wake and visualizing the flow.

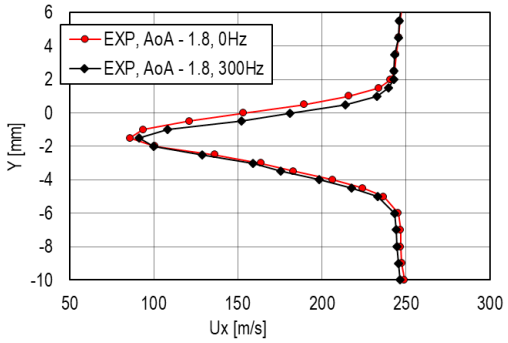

Figure 8.15: Time-averaged velocity profiles taken in the wake at a distance of $x/c = 1.05$ as measured from the leading edge ($x/c = 0$ being the position of the leading edge and $x/c = 1$ being the position of the trailing edge).

As can be seen in figure 8.14, the thickness of the wake at a given longitudinal position in the wake varies with the frequency of actuation. In the case of an actuation frequency of 400 Hz, the wake width increases (cf. figure 8.14 and table 8.3) which coincides with the observation made regarding the increased pressure differential between the suction side and pressure side close to the trailing edge (cf. figure 8.13), which indicates thicker shear layers and

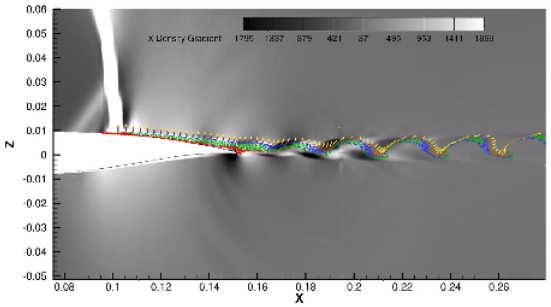

(a) (a)

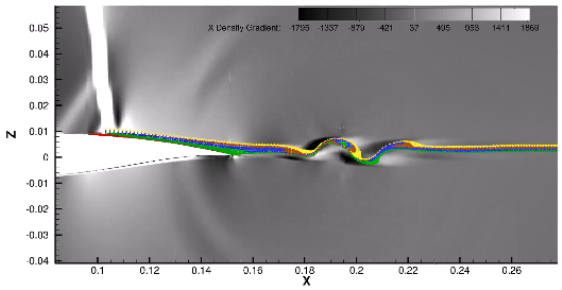

(b) (b)

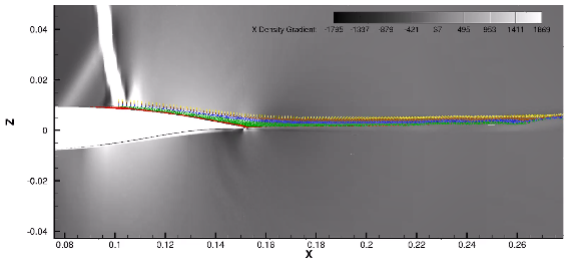

(c) (c)

Figure 8.16: Three instantaneous snapshots captured from animations post-processed from numerical calculations at three actuation frequencies: 200 Hz (a), 400 Hz (b) and 350 Hz (c).

more intense separation. This causes, for both 200 Hz and 400 Hz, the shear layer to destabilize more easily (figure 8.16-a,b) while numerical simulations performed at an actuation frequency of 300 Hz for instance show weaker wake and boundary layer instabilities, which can be seen in figure 8.16-c.

Similarly, the same trend has been observed in wind tunnel experiments.

Indeed, figure 8.15 demonstrates that a similar qualitative behavior is obtained compared to the numerical simulations, which is that a trailing edge vibration performed at a frequency of 300 Hz causes a reduction in wake thickness by diminishing the strength of the shock-wave/boundary layer interaction, limiting transient boundary layer separation and hence decreasing pressure drag. The wake width is measured via a Laser Doppler Anenometry technique that extracts the velocity field at regular locations along a laser sheet normal to the direction of the flow, illuminating the flow at a fixed location $x/c = 1.05$ in the wake. This measurement is achieved via an array of sensors that measure Doppler shifts from laser beams scattered by oncoming fluid particles which allows the device to deduce the value of the velocity at a certain location within the flow. Measurements show that wake width decreases by 4.7 % when a vibration at 300 Hz is applied compared to the static case.

Conclusion

This article presents a joint numerical and experimental study of the phenomena through which trailing edge morphing can act on compressibility effects in the transonic regime which result in strong interactions between shock-waves and boundary layers. This allows not only to reduce the risk of coupling between unsteady aerodynamic instabilities and structural modes that are detrimental to flight stability and structural resistance. This also allows to reduce aerodynamic drag and increase lift to drag ratio in a flight phase where these improvements are crucial since cruise is the most lasting phase of a commercial flight. The potential for diminished fuel consumption is an interesting prospect due to the fact that wing morphing performed via trailing edge vibrations as designed in our research group requires lightweight technology and non-invasive implementation methods compared to more conventional electric or hydraulic systems.

Both numerical results and experimental measures have exhibited the presence of a lock-in effect that underlies feedback processes which allow information to be transmitted back from the trailing edge towards the leading edge. In particular, pressure disturbances have been shown to act on the shock foot which reduces the amplitude of buffet and consequently diminishes the extent of boundary layer separation on average. This has the effect of

decreasing the pressure difference between the suction side and pressure side of the wing profile and thins down the turbulent wake, effectively reducing pressure drag. Both computations and wind tunnel tests have showcased similar results in terms of time-averaged force improvements and qualitative aspects such as the extent to which the wake thickness is reduced show strong similarities.

A better understanding still of the feedback mechanisms that alleviate the SWBLI will enable the design of a feedback controller loop to actuate the trailing edge optimally in regard to this flow regime. This has the potential to save more energy and improve aerodynamic coefficients even more. Ongoing three-dimensional computations are under realisation to help deepen and broaden the understanding of this feedback phenomenon.

Acknowledgements

The authors are grateful to the LAPLACE Laboratory GREM3 research group on electrodynamics and to the National Supercomputing centers CALMIP, CINES, IDRIS and TGCC for the allocation of computational resources, as well as the PRACE supercomputing allocation number 2017174208. This study has been realised under the H2020 European Research programme number 723402 : SMS, « Smart Morphing and Sensing for aeronautical configurations »[2]

References

Barbut, G. et al. (2010). "Prediction of transonic buffet around a wing with flap". In: *Notes on Numerical Fluid Mechanics and Multidisciplinary Design* 111, pp. 191–204. ISSN: 16122909. DOI: 10.1007/978-3-642-14168-3_16.

Bonne, Nicolas (2018). "Stabilité de l'interaction onde de choc/couche limite laminaire". PhD thesis.

[2] http://smartwing.org/SMS/EU

Bouhadji, A and M Braza (2003). "Organised modes and shock–vortex interaction in unsteady viscous transonic flows around an aerofoil: Part II: Reynolds number effect". In: *Computers & Fluids* 32.9, pp. 1261–1281. ISSN: 0045-7930. DOI: 10.1016/S0045-7930(02)00101-9.

Bourdet, S. et al. (2003). "Direct Numerical Simulation of the Three-Dimensional Transition to Turbulence in the Transonic Flow around a Wing". In: *Flow, Turbulence and Combustion (formerly Applied Scientific Research)* 71.1-4, pp. 203–220. ISSN: 1386-6184. DOI: 10.1023/B:APPL.0000014932.28421.9e.

Bourguet, R. et al. (2008). "Anisotropic Organised Eddy Simulation for the prediction of non-equilibrium turbulent flows around bodies". In: *Journal of Fluids and Structures* 24.8, pp. 1240–1251. ISSN: 08899746. DOI: 10.1016/j.jfluidstructs.2008.07.004.

Bourguet, R. et al. (2009). "Physical Analysis of an Anisotropic Eddy-Viscosity Concept for Strongly Detached Turbulent Unsteady Flows". In: *IUTAM Bookseries* 14, pp. 381–393. ISSN: 18753493. DOI: 10.1007/978-1-4020-9898-7_33.

Bradshaw, P. (Oct. 1973). *Effects of Streamline Curvature on Turbulent Flow.* Imperial College of Science and Technology.

Braza, M., R. Perrin, and Y. Hoarau (2006). "Turbulence properties in the cylinder wake at high Reynolds numbers". In: *Journal of Fluids and Structures* 22.6-7, pp. 757–771. ISSN: 08899746. DOI: 10.1016/j.jfluidstructs.2006.04.021.

Chinaud, M. et al. (2014). "Trailing-edge dynamics and morphing of a deformable flat plate at high Reynolds number by time-resolved PIV". In: *Journal of Fluids and Structures* 47, pp. 41–54. ISSN: 0889-9746. DOI: 10.1016/J.JFLUIDSTRUCTS.2014.02.007.

Deck, Sébastien (2005). "Numerical Simulation of Transonic Buffet over a Supercritical Airfoil". In: *AIAA Journal* 43.7, pp. 1556–1566. ISSN: 0001-1452. DOI: 10.2514/1.9885.

Doerffer, Piotr et al. (2010). "NACA0012 with Aileron (Marianna Braza)". In: pp. 101–131. DOI: 10.1007/978-3-642-03004-8_4.

Grossi, Fernando, Marianna Braza, and Yannick Hoarau (2014). "Prediction of Transonic Buffet by Delayed Detached-Eddy Simulation". In: *AIAA Journal* 52.10, pp. 2300–2312. ISSN: 0001-1452. DOI: 10.2514/1.J052873.

Hoarau, Yannick (Jan. 2002). "Analyse physique par simulation numérique et modélisation des écoulements décollés instationnaires autour de surfaces portantes". In: *http://www.theses.fr*.

Hunt, Julian C.R., Ian Eames, and Jerry Westerweel (2008). "Vortical interactions with interfacial shear layers". In: *Solid Mechanics and its Applications* 4, pp. 331–338. ISSN: 18753507. DOI: 10.1007/978-1-4020-6472-2_50.

Jacquin, L. et al. (2009). "Experimental Study of Shock Oscillation over a Transonic Supercritical Profile". In: *AIAA Journal* 47.9, pp. 1985–1994. ISSN: 0001-1452. DOI: 10.2514/1.30190.

Jacquin, Laurent et al. (2005). "An Experimental Study of Shock Oscillation over a Transonic Supercritical Profile". In: *35th AIAA Fluid Dynamics Conference and Exhibit*. Reston, Virigina: American Institute of Aeronautics and Astronautics. ISBN: 978-1-62410-059-8. DOI: 10.2514/6.2005-4902.

Jin, G and M Braza (1994). "Two-equation turbulence model for unsteady separated flows around airfoils". In: *AIAA Journal* 32.11, pp. 2316–2320. ISSN: 0001-1452. DOI: 10.2514/3.12292.

Jodin, G. et al. (2017). "Dynamics of a hybrid morphing wing with active open loop vibrating trailing edge by time-resolved PIV and force measures". In: *Journal of Fluids and Structures* 74, pp. 263–290. ISSN: 10958622. DOI: 10.1016/j.jfluidstructs.2017.06.015.

Lagrée, P. Y. (2010). "Interactive Boundary Layer (IBL)". In: *CISM International Centre for Mechanical Sciences, Courses and Lectures* 523, pp. 247–286. ISSN: 23093706. DOI: 10.1007/978-3-7091-0408-8_8.

Levy Jr., Lionel L. (1978). "Experimental and Computational Steady and Unsteady Transonic Flows about a Thick Airfoil". In: *AIAA Journal* 16.6, pp. 564–572. ISSN: 0001-1452. DOI: 10.2514/3.60935.

Marvin, J G, L L Levy Jr., and H L Seegmiller (1980). "Turbulence Modeling for Unsteady Transonic Flows". In: *AIAA Journal* 18.5, pp. 489–496. ISSN: 0001-1452. DOI: 10.2514/3.50782.

McDevitt, John B., Lionel L. Levy Jr., and George S. Deiwert (1976). "Transonic Flow about a Thick Circular-Arc Airfoil". In: *AIAA Journal* 14.5, pp. 606–613. ISSN: 0001-1452. DOI: 10.2514/3.61402.

Perrin, Rodolphe (Jan. 2005). "Analyse physique et modélisation d'écoulements incompressibles instationnaires turbulents autour d'un cylindre circulaire à grand nombre de Reynolds". In: *http://www.theses.fr*. URL: http://www.theses.fr/2005INPT016H.

Scheller, J. et al. (2015). "Trailing-edge dynamics of a morphing NACA0012 aileron at high Reynolds number by high-speed PIV". In: *Journal of*

Fluids and Structures 55, pp. 42–51. ISSN: 10958622. DOI: 10.1016/j.jfluidstructs.2014.12.012.

Scheller, Johannes (2015). "Electroactive morphing for the aerodynamic performance improvement of next generation airvehicles". PhD thesis.

Seegmiller, H. L., J. G. Marvin, and L. L. Levy (1978). "Steady and unsteady transonic flow". In: *AIAA Journal* 16.12, pp. 1262–1270. ISSN: 00011452. DOI: doi:10.2514/6.1978-160.

Szubert, Damien (2015). "Physics and modelling of unsteady turbulent flows around aerodynamic and hydrodynamic structures at high Reynold number by numerical simulation". In.

Szubert, Damien et al. (2015a). "Numerical study of the turbulent transonic interaction and transition location effect involving optimisation around a supercritical aerofoil". In: *European Journal of Mechanics - B/Fluids* 55, pp. 380–393. ISSN: 09977546. DOI: 10.1016/j.euromechflu.2015.09.007.

Szubert, Damien et al. (2015b). "Shock-vortex shear-layer interaction in the transonic flow around a supercritical airfoil at high Reynolds number in buffet conditions". In: *Journal of Fluids and Structures* 55, pp. 276–302. ISSN: 10958622. DOI: 10.1016/j.jfluidstructs.2015.03.005.

Tô, J.-B. et al. (2019). "Effects of vibrating and deformed trailing edge of a morphing supercritical airfoil in transonic regime by numerical simulation at high Reynolds number". In: *Journal of Fluids and Structures*. ISSN: 0889-9746. DOI: 10.1016/J.JFLUIDSTRUCTS.2019.02.011.

Chapter 9

Conclusion

This study was carried out in the context of the H2020 European research program n° 723402 "Smart Morphing and Sensing for aeronautical configurations" aiming to improve aerodynamic performance in all phases of flight. It focuses on an investigation of the Shock Wave Boundary Layer Interaction (SWBLI) dynamics in cruise flight, and how trailing edge morphing as a novel actuation method can reduce the strength of the interaction through feedback effects. The study aimed to describe the flow physics of such an interaction and to understand how the studied morphing concepts influence the time-averaged aerodynamic forces and their rms values.

This study was based on the generation of statistically stationary CFD results by employing advanced turbulence modelling methods which take into account the highly organized structure of turbulence in these flow regimes. Two-dimensional calculations were deemed more cost-efficient and were preferred to enable a comprehensive and large parametric analysis based on the trailing edge flapping frequency. Therefore, optimal vibration and amplitude ranges have been identified, enabling the selection of optimal actuation frequencies in the related experiments of the SMS project regarding the tRS-"transonic Reduced Scale" prototype, carried out by the partner IMP-PAN in Gdańsk. Moreover, the assessment of the optimal ranges by the present simulations opened the possibility of performing 3D High-Fidelity simulations in ongoing studies of our research group, by narrowing the range of the parameters to be tested in highly costly 3D simulations. Besides, the 2D approach used for the simulations in the present study was enforced by concomitant three-dimensional studies in the subsonic flight phases which

showed that trailing edge vibrations in similar frequency ranges result in a suppression of spanwise 3D instabilities. They also lead to a practically bi-dimensional wake structure encompassing the main coherent eddies, a result that was highlighted in the thesis of A. Marouf, 2020.

In the present thesis, a detailed analysis of the SWBLI and its impact on the pressure distribution and the aerodynamic forces has been discussed for the two actuation frequency ranges, $700 - 730$ and $300 - 400$ and have allowed isolating two optimal cases: The study around 720 Hz found that no other actuation frequency in that range performed as well as 720 Hz which remains the optimal case for this panel of frequencies. This frequency also provides a drag reduction of the order of 5% and a lift-to-drag increase of the order of 3%. Between 350 Hz and 400 Hz, a new optimum has been found at a frequency of 365 Hz, leading to a drag reduction of nearly 10% as well as a lift-to-drag increase of roughly 6%. These improvements of aerodynamic performance are quite significant in the cruise phase, which is the most lasting flight phase for a common mid-range or long-range commercial aircraft. Therefore, a significant fuel consumption decrease can be achieved.

Comparing the two frequency ranges, it appears that the optimum at 365 Hz gives better results than 720 Hz in terms of drag and lift to drag ratio. Although lift is decreased in the case of an actuation performed at 365 Hz compared to 720 Hz, the significant drag reduction and the improvement in regards to the lift to drag ratio mean that morphing could be applied in the cruise phase as a disruptive technology to modify the operating point and flight levels without negatively impacting fuel consumption.

It has been shown that certain actuation frequencies such as 365 Hz manage to significantly reduce the wake width via a feedback loop. Indeed, by imposing pressure fluctuations at a frequency that is a multiple of the buffet frequency, it is possible to alleviate the amplitude of the SWBLI, reduce the shock strength and consequently diminish the extent of the boundary layer separation over the suction side of the wing. This manipulation takes advantage of the so-called lock-in effect that was observed in this study, where the shock motion can be made to synchronize with either the frequency of actuation if the latter is close enough to the natural frequency of buffet, or to a sub-harmonic of the actuation frequency.

A direct consequence of this wake thickness shrinkage is the reduction of

shape drag caused by the extension of the separated boundary layer. Another consequence is that the shock is slightly weakened and the associated wave drag is diminished.

It can also be noted that lower actuation frequencies are more easily reachable by current technology. It follows that carrying out trailing edge morphing at 365 Hz is more realistic and energy-efficient than doing so at 720 Hz.

Finally, it has been proved that it is possible to control the frequency of buffet and the amplitude of this unsteady mode through trailing edge vibrations ensured by using the piezoelectric actuators that were studied in the SMS project.

Such results have been observed experimentally as well, which helps corroborate the mechanisms hereby described.

This means that trailing edge morphing has the potential to reduce the likelihood of a resonance between this global flow instability and wing vibrational modes. It can also reduce drag in cruise flight by a manipulation of the SWBLI via a transfer of information that travels upstream towards the shock foot along the separated boundary layer and through the inviscid region of the flow.

The present study has shown the existence and quantified the *feedback effect* carrying pressure disturbances from the shear layers and near wake unsteadingess towards the SWBLI and act on the buffet mode by influencing the region that precedes the shock. This effect can influence the whole flow around the wing, leading up to a variety of outlooks regarding the enhancement of aerodynamic performance, buffet manipulation and suppression through a closed-loop control.

Perspectives

From the conclusions of the present study, novel actuation approaches can be developed. Trailing edge actuations have proved to be efficient in controlling SWBLIs through a feedback effect, by inducing disturbances that can travel upstream along the boundary layer, ultimately reaching a zone that precedes the shock foot. By manipulating strategic parts of the wing at a mesoscopic

level with emphasis in regions aft the shock foot, it could be possible to reach an enhanced level of control on flow features within the boundary layer.

Electro-active skin design

By drawing inspiration from the maneuverability of sharks and manta rays, the very efficient swimming of moon jellyfish and the aerodynamics of birds, a live "shark skin" made of small electro-active actuators can be developed in order to reduce friction drag while simultaneously decreasing aerodynamic noise generation and increasing lift.

Such an apparatus would be constituted of small structures or shells that resemble shark scales. Each of them would be actuated so as to rotate upwards or remain flat along the skin at any moment in order to influence the distribution of eddies in the laminar layer or inertial range of the turbulent boundary layer. By interacting with the sheared flow within the boundary layer and shear layers, the scales create tiny vortices very close to the wall along the spanwise direction which act as a lubricant and contribute to decrease friction drag.

Additionally, it can be possible to modify the structure of turbulence within strongly separated boundary layers through the usage of these morphing concepts.

By drawing on the findings of the present study, the scales can be made to reduce the strength of coherent eddies that result from the destabilization of highly sheared or strongly separated boundary layers. This in turn would influence the transfer of energy from these organized structures towards the chaotic background of turbulence within shear layers or far downstream in the wake. This would result in reduced form/shape drag as well as diminished friction drag, while allowing the prospect of being able to increase lift since the electro-active shells would be able to inject momentum within the turbulent boundary layer to keep it attached at higher angles of incidence.

RELATED PUBLICATIONS AND CONTRIBUTIONS

The present thesis took part in the following scientific dissemination activities and large public communication activities

Publications in Peer-Reviewed Journals

1. Tô J.-B., Simiriotis N., Marouf A., Szubert D., Ioannis A., Zilli D.M., Hoarau Y., Hunt J.C.R., Braza M.
   Effects of vibrating and deformed trailing edge of a morphing supercritical airfoil in transonic regime by numerical simulation at high Reynolds number
   Journal of Fluids, Structures, vol. 91, 2019, 102595

2. Marouf A., Bmegaptche Tekap Y., Simiriotis N., Tô J.-B., Rouchon J.-F., Hoarau Y., Braza M.
   Numerical investigation of frequency-amplitude effects of dynamic morphing for a high-lift configuration at high Reynolds number
   International Journal of Numerical Methods for Heat & Fluid Flow, vol. 31, 2019, https://doi.org/10.1108/HFF-07-2019-0559

Publications in Books after International Conferences

1. Tô J.-B., Zilli D.M., Simiriotis N., Asproulias I., Szubert D., Marouf A., Hoarau Y., Braza M. *Numerical Simulation, Modelling of a Mor-*

phing Supercritical Airfoil in a Transonic Flow at High Reynolds Numbers In book: Advances in Critical Flow Dynamics Involving Moving/Deformable Structures with Design Applications (pp.371-384), 2021

2. Marouf A., Simiriotis N., Tô J.-B., Bmegaptche Tekap Y., Hoarau Y., Braza M. *DDES and OES Simulations of a Morphing Airbus A320 Wing and Flap in Different Scales at High Reynolds* Progress in Hybrid RANS-LES Modelling (pp. 246-258)

3. Marouf A., Simiriotis N., Tô J.-B., Carvalho M., Bmegaptche Y., Kitouni A., Hoarau Y., Rouchon J.-F., Braza M. *Smart Morphing and Sensing for the Wings of the Future* Invited Special Technology Session STS17, January 2021, Publisher Springer, in print.

Articles in International Conferences

1. Tô J.-B., Bhardwaj N., Simiriotis N., Marouf A., Hoarau Y., Hunt J.C.R., Braza M.
Manipulation of a Shock-Wave/Boundary-Layer Interaction in the Transonic Regime Around a Supercritical Morphing Wing
Symposium on Fluid-Structure-Sound Interactions and Control, 2019

2. Marouf A., Tô J.-B., Simiriotis N., Charbonnier D., Vos J.B., Hoarau Y., Braza M.
Aerodynamic Performance Increase of a Morphing A320 Wing with HighLift Flap by Means of Hi-Fi CFD Approaches
14th World Congress in Computational Mechanics (WCCM) ECCOMAS Congress, 2021

3. Bmegaptche Tekap Y., Jodin G., Marouf A., Tô J.-B., Harran G., Rouchon J.-F., Braza M. *Wind tunnel experimental investigation of an electroactive morphing high-lift flap on a two-element wing in subsonic speeds* IUTAM 2018, Critical flow dynamics involving moving/deformable structures with design applications, 2018

Publication in Data Paper for open science

1. Tô J.-B., Louge T., Rouaix C., Jiménez Navarro C., Marouf A., Braza M. *Aerodynamic performance in transonic regime around an A320 airfoil by means of electroactive morphing through vibration and slight deformation of the near-trailing edge region at high Reynolds number* Datapaper, 2021,
DOI:10.48531/JBRU.CALMIP/19XGRY/VBS4DK

Scientific dissemination

I also took part in a number of forums to showcase our research within the SMS project and share it with the public:

1. The Day of Science – Toulouse,France,2017.

2. ILA Berlin forum — Berlin,Germany,2018: First technological exhibition of the subscale model with fully-integrated electronics.

3. TRA Vienna forum -– Vienna,Austria,2018.

4. « Rapaces » exhibition on birds of prey — Toulouse, France, 2018. An actuated wing prototype was displayed to show the biological inspirations of the H2020 SMS EU project: http://smartwing.org/SMS/EU/.

5. « Salon du Bourget » – Paris, France, 2019.

6. « Science is wonderful ! » – Brussels,Belgium,2019.

International conferences

1. IUTAM Symposium on Critical Flow dynamics around moving/deformable structures with design applications, Santorini, Greece, 2018.

2. 8th EASN-CEAS Internation Workshop on Manufacturing for Growth & Innovation – Glasgow, Scotland, 2018.

3. FSSIC Symposium – Chania, Crete Island, Greece, 2019.

4. 9th EASN International Conference on innovation in Aviation & Space – Athens, Greece, 2019.

5. 10th EASN Virtual Invernational Conference, 2020.

6. 14th WCCM & ECCOMAS Virtual Congress, 2021.

Tutoring work

My tutoring activities during the thesis consisted in :

1. Tutoring of three « TIPE » school projects led by "classes préparatoires" students researching biomimetics.

2. Tutoring of the « Bureau d'Etudes Industrielles » (BEI) : Masters degree final project conducted by ENSEEIHT students before their final year internship – 2018, 2019, 2020, 2021.

3. Tutoring classes in ENSEEIHT in Probability theory, Statistics, numerical methods for solving PDEs, the Fourier transform, coding in Fortran, etc. during three consecutive years : 2017-2018 ; 2018-2019 ; 2019-2020.

Bibliography

Ayton, Lorna J, J R Gill, and N Peake (2016). "The Importance of the Unsteady Kutta Condition when Modelling Gust-Aerofoil Interaction". In.

Babinsky, H. and J. K. Harvey (2011). *Shock Wave-Boundary Layer Interactions*. ISBN: 9780521848527.

Barbut, G. et al. (2010). "Prediction of transonic buffet around a wing with flap". In: *Notes on Numerical Fluid Mechanics and Multidisciplinary Design* 111, pp. 191–204. ISSN: 16122909. DOI: 10.1007/978-3-642-14168-3_16.

Bock, Walter J. (Aug. 2000). "Explanatory History of the Origin of Feathers". In: *Integrative and Comparative Biology* 40 (4), pp. 478–485. ISSN: 1540-7063. DOI: 10.1093/ICB/40.4.478.

Bonne, Nicolas (2018). "Stabilité de l'interaction onde de choc/couche limite laminaire". PhD thesis.

Bouhadji, A and M Braza (2003). "Organised modes and shock–vortex interaction in unsteady viscous transonic flows around an aerofoil: Part II: Reynolds number effect". In: *Computers & Fluids* 32.9, pp. 1261–1281. ISSN: 0045-7930. DOI: 10.1016/S0045-7930(02)00101-9.

Bourdet, S. et al. (2003). "Direct Numerical Simulation of the Three-Dimensional Transition to Turbulence in the Transonic Flow around a Wing". In: *Flow, Turbulence and Combustion (formerly Applied Scientific Research)* 71.1-4, pp. 203–220. ISSN: 1386-6184. DOI: 10.1023/B:APPL.0000014932.28421.9e.

Bourguet, R. et al. (2008). "Anisotropic Organised Eddy Simulation for the prediction of non-equilibrium turbulent flows around bodies". In: *Journal of Fluids and Structures* 24.8, pp. 1240–1251. ISSN: 08899746. DOI: 10.1016/j.jfluidstructs.2008.07.004.

Bourguet, R. et al. (2009). "Physical Analysis of an Anisotropic Eddy-Viscosity Concept for Strongly Detached Turbulent Unsteady Flows". In: *IUTAM Bookseries* 14, pp. 381–393. ISSN: 18753493. DOI: 10.1007/978-1-4020-9898-7_33.

Bradshaw, P. (Sept. 1967). "The turbulence structure of equilibrium boundary layers". In: *Journal of Fluid Mechanics* 29 (4), pp. 625–645. ISSN: 1469-7645. DOI: 10.1017/S0022112067001089.

— (Oct. 1973). *Effects of Streamline Curvature on Turbulent Flow.* Imperial College of Science and Technology.

Braza, M., R. Perrin, and Y. Hoarau (2006). "Turbulence properties in the cylinder wake at high Reynolds numbers". In: *Journal of Fluids and Structures* 22.6-7, pp. 757–771. ISSN: 08899746. DOI: 10.1016/j.jfluidstructs.2006.04.021.

Braza, M et al. (2006). "Turbulence modelling improvement for highly detached unsteady aerodynamic flows by statistical and hybrid approaches". In: *ECCOMAS CFD 2006 : European Conference on Computational Fluid Dynamics, September 5-8, 2006* September.

Brown, Garry L. and Anatol Roshko (1974). "On density effects and large structure in turbulent mixing layers". In: *Journal of Fluid Mechanics* 64 (4), pp. 775–816. ISSN: 1469-7645. DOI: 10.1017/S002211207400190X.

Bruce, P. J.K. and S. P. Colliss (2015). "Review of research into shock control bumps". In: *Shock Waves* 25.5, pp. 451–471. ISSN: 09381287. DOI: 10.1007/s00193-014-0533-4.

Brutyan, M., A. Petrov, and A. V. Potapchik (2016). "New Method of Transonic Buffet Decreasing on Supercritical Airfoil". In.

Cantwell, Brian and Donald Coles (1983). "An experimental study of entrainment and transport in the turbulent near wake of a circular cylinder". In: *Journal of Fluid Mechanics* 136, pp. 321–374. ISSN: 14697645. DOI: 10.1017/S0022112083002189.

Chien, Kuei-Yuan (May 1982). "Predictions of Channel and Boundary-Layer Flows with a Low-Reynolds-Number Turbulence Model". In: *https://doi.org/10.2514/3.51043* 20 (1), pp. 33–38. DOI: 10.2514/3.51043.

Chinaud, M. et al. (2012). "Thermo-mechanical coupling in Nitinol. Application to an electro-morphing plate". In: *Proceedings - 2012 20th International Conference on Electrical Machines, ICEM 2012*, pp. 2580–2584. DOI: 10.1109/ICELMACH.2012.6350249.

Chinaud, M. et al. (2014). "Trailing-edge dynamics and morphing of a deformable flat plate at high Reynolds number by time-resolved PIV". In: *Journal of Fluids and Structures* 47, pp. 41–54. ISSN: 0889-9746. DOI: 10.1016/J.JFLUIDSTRUCTS.2014.02.007.

Corrsin, S. (1943). "Investigation of Flow in an Axially Symmetrical Heated Jet of Air". In: *undefined*.

Davis, Sanford S and Gerald N Malcolmf (1980). "Transonic Shock-Wave / Boundary-Layer Interactions on an Oscillating Airfoil". In: *AIAA Journal* 18.11, pp. 1306–1312.

Deck, Sébastien (2005). "Numerical Simulation of Transonic Buffet over a Supercritical Airfoil". In: *AIAA Journal* 43.7, pp. 1556–1566. ISSN: 0001-1452. DOI: 10.2514/1.9885.

Djeridi, H. et al. (2003). "Near-Wake Turbulence Properties around a Circular Cylinder at High Reynolds Number". In: *Flow, Turbulence and Combustion* 71 (1-4), pp. 19–34. DOI: 10.1023/B:APPL.0000014930.49408.53.

Doerffer, Piotr et al. (2010). "NACA0012 with Aileron (Marianna Braza)". In: pp. 101–131. DOI: 10.1007/978-3-642-03004-8_4.

Délery, J. M. (2001). "Shock Wave/Boundary Layer Interactions". In: *Handbook of Shock Waves*, pp. 205–I. DOI: 10.1016/B978-012086430-0/50024-5.

Frey, Manuel (1998). "Shock Patterns in the Plume of Overexpanded Rocket Nozzles". In: ed. by ESA SP R. A. Harris. Paris: European Space Agency (ESA), 1999, pp. 395–402. ISBN: 9290927046.

Frisch, U. (Uriel) and A. N. (Andrei Nikolaevich) Kolmogorov (1995). "Turbulence : the legacy of A.N. Kolmogorov". In: p. 296.

Gadd, G. E. (1958). "Interactions between shock waves and boundary layers". In: *Grenzschichtforschung / Boundary Layer Research*, pp. 239–255. DOI: 10.1007/978-3-642-45885-9_20.

Gageik, M. et al. (2018). "Pressure wave damping in transonic airfoil flow by means of micro vortex generators". In: *Aerospace Science and Technology* 81.M, pp. 65–77. ISSN: 12709638. DOI: 10.1016/j.ast.2018.05.011.

Geyer, T., E. Sarradj, and C. Fritzsche (2014). "Measuring owl flight noise". In: *undefined*.

Giannelis, Nicholas F., Oleg Levinski, and Gareth A. Vio (July 2018). "Influence of Mach number and angle of attack on the two-dimensional transonic buffet phenomenon". In: *Aerospace Science and Technology* 78, pp. 89–101. ISSN: 12709638. DOI: 10.1016/J.AST.2018.03.045.

Godefroit, Pascal et al. (Jan. 2013). "Reduced plumage and flight ability of a new Jurassic paravian theropod from China". In: *Nature Communications 2013 4:1* 4 (1), pp. 1–6. ISSN: 2041-1723. DOI: 10.1038/ncomms2389.

Grossi, Fernando, Marianna Braza, and Yannick Hoarau (2014). "Prediction of Transonic Buffet by Delayed Detached-Eddy Simulation". In: *AIAA Journal* 52.10, pp. 2300–2312. ISSN: 0001-1452. DOI: 10.2514/1.J052873.

Hartmann, A., A. Feldhusen, and W. Schröder (2013). "On the interaction of shock waves and sound waves in transonic buffet flow". In: *Physics of Fluids* 25.2. ISSN: 10706631. DOI: 10.1063/1.4791603.

Heerenbrink, Marco Klein and Anders Hedenström (Feb. 2017). "Wake analysis of drag components in gliding flight of a jackdaw (Corvus monedula) during moult". In: *Interface Focus* 7 (1). DOI: 10.1098/RSFS.2016.0081.

Heerenbrink, Marco Klein, L. Christoffer Johansson, and Anders Hedenström (May 2017). "Multi-cored vortices support function of slotted wing tips of birds in gliding and flapping flight". In: *Journal of the Royal Society Interface* 14 (130). DOI: 10.1098/RSIF.2017.0099.

Hetrick, Joel A. et al. (2007). "Flight testing of Mission Adaptive Compliant Wing". In: *Structural Dynamics and Materials Conference* 1, pp. 92–109. DOI: 10.2514/6.2007-1709.

Hoarau, Y. (2016). *Turbulence Models Description*.

Hoarau, Yannick (Jan. 2002). "Analyse physique par simulation numérique et modélisation des écoulements décollés instationnaires autour de surfaces portantes". In: *http://www.theses.fr*.

Hoarau, Yannick et al. (2016). "Recent Developments of the Navier Stokes Multi Block (NSMB) CFD solver". In: *54th AIAA Aerospace Sciences Meeting*. AIAA SciTech Forum. American Institute of Aeronautics and Astronautics. DOI: doi:10.2514/6.2016-2056.

Hunt, Julian C.R., Ian Eames, and Jerry Westerweel (2008). "Vortical interactions with interfacial shear layers". In: *Solid Mechanics and its Applications* 4, pp. 331–338. ISSN: 18753507. DOI: 10.1007/978-1-4020-6472-2_50.

Jacquin, L. et al. (2009). "Experimental Study of Shock Oscillation over a Transonic Supercritical Profile". In: *AIAA Journal* 47.9, pp. 1985–1994. ISSN: 0001-1452. DOI: 10.2514/1.30190.

Jacquin, Laurent et al. (2005). "An Experimental Study of Shock Oscillation over a Transonic Supercritical Profile". In: *35th AIAA Fluid Dynamics Conference and Exhibit*. Reston, Virigina: American Institute of Aeronau-

tics and Astronautics. ISBN: 978-1-62410-059-8. DOI: 10.2514/6.2005-4902.

Jaworski, Justin W. and N. Peake (Jan. 2020). "Aeroacoustics of Silent Owl Flight". In: *Annual Review of Fluid Mechanics* 52, pp. 395–420. DOI: 10.1146/ANNUREV-FLUID-010518-040436.

Jin, G and M Braza (1994). "Two-equation turbulence model for unsteady separated flows around airfoils". In: *AIAA Journal* 32.11, pp. 2316–2320. ISSN: 0001-1452. DOI: 10.2514/3.12292.

Jodin, G. et al. (2017). "Dynamics of a hybrid morphing wing with active open loop vibrating trailing edge by time-resolved PIV and force measures". In: *Journal of Fluids and Structures* 74, pp. 263–290. ISSN: 10958622. DOI: 10.1016/j.jfluidstructs.2017.06.015.

Jones, W.P. and B.E. Launder (1972). "The Prediction of Laminarization with a Two-Equation Model of Turbulence." In: *Int. J. of Heat and Mass Transfer* vol. 15, p. 301.

Kaul, Upender K and Nhan T Nguyen (2014). "Drag Optimization Study of Variable Camber Continuous Trailing Edge Flap (VCCTEF) Using OVERFLOW". In: ISSN: 2014-2444. DOI: 10.2514/6.2014-2444.

Kolmogorov, A. N. (July 1991). "The local structure of turbulence in incompressible viscous fluid for very large Reynolds numbers". In: *Proceedings of the Royal Society of London. Series A: Mathematical and Physical Sciences* 434 (1890), pp. 9–13. DOI: 10.1098/RSPA.1991.0075.

König, Benedikt et al. (2009). "Numerical and Experimental Validation of Three-Dimensional Shock Control Bumps". In: *Journal of Aircraft* 46.2, pp. 675–682. ISSN: 0021-8669. DOI: 10.2514/1.41441.

Kundu, P. K., I. M. Cohen, and D. R. Dowling (2012). "Compressible Flow". In: *Fluid Mechanics*, pp. 729–778. DOI: 10.1016/B978-0-12-382100-3.10015-0.

Kunz, R.F. and B. Lakshminarayana (1992). "Stability of explicit Navier-Stokes Procedures using k-epsilon algebraic Reynolds Stress Turbulence Models". In: *J. of Computational Physics* 103, pp. 141–159.

Lagrée, P. Y. (2010). "Interactive Boundary Layer (IBL)". In: *CISM International Centre for Mechanical Sciences, Courses and Lectures* 523, pp. 247–286. ISSN: 23093706. DOI: 10.1007/978-3-7091-0408-8_8.

Lee, B. H. K., H. Murty, and H. Jiang (1994). "Role of Kutta waves on oscillatory shock motion on an airfoil". In: *AIAA Journal* 32.4, pp. 789–796. ISSN: 0001-1452. DOI: 10.2514/3.12054.

Lee, Sang Im et al. (May 2015). "The function of the alula in avian flight". In: *Scientific Reports* 5. DOI: 10.1038/SREP09914.

Leer, Bram van (1979). "Towards the ultimate conservative difference scheme. V. A second-order sequel to Godunov's method". In: *Journal of Computational Physics* 32 (1), pp. 101–136. ISSN: 10902716. DOI: 10.1016/0021-9991(79)90145-1. URL: https://www.researchgate.net/publication/285599602_Towards_the_Ultimate_Conservative_Difference_Scheme_V_A_Second-order_Sequel_to_Godunov's_Method.

Levy Jr., Lionel L. (1978). "Experimental and Computational Steady and Unsteady Transonic Flows about a Thick Airfoil". In: *AIAA Journal* 16.6, pp. 564–572. ISSN: 0001-1452. DOI: 10.2514/3.60935.

Liu, Xiao, Hasan Kamliya Jawahar, and Mahdi Azarpeyvand (2016). "Wake development of airfoils with serrated trailing edges". In: *22nd AIAA-CEAS Aeroacoustics Conference*. DOI: 10.2514/6.2016-2817.

Marouf, Abderahmane (Oct. 2020). "Analyse physique de concepts du morphing électroactif pour accroître les performances aérodynamiques des ailes du futur par simulation numérique de Haute Fidélité et modélisation de la Turbulence à nombre de Reynolds élevé". In: *http://www.theses.fr*.

Marvin, J. G., L L Levy Jr., and H. L. Seegmiller (1979). "Aerospace Sciences Meeting". In: *Physics*. DOI: Doi10.1109/Icsssm.2006.320779.

Marvin, J G, L L Levy Jr., and H L Seegmiller (1980). "Turbulence Modeling for Unsteady Transonic Flows". In: *AIAA Journal* 18.5, pp. 489–496. ISSN: 0001-1452. DOI: 10.2514/3.50782.

McDevitt, John B., Lionel L. Levy Jr., and George S. Deiwert (1976). "Transonic Flow about a Thick Circular-Arc Airfoil". In: *AIAA Journal* 14.5, pp. 606–613. ISSN: 0001-1452. DOI: 10.2514/3.61402.

McGowan, Anna-Maria Rivas et al. (July 2002). "Recent results from NASA's morphing project". In: *https://doi.org/10.1117/12.475056* 4698, pp. 97–111. DOI: 10.1117/12.475056.

Méndez, B and R Gutiérrez (2018). "Non-conventional vortex generators calculated with CFD". In: p. 22029. DOI: 10.1088/1742-6596/1037/2/022029.

Nguyen, Nhan T. et al. (2015). "Wind tunnel investigation of a flexible wing high-lift configuration with a variable camber continuous trailing edge flap design". In: *33rd AIAA Applied Aerodynamics Conference*. DOI: 10.2514/6.2015-2417.

Nishizawa, S et al. (2015). “Influence of grid aspect ratio on planetary boundary layer turbulence in large-eddy simulations”. In: *Geosci. Model Dev* 8, pp. 3393–3419. DOI: 10.5194/gmd-8-3393-2015.

Paladini, Edorado et al. (2019). “Transonic buffet instability: From two-dimensional airfoils to three-dimensional swept wings”. In: *Physical Review Fluids* 4.10, p. 103906. ISSN: 2469990X.

Perrin, Rodolphe (Jan. 2005). “Analyse physique et modélisation d’écoulements incompressibles instationnaires turbulents autour d’un cylindre circulaire à grand nombre de Reynolds”. In: *http://www.theses.fr*. URL: http://www.theses.fr/2005INPT016H.

Piponniau, Sébastien (2009). “Instationnarités dans les décollements compressibles : cas des couches limites soumises à ondes de choc”. In.

Ponitz, Benjamin, Michael Triep, and Christoph Brücker (2014). “Aerodynamics of the Cupped Wings during Peregrine Falcon’s Diving Flight”. In: *Open Journal of Fluid Dynamics* 04 (04), pp. 363–372. DOI: 10.4236/OJFD.2014.44027.

Ponitz, Benjamin et al. (Feb. 2014). “Diving-flight aerodynamics of a peregrine falcon (Falco peregrinus)”. In: *PLoS ONE* 9 (2). DOI: 10.1371/JOURNAL.PONE.0086506.

Qin, N. et al. (2000). “Active control of transonic aerodynamics using suction, blowing, bumps and synthetic jets”. In: *18th Applied Aerodynamics Conference*. DOI: 10.2514/6.2000-4329.

Ramaswamy, Deepak Prem and Anne Marie Schreyer (2021). “Control of shock-induced separation of a turbulent boundary layer using air-jet vortex generators”. In: *AIAA Journal* 59.3, pp. 927–939. DOI: 10.2514/1.J059674.

Rodes, Pascal (Jan. 1999). “Contribution à l’étude d’écoulements instationnaires transtionnels et turbulents autour d’une aile par simulation numérique et modélisation”. In: *http://www.theses.fr*.

Roger, Michel, Stéphane Moreau, and Korcan Kucukcoskun (2015). “On sound scattering by rigid edges and wedges in a flow, with applications to high-lift device aeroacoustics”. In: DOI: 10.1016/j.jsv.2015.10.004.

Scheller, J. et al. (2015). “Trailing-edge dynamics of a morphing NACA0012 aileron at high Reynolds number by high-speed PIV”. In: *Journal of Fluids and Structures* 55, pp. 42–51. ISSN: 10958622. DOI: 10.1016/j.jfluidstructs.2014.12.012.

Scheller, Johannes (2015). “Electroactive morphing for the aerodynamic performance improvement of next generation airvehicles”. PhD thesis.

Seegmiller, H. L., J. G. Marvin, and L. L. Levy (1978). "Steady and unsteady transonic flow". In: *AIAA Journal* 16.12, pp. 1262–1270. ISSN: 00011452. DOI: doi:10.2514/6.1978-160.

Shang, J. S., Jr. Hankey W. L., and C. H. Law (1976). "Numerical simulation of shock wave-turbulent boundary layer interaction". In: *aiaa*.

Spalart, P. R. et al. (1997). "Comments on the feasibility of LES for wings and on a hybrid RANS/LES approach". In: *Advances in DNS/LES* 1.JANUARY, pp. 4–8.

Speziale, Charles G. (Sept. 1998). "A Combined Large-Eddy Simulation and Time-Dependent RANS Capability for High-Speed Compressible Flows". In: *Journal of Scientific Computing 1998 13:3* 13 (3), pp. 253–274. ISSN: 1573-7691. DOI: 10.1023/A:1023266932231.

Sundén, Bengt and Juan Fu (2017). "Introduction". In: *Heat Transfer in Aerospace Applications*, pp. 1–17. DOI: 10.1016/B978-0-12-809760-1.00001-6.

Szubert, Damien (2015). "Physics and modelling of unsteady turbulent flows around aerodynamic and hydrodynamic structures at high Reynold number by numerical simulation". In.

Szubert, Damien et al. (2015a). "Numerical study of the turbulent transonic interaction and transition location effect involving optimisation around a supercritical aerofoil". In: *European Journal of Mechanics - B/Fluids* 55, pp. 380–393. ISSN: 09977546. DOI: 10.1016/j.euromechflu.2015.09.007.

Szubert, Damien et al. (2015b). "Shock-vortex shear-layer interaction in the transonic flow around a supercritical airfoil at high Reynolds number in buffet conditions". In: *Journal of Fluids and Structures* 55, pp. 276–302. ISSN: 10958622. DOI: 10.1016/j.jfluidstructs.2015.03.005.

Szubert, Damien et al. (2016). "Numerical study of the turbulent transonic interaction and transition location effect involving optimisation around a supercritical aerofoil". In: *European Journal of Mechanics, B/Fluids* 55, pp. 380–393. ISSN: 09977546. DOI: 10.1016/j.euromechflu.2015.09.007.

Tijdeman, H (1977). "Investigation of the transonic flow around oscillating airfoils". In: *National Aerospace Lab. Amsterdam, Netherlands* TR-77-090U. DOI: b07421b9-136d-494c-a161-b188e5ba1d0d.

Tô, J.-B. et al. (2019). "Effects of vibrating and deformed trailing edge of a morphing supercritical airfoil in transonic regime by numerical simulation

at high Reynolds number". In: *Journal of Fluids and Structures*. ISSN: 0889-9746. DOI: 10.1016/J.JFLUIDSTRUCTS.2019.02.011.

Townsend, A. A. (Dec. 1956). "The properties of equilibrium boundary layers". In: *Journal of Fluid Mechanics* 1 (06), p. 561. DOI: 10.1017/S0022112056000378.

Vos, J. B. et al. (1998). "Recent advances in aerodynamics inside the nsmb (navier stokes multi block) consortium". In: *36th AIAA Aerospace Sciences Meeting and Exhibit*. DOI: 10.2514/6.1998-225. URL: https://arc.aiaa.org/doi/abs/10.2514/6.1998-225.

Wolf, William R. and Sanjiva K. Lele (Nov. 2012). "Trailing-edge noise predictions using compressible large-eddy simulation and acoustic analogy". In: *AIAA Journal* 50 (11), pp. 2423–2434. DOI: 10.2514/1.J051638.

Wong, W. S. et al. (Sept. 2008). "A combined experimental and numerical study of flow structures over three-dimensional shock control bumps". In: *Aerospace Science and Technology* 12 (6), pp. 436–447. DOI: 10.1016/J.AST.2007.10.011.

Appendix A

Collaborative datapaper

Datapaper

Aerodynamic performance in transonic regime around an A320 airfoil by means of electroactive morphing through vibration and slight deformation of the near-trailing edge region at high Reynolds number

By

Jean-Baptiste Tô[1], Thierry Louge[2], Clément Rouaix[1], César Jimenez Navarro[1], Abderahamane Marouf[1,3], Marianna Braza[1]

[1]IMFT- Institut de Mécanique des Fluides de Toulouse, UMR 5502 CNRS-INPT-UT3
[2]CALMIP Supercomputing Meso - Centre, UMS3667 CNRS-INPT-UT3
[3]ICUBE Laboratoire des sciences de l'ingénieur, de l'informatique et de l'imagerieUMR 7357 CNRS

The present article has been elaborated in the context of the Foundation's STAE (http://www.fondation-stae.net/) -RTRA platform DATANOOS: "From Data to noosphere", coordinated by IRIT, (Institut de recherché en Informatique de Toulouse, Michelle Sibilla & Nathalie Aussenac). In this context, the present Datapaper has been prepared within the Use-Case DATANOOS-UC1, "Modélisation enrichie et intelligente de données Avion" coordinated by Marianna Braza, on the basis of INPT/IMFT's data generated in the H2020 European research project N° 723402: SMS, "Smart Morphing and Sensing for aeronautical configurations", www.smartwing.org/SMS/EU in collaboration with the CALMIP, (T. Louge) who launched the CALLISTO Interface for a Semantic Toolbox Online: https://callisto.calmip.univ-toulouse.fr/
This collaborative study offers access, interoperability and reuse of these data in the context of Open / FAIR research data in Horizon 2020.

The present article studies through appropriate vibration and deformation of the near trailing edge region of a supercritical A320-type morphing airfoil the physical mechanisms related the aerodynamic performance modification, e.g. the change in the lift and drag coefficients due to modification of the near wake's turbulence structure and of the shock-boundary layer interaction. The upstream Mach number is 0.78 and the wing is placed at an incidence of 1.8°, both parameters corresponding to nominal cruise operating conditions.

The airfoil's chord measures 15 cm, corresponding to the so-called tRS, "transonic Reduced Scale" prototype of the H2020 N° 723402 SMS project "Smart Morphing and Sensing for aeronautical configurations", www.smartwing.org/SMS/EU, coordinated by IMFT/INPT, the experiments of which have accomplished in the transonic wind tunnel of the IMP-PAN Institute at Gdansk, co-partner of the SMS project.

The computations have been carried out in the Olympe supercomputer of the CALMIP Centre with the use of the Navier Stokes MultiBlock (NSMB) code of the European Consortium.

The near trailing edge region of the airfoil is made to vibrate at different frequencies in the 700 Hz to 780 Hz range. This actuation is performed by the use of Macro Fiber Composite (MFC) type piezoactuators, operating at low deformation amplitudes (in the order of 0.5 mm).

Figures 1 and 2 show the qualitative and quantitative modifications of the unsteady aerodynamic force coefficients due to this kind of morphing. An increase of the lift coefficient's mean value is obtained for the case of a 710 Hz actuation, where a drag decrease is achieved for the 720 Hz case on average.

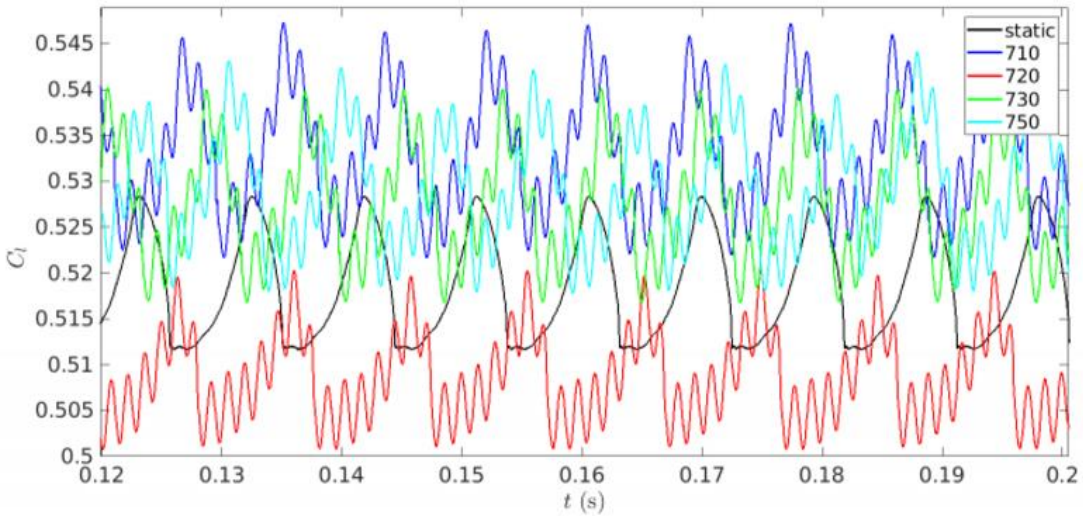

Figure 1 – Time series of the lift coefficient for actuation frequencies f_{ac} = 710 Hz, 720 Hz, 730 Hz, 750 Hz and the static case

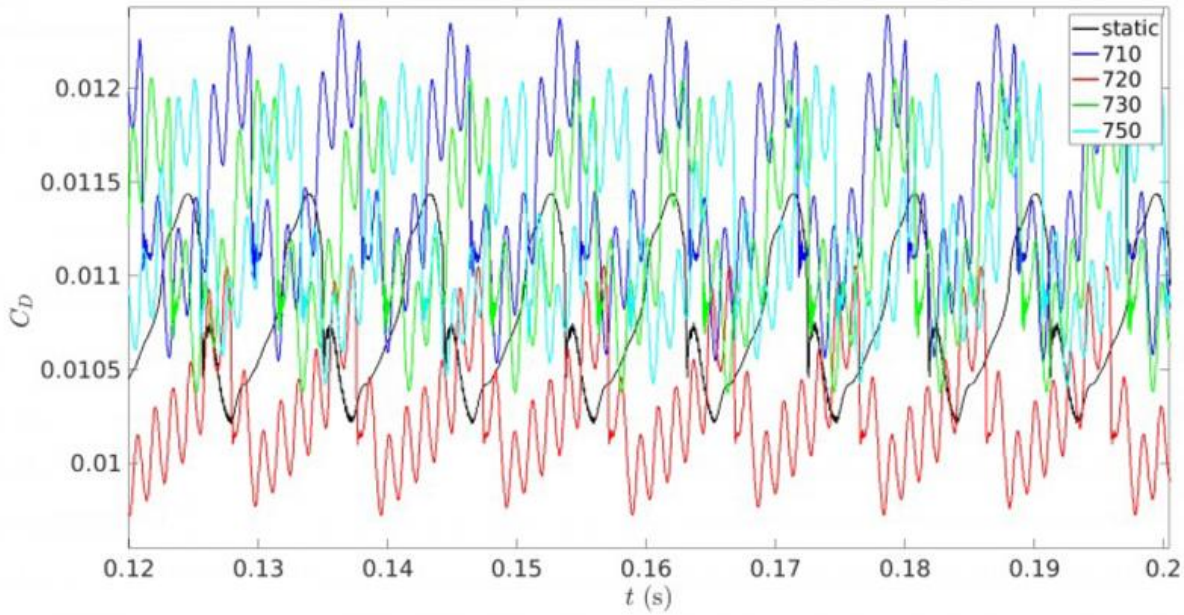

Figure 2 - Time series of the drag coefficient for f_{ac} = 710 Hz, 720 Hz, 730 Hz, 750 Hz and the static case

Power Spectral Densities of the pressure time series measured in the vicinity of the trailing edge as shonw in Fig.3 are performed in order to capture the flow instabilities that may develop in these zones. This information allows us to investigate the mechanisms that govern the interaction between the buffet instability and the actuation frequency. To do so, the Welch method is employed to average the PSD estimation of a statistically stationary signal over long durations, in order to highlight the coherent features of the signal and suppress noise. Hence the signal is first convoluted with a Hamming window which spans 5 periods of the lowest frequency mode, namely the buffet instability mode.

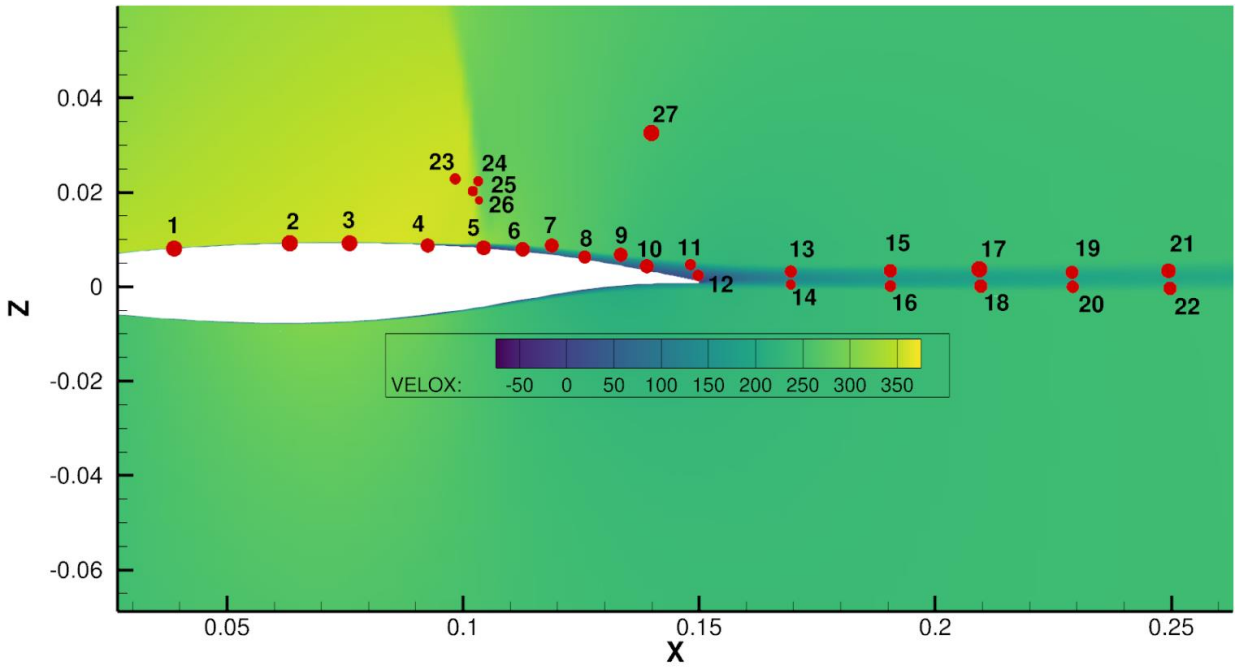

Figure 3 - Location of the probe where the pressure signal is extracted

Figures 4 to 8 show the PSD of the pressure time series for the static case and the actuation cases. The first predominant peak in each one of these PSDs corresponds to the buffet mode, characterized by a quasi-periodic shock motion. A lock-in mechanism around the actuation frequency is obtained, (Tô *et al*) allowing the modification and control of the buffet instability which is responsible for drag increase, a crucial issue in cruise flight conditions. This lock-in is a synchronization phenomenon between the buffet instability and the actuation frequency, the latter being highlighted here by the consistent presence of a strong peak in the PSD at the actuation frequency.

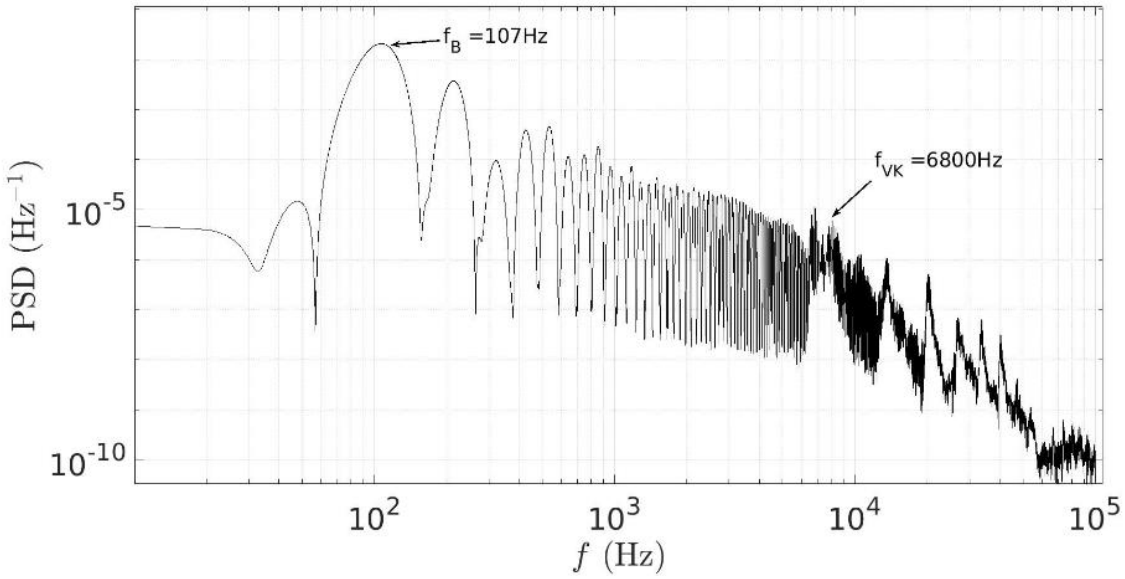

Figure 4 - PSD diagram of the pressure signal at the trailing edge for the static case

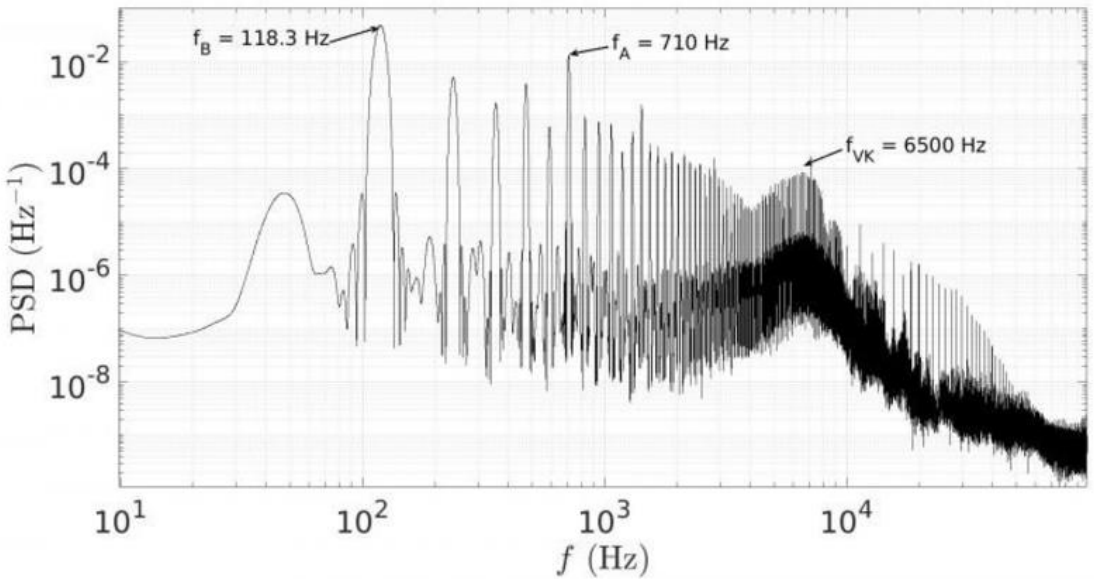

Figure 5 - PSD diagram of a pressure time series monitored at the trailing edge for a 710 Hz actuation frequency

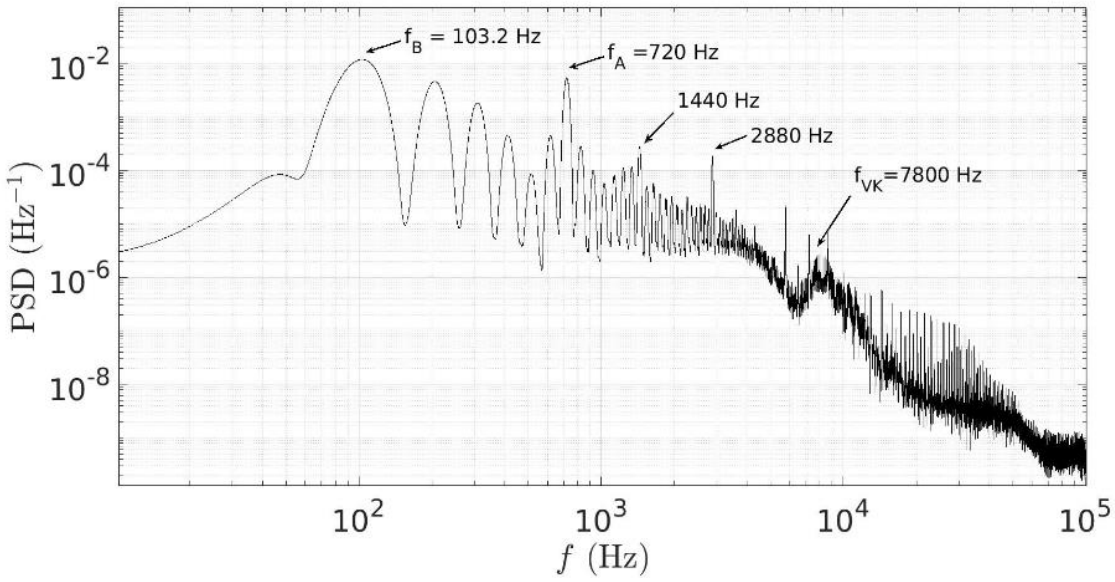

Figure 6 - PSD diagram of a pressure time series monitored at the trailing edge for an actuation frequency of 720 Hz

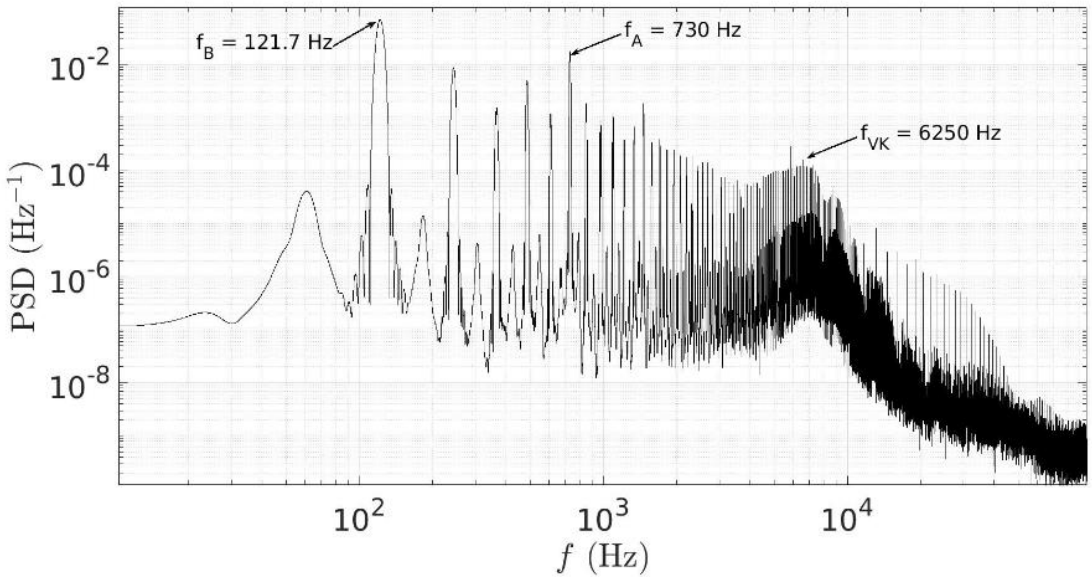

Figure 7 - PSD diagram of a pressure time series monitored at the trailing edge for a 730 Hz actuation frequency

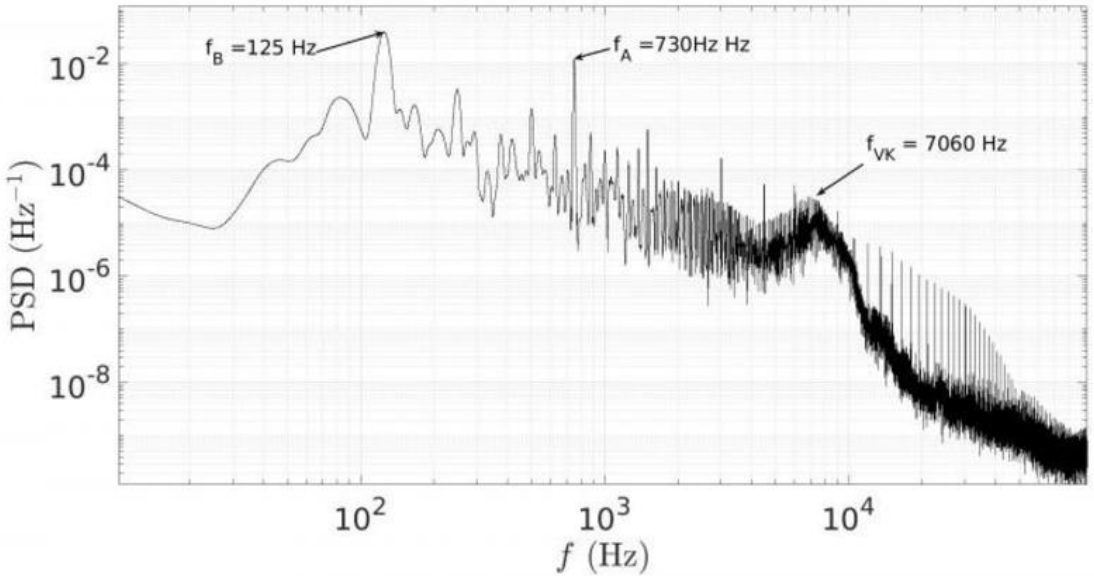

Figure 8 - PSD diagram of the pressure at a pressure time series monitored at the trailing edge for an actuation frequency of 750 Hz

The bump in the higher frequency range, that is between 6000 Hz and 9000 Hz, corresponds to formation of the von Kármán instability in the wake. The harmonics on the right side of the buffet frequency interact with the sub-harmonics of the von Kármán bump and illustrate the *feedback* effect of the downstream unsteadiness marked by coherent vortices being shed in the wake and creating an opposite circulation which translates in an upstream pressure transport. Through this feedback, morphing therefore affects the pressure distribution around the airfoil which modifies the aerodynamic coefficients.

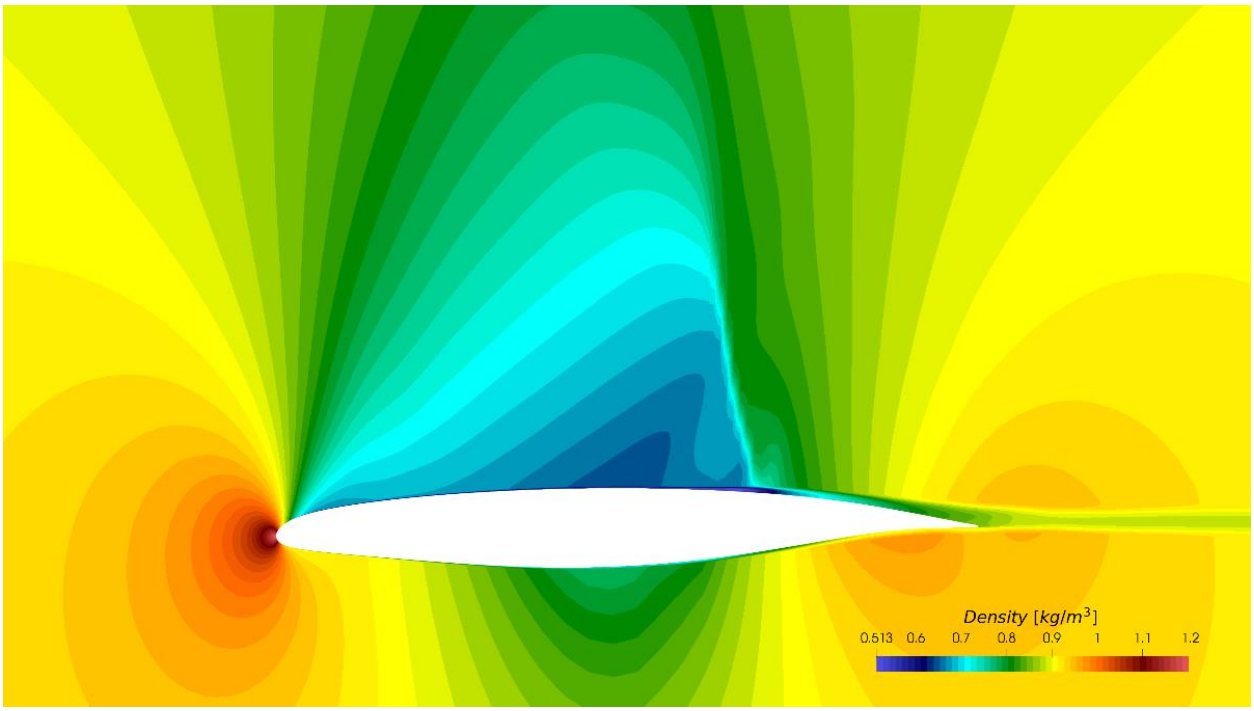

Figure 9 - Iso-density contours, Morphing A320 wing, transonic regime, actuation frequency at 720 Hz near trailing edge, by means of piezo-actuators

Figure 9 shows the iso-density contours around the wing in the case of an actuation frequency of 720 Hz (corresponding to a minimum of mean drag). The turquoise zone illustrates the supersonic flow region terminated by the sharp normal shock wave, followed by the separated boundary layer and the shear layers that form the wake downstream.

The present data paper ensures access to the data corresponding to the signals available in the Callisto platform of CALMIP. Moreover, thanks to suitable workflows, the PSD hereby presented can be calculated by the corresponding algorithm in the workflow. Figure 9 can be produced by using the following file (https://doi.org/10.48531/jbru.calmip/p76fwg) provided in the Callisto dataverse. A suitable workflow involving the right scripts will extract the desired iso-contours from this file. Data presented in this paper are integrated in a series of tools inside Callisto for public finding, comparing and analysis.

In order to use the tools and services available, one can access the working space of CALLISTO interface (https://callisto.calmip.univ-toulouse.fr/index-work.php) and change the default repository for the “sms” repository. Then, different possibilities are available including “Semi-automatic data analysis”. Indicating “Near trailing edge piezo actuation” or “Airfoil pressure distribution” (which are cited here only as examples of how to achieve a successful search for information) and using the “Query” option lead to the listing of available datasets, as seen in Figure 10.

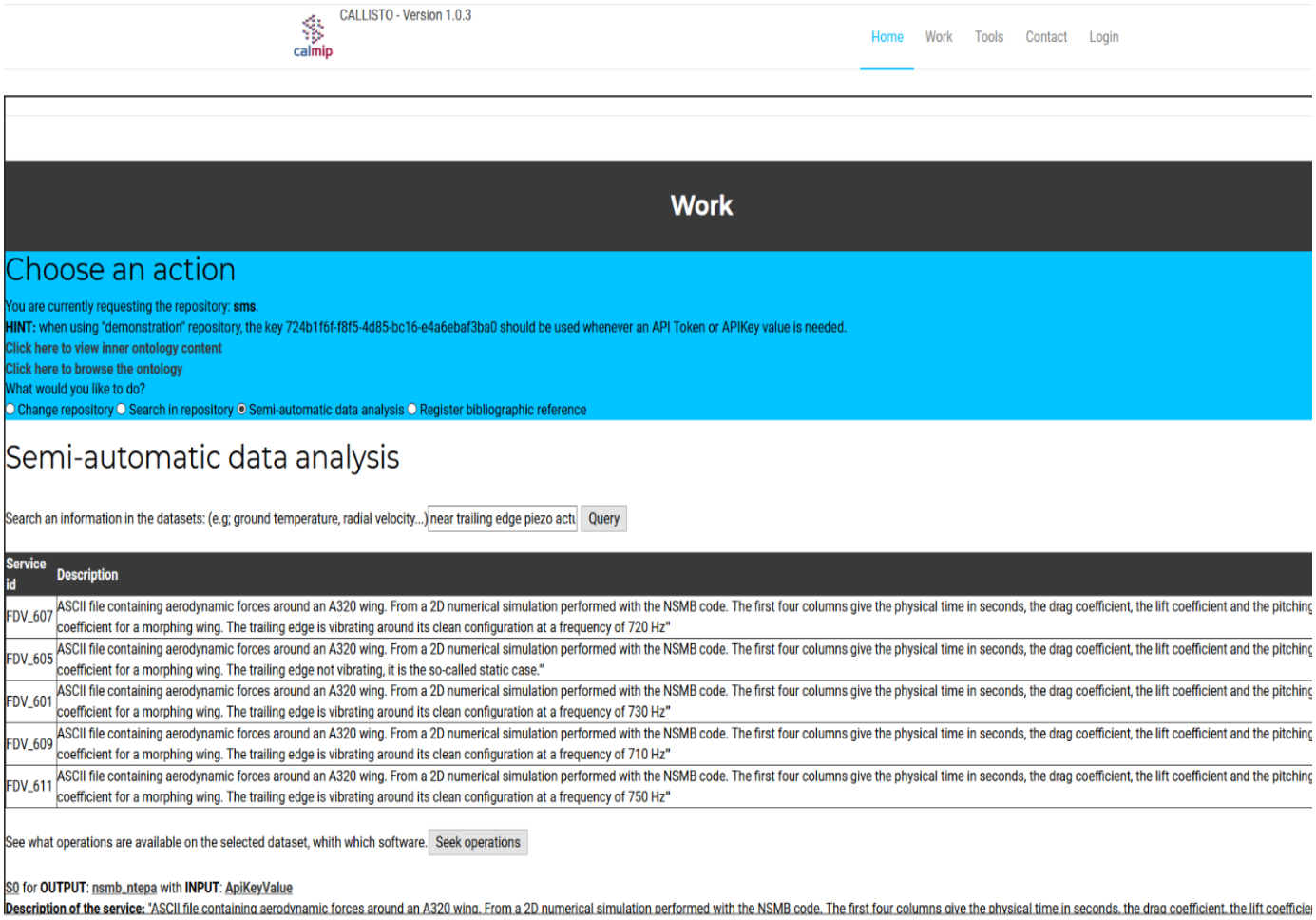

Figure 10: Callisto interface, reusing data part 1.

Choosing one of the datasets and activating “Seek operations” compose available workflows for the corresponding datasets and allow a user to perform the operation described on the present paper (PSD calculation and display, use paraview to display the static airfoil PSD). Figure 11 shows the workflow composition step of the overall process.

Data finding, reuse and interoperability relies on an ontological representation of SMS data and SMS scientific context aiming to help explaining the data in their scientific context within the SMS project and ease their use. This specific “SMS ontology” developed in Callisto helps to access to selected metadata of the SMS project (numerical and experimental) as well as to use the aforementioned workflow algorithms. This ontology is publicly available and may be queried, exported and is available with some example queries within Callisto (https://allegro.callisto.calmip.univ-toulouse.fr/#/repositories/sms/overview)

Supplemental elements in the CALLISTO web interface lead to an inner view of the SMS ontology, either wide or fine-grained following in which step the browsing is started. It is also possible to browse this ontology by a graphical interface (https://allegro.callisto.calmip.univ-toulouse.fr/#/repositories/sms/gruff).

This browsing ilustrated in figure 12 helps to have a complete understanding of the data and its environment. The programming language used for coding the sofware involved in data acquisition or processing, libraries, details in algorithms for equation solving are examples of elements that can be accessed by this means.

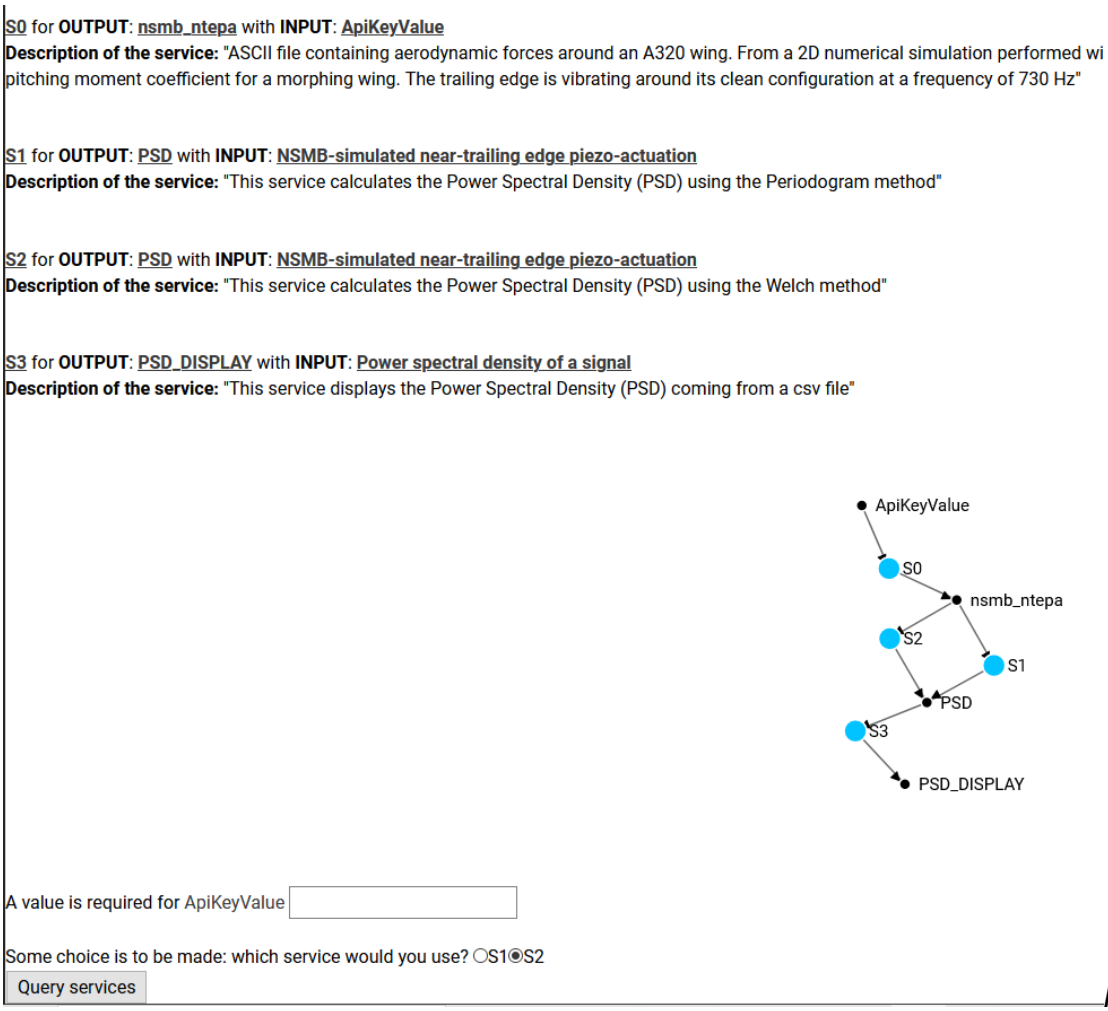

Figure 11: Callisto interface, reusing data part 2.

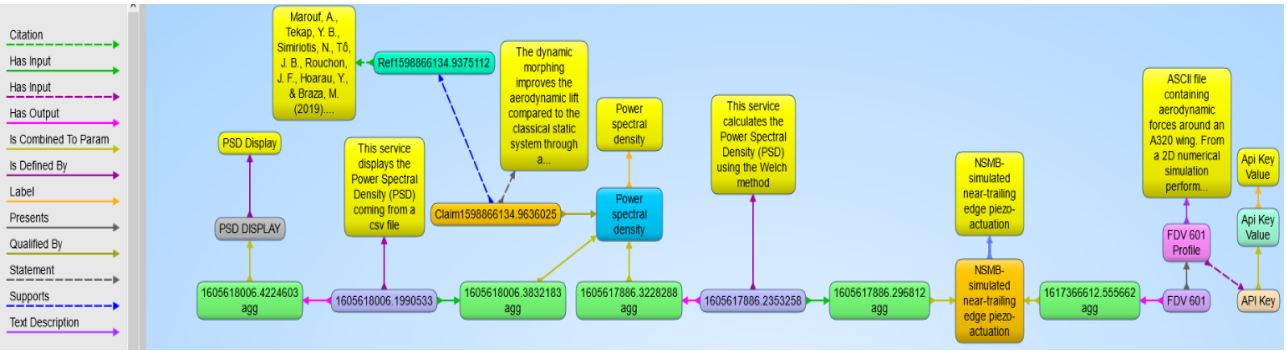

Figure 12 : A partial representation of the ontology showing a workflow and the involved algorithms

Furthermore, CALLISTO also allows to register DOIs for datasets, which has been done for the datasets presented in this paper. These DOIs are the following:

Aerodynamic forces; 2D morphing - numerical simulations - incidence 1.8 deg - static case: https://doi.org/10.48531/jbru.calmip/buabfj

Aerodynamic forces; 2D morphing - numerical simulations - incidence 1.8 deg - frequency 710 Hz: https://doi.org/10.48531/jbru.calmip/robira

Aerodynamic forces; 2D morphing - numerical simulations - incidence 1.8 deg - frequency 720 Hz : https://doi.org/10.48531/jbru.calmip/echixn

Aerodynamic forces; 2D morphing - numerical simulations - incidence 1.8 deg - frequency 730 Hz: https://doi.org/10.48531/jbru.calmip/jx2o55

Aerodynamic forces; 2D morphing - numerical simulations - incidence 1.8 deg - frequency 750 Hz : https://doi.org/10.48531/jbru.calmip/x5unj4

plt dataset for Paraview visualization - 730 Hz morphing actuation : https://doi.org/10.48531/jbru.calmip/p76fwg